

Cover Page



Universiteit Leiden



The handle <http://hdl.handle.net/1887/138639> holds various files of this Leiden University dissertation.

Author: Mandal, S.

Title: Revealing the nature of new low-frequency radio source populations

Issue Date: 2020-12-10

Revealing the nature of new low-frequency radio source populations

Proefschrift

ter verkrijging van
de graad van Doctor aan de Universiteit Leiden,
op gezag van Rector Magnificus prof. mr. C.J.J.M. Stolker,
volgens besluit van het College voor Promoties
te verdedigen op donderdag 10 december 2020
klokke 11:15 uur

door

Soumyajit Mandal
geboren te Purulia, India
in 1992

Promotiecommissie

Promotor: Prof. dr. H. J. A. Röttgering
Co-promotor: Dr. R. J. van Weeren

Overige leden: Dr. I. Prandoni (IRA-INAF, Bologna)
Prof. dr. M. Brügger (University of Hamburg)
Dr. H. T. Intema
Prof. dr. H. Hoekstra
Prof. dr. P. P. van der Werf

ISBN: 978-94-6423-083-3

Cover: The cover design and coloring is done by Elena Garuccio and Soumyajit Mandal. The background source of the front cover is the ‘radio phoenix’ in the galaxy cluster Abell 2593, as seen by LOFAR telescope and is overlaid with a ‘phoenix’, a mythological bird that is created from the ashes of its own predecessor. The back cover is a small section the Lockman Hole field. This is one of the deepest radio images ever made at 150 MHz.

*“The sky is full of the sun and the stars
The universe is full of life
Among all these I have found a place
And in wonder and amazement I sing”
–Rabindranath Tagore*

Contents

1	Introduction	1
2	Merging galaxy cluster Abell 1914	13
2.1	Introduction	14
2.1.1	LOFAR data reduction	21
2.1.2	GMRT data reduction	24
2.1.3	VLA data reduction	26
2.1.4	Chandra data reduction	26
2.1.5	CFHT data	26
2.1.6	Spectral index maps and integrated spectrum calculation	27
2.2	Results	30
2.2.1	RP: A radio phoenix candidate	30
2.2.2	HT: A head-tail galaxy	31
2.2.3	RH: A radio halo candidate	31
2.3	Discussion	34
2.4	Summary and conclusions	37
3	Revived fossil plasma sources in galaxy clusters	41
3.1	Introduction	42
3.2	Sample selection	48
3.3	Observations and methods	49
3.3.1	GMRT data reduction	49
3.3.2	LOFAR data reduction	50

3.3.3	Spectral index maps and integrated spectrum calculation	50
3.3.4	X-ray data reduction	51
3.4	Results	52
3.4.1	Abell 2593	52
3.4.2	SDSS-C4-DR3-3088	54
3.4.3	Abell 2048	55
3.5	Discussion	60
3.5.1	AGN connection	60
3.5.2	Spectral index	60
3.5.3	Mass, temperature, dynamical state, and position of the radio source in the cluster	61
3.6	Conclusion	62
3.A	Spectral index error map	64
3.B	Additional spectral index and error maps of SDSS-C4-DR3-3088	65
4	Sample of radio phoenixes in galaxy clusters	67
4.1	Introduction	68
4.2	Sample Selection	76
4.3	Observations and Methods	77
4.3.1	GMRT Data Reduction	77
4.3.2	LOFAR Data Reduction	77
4.3.3	VLA Data Reduction	78
4.3.4	X-ray Data Reduction	78
4.3.5	Integrated spectral index	82
4.4	Results	82
4.5	Common properties	89
4.6	Discussion	92
4.7	Summary and conclusion	97
4.A	GMRT Maps	106
5	Source counts from LoTSS Deep Fields	109
5.1	Introduction	110
5.2	Observations and Data reduction	116
5.3	Source extraction, masking and deblending	117
5.3.1	Visibility function of raw and final catalogues	118
5.3.2	Source Size Deconvolution	119
5.4	Source Size Distribution and Resolution Bias	124
5.5	Eddington bias	134
5.6	Differential source counts	139

5.7	Conclusions	143
5.8	Acknowledgements	144
5.A	Appendix	146
	Bibliography	146
	Nederlandse samenvattig	167
	List of publications	173
	Curriculum Vitae	177
	Acknowledgements	179

Chapter 1

Introduction

The formation history of our Universe has been a topic of discussion since ancient times. With the advancement in science and technology, humankind has been able to untie a few knots in the vast web of mystery. The Big Bang is the accepted cosmological theory that describes how the Universe began before undergoing a sequence of complex hierarchical structure formation. The theory asserts that the Universe started about 13.7 billion years ago in an initial state of very high temperature and density ([Komatsu et al. 2011](#), [Planck Collaboration et al. 2016](#)). The Λ CDM : current standard model of cosmology, states that our Universe consists of baryonic matter (5%), cold dark matter (22%) and dark energy density (73%). This model successfully describes some of key observed phenomena such as the abundance of the light elements (Helium, Hydrogen and Lithium), the Cosmic Microwave Background (CMB) radiation ([Smoot et al. 1992](#), [Bennett et al. 1996](#) [Planck Collaboration et al. 2016](#)), the accelerated expansion of the universe ([Riess et al. 1998](#)) and the large-scale structures.

A key ingredient of the Λ CDM model is the theory of cosmic inflation ([Guth 1981](#), [Guth & Steinhardt 1984](#)) that suggests, our Universe, in its first few moments, went through an extremely rapid exponential expansion. In a tiny fraction of a second ($\sim 10^{-32}$ s), the linear size of the Universe increased by a factor of 10^{26} . This explains that distant regions of the Universe were actually much closer together prior to inflation and could have been causally connected, thus having same physical properties. This sudden expansion as invoked by

inflation, also results in a flat-space geometry. This could also explain that, during this process the density of the magnetic monopoles dropped exponentially making their detection highly unlikely.

Our Universe is remarkably homogeneous and isotropic on larger scales. The CMB radiation has a spectrum consistent with that of a black body at a temperature of $T_{\text{CMB}} = 2.725\text{K}$ (Fixsen 2009). However, tiny variations in the CMB temperature indicate that at that time there were small-scale density fluctuations (Smoot et al. 1992, Mather et al. 1994, Kovac et al. 2002). These tiny fluctuations are thought to be related with the quantum fluctuations of matter density that are present immediately after the Big Bang. Under the influence of gravity, these small scale primordial CMB density fluctuations can grow hierarchically. First, halos of cold dark matter formed and these merged with each other to accrete more mass (Springel et al. 2006). The baryonic matter that primarily follows the dark matter halos, then cooled and collapsed, forming clouds of gas, stars, galaxies and eventually the largest structures of all, namely clusters of galaxies. These clusters are the focus of this thesis.

Galaxy clusters

Galaxy clusters are the largest gravitationally bound systems of the Universe, with masses up to $10^{15}M_{\odot}$. Even though clusters can contain up-to thousands of galaxies, the majority (80%) of the cluster-mass is constituted by dark matter (Blumenthal et al. 1984). Dark matter only interact with the baryonic matter ($\sim 20\%$) through gravitational force. Of the baryonic mass, 85% is comprised of a hot ($10^7 - 10^8$ K), rarefied ionised plasma, that fills the entire volume of the cluster, referred as intra-cluster medium (ICM). This dilute plasma emits thermal Bremsstrahlung radiation that is visible at X-ray wavelengths. Stars, cold gas and dust in galaxies form the remaining 15% of the baryonic mass.

Galaxy clusters are continuing to grow via the accretion of smaller groups of galaxies and through major merger events with other cluster of galaxies (Kravtsov & Borgani 2012). This process of cluster mergers and continuous accretion of gas from the inter-galactic medium (IGM), can create shock waves in and around galaxy clusters. The most spectacular are events where two massive clusters merge. This releases a huge amount ($\sim 10^{64}$ ergs) of gravitational energy into the ICM. The released binding energy strongly affects the physical properties of the system including density distribution & velocity dispersion of member galaxies and temperature, metallicity & density distribution of the X-ray emitting thermal ICM. Direct evidence of associated density, pressure and temperature jumps are seen with X-ray observations (Markevitch & Vikhlinin

2007). Merger driven shocks, bulk flows and turbulence can amplify the magnetic field ($\sim \mu\text{G}$) strength (Roettiger et al. 1996, Roettiger et al. 1997) and affect the spatial transport of the relativistic ($\gamma > 1000$) particles (also known as cosmic rays, CRs). In the presence of magnetic fields, these relativistic charged particles can emit synchrotron radiation that can be observed at radio frequencies. Radio observations reveal giant diffuse synchrotron emission that traces the CRs in the ICM (see Feretti et al. 2012, van Weeren et al. 2019, for reviews).

Typically diffuse radio sources in clusters have a steep spectral index¹ ($\alpha \leq -1$). The spectral shape is related to the physics of the (re)acceleration mechanism and the electron synchrotron and inverse Compton (IC) energy losses (Sarazin 1999, Brunetti & Jones 2014). Energy losses limit the life-time of CR electrons in the ICM and the maximum energy at which they can be accelerated by various mechanisms. The presence of CR electrons and magnetic fields in the ICM that generate large-scale diffuse radio sources via synchrotron emission, has fundamental implications on both the physics of the ICM and the evolution of galaxy clusters (e.g. Brunetti & Jones 2014, for a review).

Diffuse radio emission in clusters

In the last decades, with the advent of low-frequency telescopes and X-ray satellites, significant progress has been made to classify diffuse radio sources in the ICM and study the particle acceleration mechanisms. Diffuse radio sources can broadly be classified into two sub-categories based on their morphology and location of the sources in the cluster: *radio halos* and *radio relics*.

Radio halos are extended ($\sim\text{Mpc}$) diffuse radio sources that are located at the centre of merging clusters (Cassano et al. 2008; Cuciti et al. 2015, Kale et al. 2018). They typically have a morphology similar to the X-ray morphology of the ICM. More than 70 radio halos have been discovered (e.g. Feretti et al. 2012; van Weeren et al. 2019). Observational evidence to date suggests that radio halos are caused by continuous acceleration of CR electrons in the turbulent gas (Brunetti et al. 2001, Petrosian 2001, Brunetti & Lazarian 2007). These CR electrons (also known as primary electrons) are injected into the ICM by, for example, radio galaxies, supernovae, or galactic winds. Also, proton-proton collision could be responsible for the generation of secondary electrons (Hadronic model: Dennison 1980, Enßlin et al. 2011) that can be re-accelerated together with primary CR electrons (Brunetti & Lazarian 2011; Pinzke et al. 2017) and generate large-scale radio halos. However, current upper limits on the

¹ $S_\nu = \nu^\alpha$; S_ν is the measured flux density of a radio source at the observed frequency ν

γ -ray emission in galaxy clusters puts constraints on the hadronic origin of radio halos (Jeltema & Profumo 2011; Ackermann et al. 2016; Brunetti et al. 2017).

Radio relics are ~ 1 -2 Mpc long and are located in the cluster outskirts (Feretti et al. 2012, van Weeren et al. 2019). Typically they have a convex morphology with respect to the cluster centre, are linearly polarized (20% to 30% at GHz frequencies) and exhibit a radio spectral steepening towards the cluster centre (e.g. van Weeren et al. 2010, Bonafede et al. 2012, Stroe et al. 2013, Hoang et al. 2017, Kierdorf et al. 2017 etc.). Cluster radio relics are thought to be tracers of merger induced shock waves (e.g. Finoguenov et al. 2010, Shimwell et al. 2015, Botteon et al. 2016 etc.). Typically, the spectra of radio relics are well represented by a power-law; however, it is now a matter of debate if radio relics have a curvature at frequencies higher than ~ 2 GHz (Stroe et al. 2016, Loi et al. 2017).

Nowadays, the connection between radio relics and shocks is well established. However, the underlying acceleration mechanism is still debated. Primarily shocks are thought to accelerate particles via diffusive shock acceleration (DSA, Krymskii 1977; Bell 1978a; Bell 1978b etc.). DSA is also known as Fermi-I mechanism and asserts that CR particles are scattered in the upstream and downstream regions of a shock by plasma irregularities. Due to these repeated reflections at the shock fronts, CR electrons gain their non-thermal energy (Fermi 1949). It was originally thought that electrons in the thermal pool could be accelerated by DSA to produce the observed (radio) emission. However, the acceleration efficiency via DSA is found to be low, and insufficient to generate bright radio relics (van Weeren et al. 2016a, Botteon et al. 2016 etc.). Also, a connected problem with the large acceleration efficiencies concerns the lack of γ -ray emission from galaxy clusters (Vazza et al. 2014; Vazza et al. 2015; Wittor et al. 2017).

For these reasons, the role of ‘**fossil plasma**’ or seed particles have been invoked, as recent simulations indicate that re-acceleration of seed relativistic particles is more efficient than the DSA (e.g. Kang & Ryu 2015). A similar issue has also been suggested for the generation of radio halos that may require an initial pool of mildly relativistic CR electrons for turbulent re-acceleration (Brunetti & Jones 2014). A key question that needs to be answered is what are the source of these fossil electrons in the ICM? It is clear that galaxy clusters host active galactic nuclei (AGN). These AGNs can inject CR electrons into the ICM and in the presence of magnetic fields can generate synchrotron radio emission (Vantyghem et al. 2014). Such AGNs that are very luminous at radio wavelengths are known as radio galaxies and are often accompanied by single or twin radio lobes that can extend up-to Mpc scales. These energetic CR electrons

from the lobes of a radio galaxy can provide the seed populations of relativistic electrons and a possible connection between radio galaxies and re-acceleration mechanisms in radio halos or radio relics (Kang & Ryu 2016). Such tentative morphological connections of radio galaxies with radio relics have been proposed by Bonafede et al. (2014), Shimwell et al. (2015) and most clearly has been shown by van Weeren et al. (2017) in the galaxy cluster pair Abell 3411–3412.

Studying the population of fossil electrons is not trivial. When the central AGN of a radio galaxy switches off and there is no supply of freshly injected particles, the so-called ‘AGN remnant lobes’ can diffuse into the surrounding medium. Due to synchrotron and radiative losses, after a few tens of Myr, their spectrum becomes steep ($\alpha \leq -1.2$) and curved. The fossil plasma becomes invisible and hard to detect, even at the lowest observable frequencies (Brienza et al. 2017, Hardcastle 2018, English et al. 2019). However, in a cluster environment, these low-energy relativistic ($\gamma \sim 100$) electrons can still be poorly mixed with the ICM (Sarazin 1999; Petrosian 2001; Pinzke et al. 2013). Merger driven turbulence, shocks and ICM bulk motion can adiabatically compress these old fossil electrons (Ensslin et al. 1998; Enßlin & Brüggen 2002) and emit observable (sub GHz) radio waves again. These revived fossil plasma sources, which are known as **radio phoenixes**, provide us with a unique opportunity to study these otherwise invisible population of electrons (Kempner et al. 2004). To date, only a few radio phoenixes have been discovered (Slee et al. 2001, van Weeren et al. 2009, de Gasperin et al. 2015). In order to understand the acceleration mechanisms responsible for the generation of radio phoenixes, it is crucial to identify their common observational and physical properties and compare them with that of radio halos and relics. This will also help in establishing radio phoenixes as a distinct class of objects and enable us to better understand the nature of this relatively unexplored population.

Faint radio population

Radio source counts that are derived from deep 1.4 GHz surveys, had shown a sudden steepening below 1 mJy (Windhorst et al. 1990, Prandoni et al. 2001b). This is interpreted as a result of the emergence of a faint radio population; which is different in nature from the ones that dominate at higher flux densities (such as radio loud AGNs). The faint radio population most likely consists of several types of objects such as: faint (radio-quiet) AGNs, starburst galaxies, distant clusters, normal spirals and ellipticals. The physical and evolutionary properties of faint radio sources and the relative importance of the different class of objects are still being debated and their redshift distribution and luminosity

properties are not well known (Prandoni et al. 2001a). This is mainly because the current samples of such objects are small. Moreover, optical follow up of these sources are highly incomplete in terms of spectroscopic information (Grappioni et al. 1999, Gregorini & Prandoni 2000). Therefore, it is evident that wider and deeper (low-frequency) radio sky surveys with optical follow-up are strongly needed in order to assess the evolution and the nature of the faint radio population. Observations at low-radio frequencies not only have large field of views, that allow to construct a larger statistical sample and provide more robust statistical constraints but also are more sensitive to (steep spectrum) star forming galaxies that dominate the faint radio population.

Low-frequency radio data processing and advancements

In the last decades, significant progress has been made in order to understand the physics of galaxy clusters. Cluster mergers are the largest particle accelerators of the Universe and these conditions (such as large scales, weak shocks and magnetic fields) cannot be found in other astronomical events or be reproduced on Earth. It is now well established that shocks and ICM motions generated through cluster mergers can produce large-scale synchrotron emission that usually has a very low-surface brightness and steep spectra. Therefore, it is clearly beneficial to study these systems at the low-radio (sub GHz) frequencies.

However, calibration of low-frequency radio data is not trivial due to the direction dependent, time varying effects of the ionosphere that affects both the amplitude and the phase of the radio signal. These ionospheric effects are more dominant towards the lower part of the radio spectrum making it one of the main limiting factors for high-resolution low-frequency radio observations. In addition, the field-of-view at these frequencies, is much larger than at higher frequencies. Therefore, applying a unique correction factor using traditional techniques (such as self-calibration; Pearson & Readhead 1984) to correct these phase and amplitude effects for the entire field of view is too simplistic and is not sufficient. Below, a brief description of two of the pioneer low-frequency radio telescopes: **GMRT** and **LOFAR** is given. These two radio telescopes are also two of key the pathfinders of the future generation radio telescope Square Kilometre Array (SKA; Schilizzi 2005).

The Giant Meterwave Radio Telescope (GMRT; Swarup et al. 1991) is a radio interferometer that is located in India and consists of 30 parabolic dishes of 45 meter diameter each. The GMRT started to improve the low-frequency view of the radio sky in terms of angular resolution and sensitivity. This has been shown in a few low-frequency surveys centred around 150 MHz (e.g.: Ishwara-

Chandra et al. 2010, Sirothia et al. 2009). Most importantly, in the last 10 years, the development of the Source Peeling and Atmospheric Modeling (SPAM; Intema et al. 2009, Intema 2014), have made a significant improvement on the ionospheric calibration of the low-frequency radio data. This fully automated pipeline includes state-of-the-art calibration, radio frequency interference (RFI) mitigation schemes, direction-dependent calibration, and ionospheric modeling. One of the most important data products of this pipeline is the 150 MHz TIFR GMRT Sky Survey (TGSS ADR; Intema et al. 2017). The TGSS is the most sensitive (2-5 mJy/beam rms noise) radio sky survey at such low-frequency till date, that covers almost 90% (-53° to $+90^\circ$) of the whole sky.

The Low Frequency Array (LOFAR; van Haarlem et al. 2013) is the largest pathfinder to the SKA that operates at the lowest observable frequency range of 30-240 MHz. LOFAR is a new-generation radio telescope that uses phased aperture array technique in which the antenna primary beam is formed electronically. This is different from traditional radio telescopes that use mechanical steering of antennas. Most of the LOFAR antennas are based in the Netherlands, with baseline lengths ranging from 100 meters to 120 km. Additional remote stations are located throughout Europe. The longest European baseline of LOFAR can provide a resolution of $0.5''$ at 150 MHz. The combination of LOFAR's large field of view, wide range of baseline lengths, and large fractional bandwidth makes it a powerful instrument for performing large area and deep sky surveys. These enormous capabilities of LOFAR also make the challenges to tackle the radio data calibration and imaging (at such low frequencies) more complicated since, the ionosphere and its associated Faraday rotation and sky structure are heavily direction dependent and time varying. In the last few years, novel algorithms have been developed to overcome these challenges; such as SAGECal (Yatawatta et al. 2013), Facet Calibration (van Weeren et al. 2016b), KillMS (kMS; Tasse 2014; Smirnov & Tasse 2015), DDFacet (Tasse et al. 2018). Specifically KillMS and DDFacet are now being used for the completion of the LOFAR Two Meter Sky Survey (LoTSS; Shimwell et al. 2017) where the whole northern radio sky is observed with a sensitivity better than $100\mu\text{Jy}/\text{beam}$ at the resolution of $5''$. This upcoming deep and sensitive low-radio-frequency survey will be an excellent tool to further investigate the nature of diffuse radio emission in clusters and of the faint radio population.

This Thesis

With the advent of new generation low-frequency telescopes and better calibration techniques, we have now started to unveil the sub GHz radio sky with

unprecedented depth and sensitivity. Diffuse radio emission have steep synchrotron spectra, meaning that they are brighter at low frequencies and are the ideal targets for LOFAR. LOFAR has been thought to have the potential to make major breakthroughs in the field of cluster science (Röttgering et al. 2006, Röttgering et al. 2011, Cassano et al. 2012, Nuza et al. 2012). Even if the number of such observations are very limited at this stage, the complexity of objects observed has put the traditional taxonomy of diffuse radio sources into question (de Gasperin et al. 2017). Recent LOFAR observations have also strengthened the claim of presence of **fossil radio plasma** in the ICM that could provide the seed particles and can be accelerated to generate large-scale diffuse radio emission (van Weeren et al. 2016a, Shimwell et al. 2016, Hoang et al. 2017, Wilber et al. 2018). Cluster science with LOFAR also includes the fate and evolution of radio lobes/bubbles, the interplay between cluster radio galaxies (AGNs) and the ICM and the distribution of the ICM magnetic fields. In this regard, open questions in this field that are to be answered, are:

- How common is the presence of fossil radio plasma in clusters?
- Do ultra-steep spectrum fossil plasma sources in galaxy clusters have a common origin and is there a connection between radio galaxies and re-acceleration mechanisms in radio halos and relics?
- What is the occurrence of diffuse radio sources as function of cluster mass and dynamical state?
- How useful are the upcoming deep radio surveys in order to understand the nature of faint radio source population?

In order to answer these questions, systematic studies of different classes of radio sources are crucial. It is also very important to combine complementary multi-band data to understand the interaction between different components (such as thermal and non-thermal) of clusters. In addition, observations of these systems at different wavelengths, need to be compared with simulations.

Conducting wide and deep radio sky surveys is one of the main goals of LOFAR since its commencement. For this purpose, a three-tier approach had been adopted. Tier 1 includes the observation of the whole 2π steradians of the northern sky (LoTSS; Shimwell et al. 2017, Shimwell et al. 2019). In these radio images, the most prevalent population is the radio-loud AGN that dominates the bright radio sky. With deeper observations, it is indeed possible for LOFAR to open up a new regime of (much) fainter radio population (such as radio quiet

quasars, distant star-forming galaxies, high-redshift clusters and faint diffuse radio emission). Therefore, deeper Tier 2 and Tier 3 observations were planned to cover smaller areas (over a sky area of 30 deg^2) with a higher sensitivity ($10\text{-}15 \mu\text{Jy}/\text{beam}$; see [Röttgering et al. 2011](#) for more details). In order to scientifically exploit these more sensitive surveys, complementary multi-wavelength data are necessary, most notably to identify the host galaxies of the extra-galactic radio sources and determine their redshift. For these reasons, observations were focused on fields with the highest quality multi-wavelength data available; such as the Lockman Hole, the Boötes and the European Large-Area ISO Survey-North 1 (ELAIS-N1) fields. Studying these deep fields would allow an extreme broad range of science that includes: star formation processes in the early Universe; characterisation of the distribution of star-formation across the galaxy population as a function of mass, luminosity, different environment and redshift; intra-cluster magnetic fields; determining the history of black hole accretion and its dependence with the star formation; the nature of radio filaments and bridges across galaxy clusters that could be related to the accretion shocks and etc. However, before addressing the science questions, it is very important to make sure that the sources in these radio images are properly deconvolved and have reliable flux densities. **Radio source-counts** is one of the immediate data products from these deep radio images that can be used as a sanity check for the data reduction and to study the statistical properties of the (faint) radio source population. Source counts derived from these wide area surveys would overcome uncertainties introduced by low statistics, cosmic variance effects ([Heywood et al. 2013](#)) and other systematics ([Condon et al. 2012](#)). These source counts can also be used to estimate the foreground contamination for Epoch of Reionization (EoR) experiments ([Trott & Wayth 2016](#)).

Thus, the aim of this thesis is two fold:

- To better understand the nature of revived fossil (radio) plasma sources in galaxy clusters and establish them as a distinct class of radio sources (Chapter 2,3 and 4).
- To derive the deepest radio source-counts at 150 MHz (to date) and compare with the other existing determinations, as well as with state-of-the-art evolutionary models (Chapter 5).

Below, the contents of each chapter and the topics discussed within, are described (in brief):

Chapter 2 deals with a detailed study of a merging galaxy cluster Abell 1914. Deep radio (LOFAR 150 MHz, GMRT 325 and 610 MHz and VLA 1.4 GHz),

X-ray (*Chandra*) and optical (CFHT) data are presented. The analysis shows that the ultra-steep spectrum source (4C38.39; $\alpha \leq -2$) that previously was thought to be part of a radio halo, is a distinct source with properties that are consistent with revived fossil plasma sources. In addition, some diffuse emission to the west of the source 4C38.39 was also detected that could belong to a radio halo.

Chapter 3 and 4 present the first systematic study of revived fossil plasma candidates in galaxy clusters. **Chapter 3** demonstrates the discovery potential of the 150 MHz TIFR GMRT Sky Survey (TGSS) in combination with the 1.4 GHz NRAO VLA Sky Survey (NVSS) to find and study revived fossil plasma sources in galaxy clusters. A subset of three candidates (out of which two are new discoveries) was studied in detail using deep multi-band radio (LOFAR and GMRT), X-ray (*Chandra* or *XMM-Newton*) and archival optical observations. Tentative physical properties of these three sources were discussed based on the observations and they were categorised to be in the class of ‘radio phoenixes’. As the next step, in **Chapter 4**, an observational overview of all the known radio phoenixes (either newly discovered or previously known) is presented. Out of 25 sources that are shown, 12 are new discoveries, for which new radio (GMRT and/or LOFAR) and, for a subset, X-ray observations have been shown. Common physical properties of the whole sample of radio phoenixes (such as radio morphology, dynamical state of the host cluster, location of the phoenixes inside the cluster and spectral behaviour) are studied for the first time, in order to establish the nature of this relatively unexplored class of objects. These radio phoenixes are found to have AGN origin and are located well within the R_{500} of the clusters. Presence of dynamical disturbance in the cluster supports the formalism that they are associated with ICM motion and or shocks. Finally, even if these revived fossil plasma tend to have a curved spectra at higher frequencies, presence of non-uniform spectral indices suggests they should not be thought of a reservoir of uniform cosmic-ray population.

In **Chapter 5** the deepest radio source counts, that have ever been obtained at 150 MHz are presented for the Lockman Hole, The Boötes and the Elais-N1 fields. These three fields are the LOFAR Tier-3 depth survey fields (see [Röttgering et al. 2011](#) for details). The derived source counts are compared with other existing determinations, as well as with state-of-the-art evolutionary models (e.g. [Mancuso et al. 2017](#); [Bonaldi et al. 2019](#)). The expected flattening and upturn of the counts below ~ 1 mJy (as also seen in higher frequency surveys) is due to the emergence of the radio-quiet quasar and star-forming populations, which these deeper pointings will critically enable us to properly sample across luminosity and redshift space.

Future studies

In terms of fundamental physics, this century has seen some of the biggest breakthroughs such as discovery of Higgs Boson, detection of gravitational waves etc. and it has become clear that the advancement in technologies play a key role in this process. In the field of radio astronomy, a similar trend in technological advancements had happened in the last decade. Many new generation radio telescopes (such as LOFAR, MWA, ASKAP, MeerKAT etc.) started to become operational and older telescopes have been upgraded (such as VLA, WSRT, GMRT). The LOFAR has already started to reveal the radio sky at frequencies around and even below 100 MHz and has clearly made a significant impact in our understanding of faint radio populations. The lowest observable window of the electro-magnetic radiation is a completely uncharted territory and therefore, is full of potential for new discoveries.

The future of cluster science with LOFAR is undoubtedly promising. The dense core of LOFAR provides excellent sensitivity towards low surface brightness diffuse emission. Furthermore, the arc-second resolution will allow appropriate disentanglement of the foreground/background emission and embedded sources that are projected onto the diffuse emission. In the next few years, few immediate objectives can be achieved:

- Already, from the shallow low-frequency surveys it has become clear that fossil radio plasma can occupy a significant fraction of the cluster volume and provide seed particles for re-acceleration. The known sample of revived fossil plasma sources is probably just the tip of the iceberg of the population and upcoming wider and deeper radio surveys (such as LoTSS; [Shimwell et al. 2019](#) and LoLSS; de Gasperin et al. in prep) will be excellent tools to further investigate the nature of these fossil electron population. Also, studying the spectral behaviour of these diffuse sources would allow for detailed comparisons between the predictions from different particle re-acceleration models and the observational data.
- The brightness fluctuations in the diffuse radio emission reflect the underlying distribution of magnetic fields in the ICM. The high-resolution images from LOFAR are able to resolve scales smaller than the typical coherent scales of magnetic field in galaxy clusters. This will be crucial to probe the magnetic field power spectrum ([Murgia et al. 2004](#), [Vacca et al. 2012](#)).
- [Enßlin & Röttgering \(2002\)](#) predicted that sensitive radio surveys at low

radio frequencies will be crucial to draw an unbiased statistical population of radio halos that can provide unique information about galaxy cluster merger rates and associated non-thermal processes. Also, turbulent re-acceleration model predicts the existence of ultra-steep spectrum radio halos (Cassano et al. 2010) that will be picked up by upcoming low-frequency radio surveys.

Complementary radio observations at high frequencies is also important in order to distinguish between various models for the origin of synchrotron emitting electrons. In addition, following up large unbiased samples of diffuse radio sources at high frequencies will allow us to study the polarisation properties and magnetic field distribution in the ICM. Finally, it is of no doubt that combining X-ray data with radio observations is very important to study the interplay between thermal and non-thermal components in the ICM. Therefore, with the future generation radio (SKA) and X-ray telescopes (eROSITA, ATHENA), we expect to have a much better understanding of galaxy cluster physics.

Chapter 2

Ultra-steep spectrum emission in the merging galaxy cluster Abell 1914

Based on
S. Mandal, H. T. Intema, T. W. Shimwell, R. J. van Weeren, A. Botteon,
H. J. A. Röttgering, D. N. Hoang, G. Brunetti, F. de Gasperin, S. Giacintucci,
H. Hoekstra, A. Stroe, M. Brüggen, R. Cassano, A. Shulevski, A. Drabent,
D. Rafferty
A&A 622, A22 (2019)

Abstract

A number of radio observations have revealed the presence of large synchrotron-emitting sources associated with the intra-cluster medium. There is strong observational evidence that the emitting particles have been (re-)accelerated by shocks and turbulence generated during merger events. The particles that are accelerated are thought to have higher initial energies than those in the thermal pool but the origin of such mildly relativistic particles remains uncertain and needs to be further investigated. The galaxy cluster Abell 1914 is a massive galaxy cluster in which X-ray observations show clear evidence of merging activity. We carried out radio observations of this cluster with the LOw Frequency ARay (LOFAR) at 150 MHz and the Giant Metrewave Radio Telescope (GMRT) at 610 MHz. We also analysed Very Large Array (VLA) 1.4 GHz data, archival GMRT 325 MHz data, CFHT weak lensing data and Chandra observations. Our analysis shows that the ultra-steep spectrum source (4C38.39; $\alpha \lesssim -2$), previously thought to be part of a radio halo, is a distinct source with properties that are consistent with revived fossil plasma sources. Finally, we detect some diffuse emission to the west of the source 4C38.39 that could belong to a radio halo.

2.1 Introduction

Galaxy clusters are the largest gravitationally bound systems in the Universe. They grow through the accumulation of smaller groups of galaxies and through major mergers with other massive clusters. A huge amount of gravitational binding energy ($\sim 10^{64}$ ergs) is released when massive galaxy clusters merge (e.g. [Kravtsov & Borgani 2012](#)). This strongly affects the physical properties of the different properties of clusters, for example the density distribution and velocity dispersion of galaxies, and the temperature, metallicity, and density distribution of the (X-ray-emitting) thermal intra-cluster medium (ICM). Direct evidence for these merging events is seen using X-ray observations, which show the disturbed surface brightness of the ICM and the presence of density and temperature jumps (shocks and cold fronts: [Markevitch & Vikhlinin 2007](#)). The shocks and turbulence that are generated in the ICM might also amplify magnetic fields ($\sim \mu\text{G}$) and accelerate relativistic particles (Lorentz factor $\gamma \gg 1000$), resulting in megaparsec-scale synchrotron emission regions (for review: [Feretti et al. 2012](#), [Brunetti & Jones 2014](#)). The spectral index α of the synchrotron emission is generally steep: $\alpha \lesssim -1$ with $S \propto \nu^\alpha$, where ν is the observed

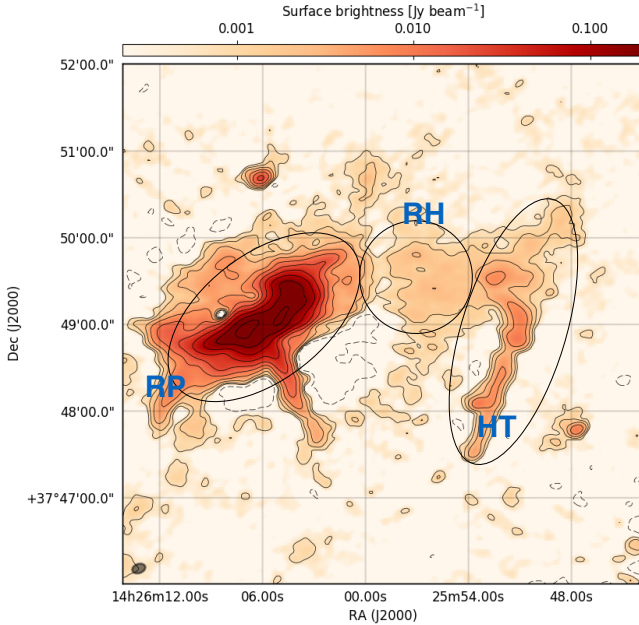


Figure 2.1: Full-resolution ($9'' \times 6''$) LOFAR 120-160 MHz image of Abell 1914 with regions of interest circled and labelled. The black contours and dashed lines indicate the significance of the radio emission at $(1, 2, 4, \dots) \times 3 \times \sigma_{\text{LOFAR}}$ and $-3 \times \sigma_{\text{LOFAR}}$ levels, respectively, where $\sigma_{\text{LOFAR}} = 150 \mu\text{Jy beam}^{-1}$.

frequency and S is the measured flux density. The steep spectral index suggests that the synchrotron emission is relatively bright at low radio frequencies.

While the nomenclature used to describe the emission needs refinement, these synchrotron sources are most commonly classified as either radio haloes or radio relics (Feretti et al. 2012). There are about 50 radio haloes that have been discovered; these are extended ($\gtrsim 1$ Mpc) diffuse radio sources at the centre of merging clusters (e.g. Cassano et al. 2010; Cuciti et al. 2015; Kale et al. 2015) and have a morphology similar to the X-ray morphology.

One of the theoretical models to explain their formation is merger-driven turbulent re-acceleration (Brunetti et al. 2001, Petrosian 2001, Brunetti & Lazarian 2007, Pinzke et al. 2017, Brunetti et al. 2017). Although alternative models have

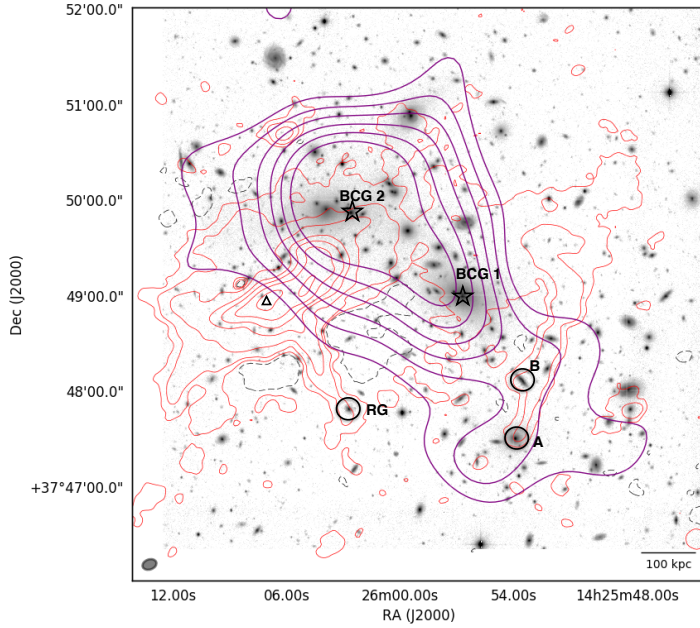


Figure 2.2: Full-resolution ($9'' \times 6''$) LOFAR image overlaid on a CFHT r -band image. The LOFAR contours (solid red) show the $(1,2,4,\dots) \times 3 \times \sigma_{\text{LOFAR}}$ levels and the dashed red contours show the $-3\sigma_{\text{LOFAR}}$ contour where $\sigma_{\text{LOFAR}} = 150 \mu\text{Jy beam}^{-1}$. The purple contours represent the weak lensing measurement (CFHT data: section 2.5) showing the dark matter distribution. The two stars indicate the position of the two brightest cluster galaxies (BCG) in the cluster. The triangle indicates the position of the peak radio emission. The circle A indicates the location of the galaxy that is the optical counterpart of source HT. Circle B indicates a radio-loud galaxy that is not associated with source HT. Circle RG indicates the location of the galaxy that could be a possible counterpart of RP (discussed in section 4).

been proposed, i.e. secondary models, in which the synchrotron emitting electrons are continuously injected by inelastic collisions between cosmic ray protons and thermal protons (e.g. Dennison 1980; Enßlin et al. 2011). The process of generation of secondary particles via proton-proton collisions is thought to play a minor role due to current upper limits in gamma ray observations (Ackermann et al. 2014, Ackermann et al. 2016, Brunetti et al. 2012, Brunetti et al. 2017, Zandanel & Ando 2014) unless this mechanism is combined with turbulent re-acceleration. Radio relics are usually found in cluster outskirts and are thought to trace merger-induced shock waves (e.g. Ensslin et al. 1998; van Weeren et al. 2010; van Weeren et al. 2012a; Roettiger et al. 1999). A connection between relics and shocks has been established by X-ray detections of shocks at the relic location (Finogonov et al. 1993, Akamatsu & Kawahara 2013, Shimwell et al. 2015, Botteon et al. 2016, Eckert et al. 2016). However, in some cases, the luminosity of radio relics is much higher than expected from the acceleration efficiency of thermal electrons from diffuse shock acceleration (DSA; e.g. Brunetti & Jones 2014, Botteon et al. 2016, van Weeren et al. 2016a etc.). Shocks are also able to re-accelerate these electrons via Fermi-type processes. Simulations indicate that such re-acceleration of fossil relativistic electrons should be more efficient than the acceleration of electrons from the thermal pool of the ICM (e.g. Kang & Ryu 2015). Relics are elongated regions with sizes up to 1-2 Mpc long, which have a convex morphology with respect to the cluster centre, exhibit a radio spectral index steepening towards the cluster centre, and are linearly polarised (>10%-30% at GHz frequencies; van Weeren et al. 2010 Bonafede et al. 2012, Stroe et al. 2013, de Gasperin et al. 2015, Kierdorf et al. 2017). Radio phoenixes are another, less widely studied class of diffuse radio sources in the ICM. These are thought to be a manifestation of fossil plasma in galaxy clusters (e.g. Slee et al. 2001; Enßlin & Brüggen 2002; Kempner et al. 2004; van Weeren et al. 2009; de Gasperin et al. 2015). Likely candidates for the fossil electrons are old lobes of radio galaxies that have ultra-steep spectra (USS) owing to synchrotron and inverse Compton (IC) losses. When a merger shock passes through an old lobe (or radio tail), it compresses the fossil radio plasma, thereby re-energizing the electrons and boosting their visibility Enßlin & Gopal-Krishna 2001. As the sound speed in the fossil plasma is much larger than the surrounding ICM and the shocks have a low Mach number ($\mathcal{M} < 2$), this may result in subsonic compression waves generated within the plasma (Enßlin & Gopal-Krishna 2001, Enßlin & Brüggen 2002). Sources powered by this mechanism can maintain electrons at higher energies than what radiative cooling would allow. Although deposited locally, fossil plasma can, over time, occupy a significant volume of the ICM due to turbulent diffusion. The relative impor-

tance of these proposed mechanisms to explain the plethora of diffuse cluster radio sources is still unclear.

In this paper we study extended radio emission in the galaxy cluster Abell 1914, a merging cluster at $z=0.168$ with an asymmetric X-ray brightness distribution (Govoni et al. 2004; G04 hereafter), a high velocity dispersion of $\sigma_V = 1210_{-110}^{+125} \text{ km s}^{-1}$ (Barrena et al. 2013), and a mass of $M_{500} = 7.3 \pm 0.3 \times 10^{14} h^{-1} M_{\odot}$ (Planck Collaboration et al. 2016). The cluster has a luminosity $L_X = (0.1\text{-}2.4 \text{ keV}) = 17.93 \times 10^{44} h_{50}^{-2} \text{ erg s}^{-1}$ (Ebeling et al. 1996) and temperature $kT_X \sim 9 \text{ keV}$ (Baldi et al. 2007; Maughan et al. 2008). In the morphological and dynamical analysis performed by Buote & Tsai (1996), the values of the power ratios $P1/P0$ and $P3/P0$ for this cluster were found to be representative of a disturbed system. Furthermore, Botteon et al. (2018a) found surface brightness and temperature jumps in the ICM. At radio wavelengths, the cluster is known to host an extended, very bright, steep spectrum, and unpolarised radio source (Bacchi et al. 2003; B03 hereafter), namely 4C38.39 (Roland et al. 1985; Komissarov & Gubanov 1994; Kempner & Sarazin 2001). The total flux density as reported in B03 is $20 \pm 3 \text{ mJy}$ at 1.4 GHz, while the spectral index is found to be $\alpha \sim -1.8$. At the resolution of radio data used in the study by B03 (Figure 6) it was suggested that 4C38.39 is a part of a radio halo. However, as we discuss in more detail, the bulk of the radio emission does not align well with the X-ray emission of the ICM nor with the galaxy density distribution. Higher resolution radio observations are essential for shedding more light on the true nature of this source.

In this paper we study the morphology and spectral properties of the radio emission in Abell 1914 at higher angular resolution and better sensitivity than previously using new LOw Frequency ARray (LOFAR) 150 MHz and Giant Metrewave Radio Telescope (GMRT) 610 MHz observations, combined with archival Very Large Array (VLA) 1.4 GHz and GMRT 325 MHz observations, and complemented with optical Canada France Hawaii Telescope (CFHT) and *Chandra* X-ray data. The radio telescope LOFAR (van Haarlem et al. 2013) observes in the relatively poorly explored frequency range between 10 MHz and 90 MHz using the Low Band Antenna (LBA) and 110-240 MHz using the High Band Antenna (HBA). The high sensitivity and abundance of short and long baselines makes LOFAR an ideal instrument to study low-surface brightness diffuse steep-spectrum objects in clusters (e.g. Shimwell et al. 2016; van Weeren et al. 2016a; Hoang et al. 2017; Wilber et al. 2018; Botteon et al. 2018b).

This paper is structured as follows: We present the observations and data processing in Section 2. In Section 3 we show the observational results followed by a discussion of these results in Section 4. In this paper, we assume a Λ CDM

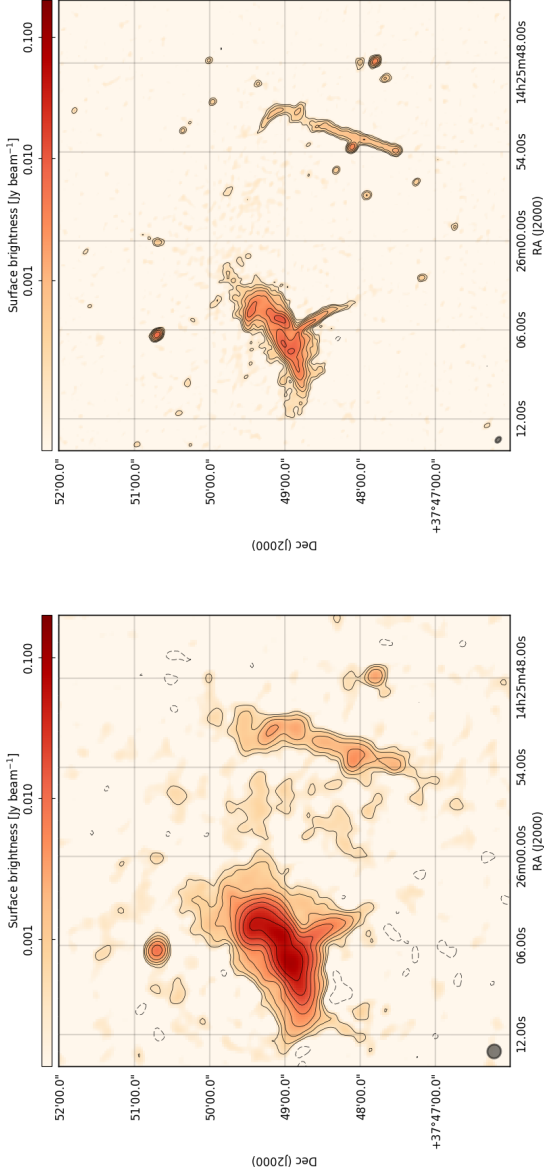


Figure 2.3: Full-resolution GMRT images of Abell 1914 at 325 MHz (left: $11'' \times 10''$) and 610 MHz (right: $5'' \times 4''$). The black contours and dashed lines indicate the significance of the radio emission at $(1, 2, 4, \dots) \times 3 \times \sigma_{\text{GMRT}, 325/610}$ and $-3 \times \sigma_{\text{GMRT}, 325/610}$ levels, respectively, where $\sigma_{\text{GMRT}, 325} = 130 \mu\text{Jy beam}^{-1}$ and $\sigma_{\text{GMRT}, 610} = 40 \mu\text{Jy beam}^{-1}$.

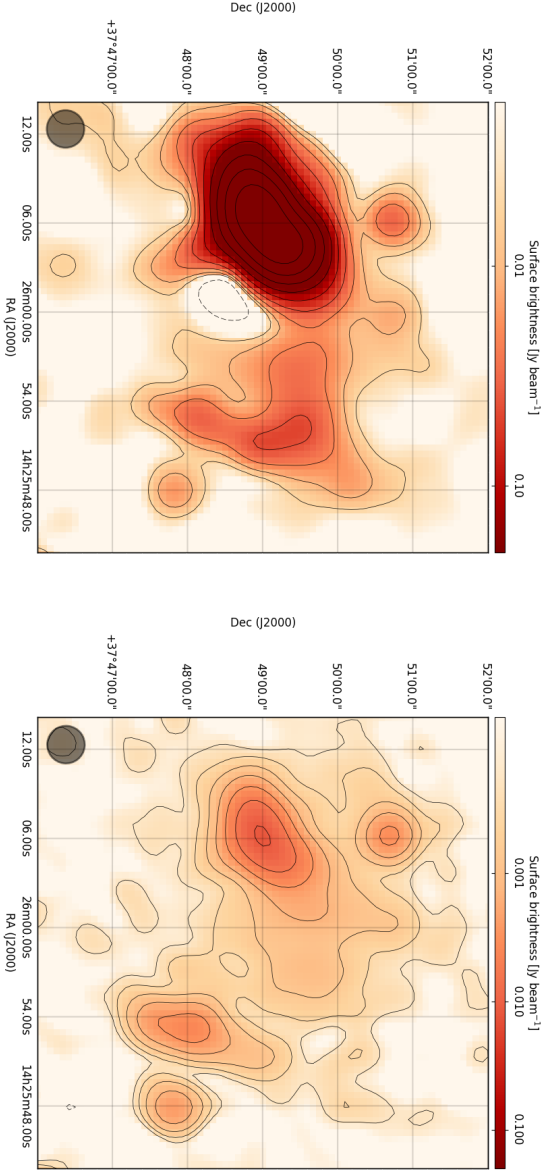


Figure 2.4: Left: 150 MHz LOFAR image ($30'' \times 30''$) in which the contours show the $(1,2,4,\dots) \times 3 \times \sigma_{\text{LOFAR},150}$ levels, where $\sigma_{\text{LOFAR},150} = 1.8 \text{ mJy beam}^{-1}$. Right: 1.4 GHz VLA image ($26'' \times 14''$) where the contours show the $(1,2,4,\dots) \times 3 \times \sigma_{\text{VLA},1400}$ levels, where $\sigma_{\text{VLA},1400} = 40 \text{ } \mu\text{Jy beam}^{-1}$.

cosmology with $\Omega_m = 0.3$, $\Omega_\Lambda = 0.7$ and $H_0 = 70 \text{ km s}^{-1} \text{ Mpc}^{-1}$. At the redshift of the Abell 1914 ($z = 0.168$) the luminosity distance is 808.5 Mpc and 1 arcsec corresponds to 2.873 kpc. All the coordinates are given in epoch J2000.

2.1.1 LOFAR data reduction

We observed Abell 1914 in HBA_DUAL_INNER mode on 13 April 2013. The observation (with ID: 248837) was centred on RA 14h26m01.6s and Dec +37d49m38s. The duration of the observation was 8 hours. We observed the bright source 3C 295 as flux and bandpass calibrator. The frequency coverage for both the calibrator and cluster was 120 to 168 MHz. The visibility data was recorded every 1 second over 64 channels per 0.195 MHz sub-band. As per default, the data were flagged for interference by the observatory with AOFLAGGER (Oftringa et al. 2012), averaged to 2 seconds and 10 channels per sub-band, and stored in the LOFAR long-term archive (LTA¹).

We performed an initial direction-independent calibration following de Gasperin et al. (2018). Then, we corrected for direction-dependent effects using the facet calibration scheme described in van Weeren et al. (2016a) and Williams et al. (2016). More details are provided in the following sections.

Direction-independent calibration

The data were first flagged to remove the bad station CS013HBA. The bandpass and absolute flux scales were calibrated using a model of primary flux calibrator 3C 295 from Scaife & Heald (2012). Since the remote stations are not on the same clock as the core stations, we determined the clock offsets from the calibrator observations. After applying the calibration solutions to the target field data we performed an initial phase calibration on the target field using a model generated from the VLA Low-Frequency Sky Survey (VLSS; Cohen et al. 2007), Westerbork Northern Sky Survey (WENSS; Rengelink et al. 1997), and the NRAO/VLA Sky Survey (NVSS; Condon et al. 1998). This was followed by making high- and low-resolution images of the entire field. Compact and diffuse sources were extracted from these images with PYTHON Blob Detector and Source Finder (PYBDSF; Mohan & Rafferty 2015). These sources were then subtracted from the visibility data to create a residual (source-subtracted) data set.

¹<https://lta.lofar.eu/>

	LOFAR 150 MHz	GMRT 325 MHz	GMRT 610 MHz	VLA 1.4 GHz
Pointing RA, Dec	14:26:01,+37:49:38	14:26:03,+37:49:32	14:26:02,+37:49:38	14:26:01,+37:49:38
Configuration	HBA_DUAL_INNER	N/A	N/A	C and D
Observation date	April 13, 2013	August 29, 2009	Dec. 4, 2016	June 28, 2000 & Sept 25, 2000
On-source time (hr)	8.0	6	6	5
Freq. coverage (MHz)	120-168	308-340	594-626	1.365-1.435

Table 2.1: Details of the radio observations towards Abell 1914.

Data	Frequency (MHz)	robust	taper (")	Θ_{FWHM} " \times ", (PA ^a)	σ_{rms} $\mu\text{Jy beam}^{-1}$	Figure
LOFAR	150	+0.5	0	9 \times 6, (-77.0)	150	2.1
LOFAR	150	0.0	22	30 \times 30, (0.0)	1500	2.4
GMRT	325	0.0	0	12 \times 11, (68.0)	100	2.3
GMRT	610	0.0	0	6 \times 5, (47.0)	55	2.3
VLA	1400	0.0	22	30 \times 30, (0.0)	51	2.4

^a The beam position angle (PA) is measured in degrees from north through east.

Table 2.2: Imaging parameters and image properties of the LOFAR, GMRT, and VLA maps of Abell 1914.

Direction-dependent calibration

In order to improve the image fidelity, we used facet calibration to perform a direction-dependent calibration and thus correct for the ionosphere and beam errors in the direction of the cluster. As the apparent flux density of the cluster dominates the field, it was sufficient to perform a single direction-dependent calibration towards Abell 1914. The resulting calibrated data for the central facet (40' \times 40') were imaged in CASA using the multi-scale multi-frequency (MS-MFS) option in the `clean()` task (Rau & Cornwell 2011). Since the emission from Abell 1914 is within the 99% power point of the primary beam, we did not have to correct for primary beam attenuation. While imaging, we cleaned to a depth of $2\sigma_{rms}$ using scale sizes equal to zero, 3, 7, 9, 25, 60, and 150 pixels, where the pixels have a size of approximately one-fourth of the resolution. After cleaning, the image residuals were mostly noise-like. The brightest source in the cluster (source RP; see Figure 2.1) has a total flux of 4.68 Jy at 150 MHz. In the presence of such a bright extended source, the local background noise of the image is negatively affected due to dynamic range limitations, most likely caused by small residual calibration errors. For this reason, two shallow negative bowls (3σ contours) can be seen to the south-west of RP. More image details are provided in Table 2.2. It is important to note that the deepest negative surface brightness present in the negative region is of the order of -14σ . The RP region consists of an area of 30 beams, which means the amount of total flux density that can be suppressed because of the presence of the negative bowl is $30 \times (14\sigma) = 0.07$ Jy. With a measured flux density of 4.68 Jy for RP, this includes an extra flux of only 1.4%. Even if, in a conservative scenario, the source is extended over 60 beams in the absence of the negative bowl, the suppression in

the total flux would be 3%, which is still small. The presence of the negative bowl may affect the radio halo flux, which is discussed later in detail.

Owing to normalisation issues and inaccurate beam models, flux densities measured from LOFAR images need rescaling to other surveys. We used the TIFR GMRT Sky Survey (TGSS; [Intema et al. 2017](#)), which itself has a flux uncertainty of 10%. We selected six high signal-to-noise ($>20\sigma$) compact sources within the LOFAR facet area from the TGSS to minimise the flux density measurement errors. Even though the number of sources is relatively small, the ratios of the TGSS to LOFAR flux densities are tightly clustered around 0.59 with a scatter of only 2%. To properly take into account the propagation of all flux density uncertainties, we performed a MC simulation in which we modelled each measured LOFAR and TGSS flux density as a Gaussian distribution with the measured flux density as the centre and the uncertainty as the width of the Gaussian, and from which we determined an ensemble of flux ratios. The resulting (combined) flux ratios also follow a Gaussian distribution centred at 0.59 with a 1σ width of 0.06. We adopt these values as our flux correction factor and uncertainty, respectively. For any flux density measurement in LOFAR map, we apply the following correction:

$$S^t = r \times S^m, \quad (2.1)$$

where S^t and S^m are the “true” (scaled to TGSS) and LOFAR flux densities. The value r is the LOFAR flux correction factor as determined above and value Δr is the uncertainty in the correction factor r . The relative error on r is $f = \Delta r/r = 0.10$.

2.1.2 GMRT data reduction

We used the GMRT archival data at 325 MHz of Abell 1914 (project code 16_074) and obtained new data at 610 MHz in the GMRT observation cycle 31 (project code 31_049; details are given in Table 2.1). The data were processed using the SPAM pipeline ([Intema et al. 2017](#)) which includes radio frequency interference (RFI) mitigation schemes, direction-dependent calibration, and ionospheric modelling ([Intema et al. 2009](#)). The final GMRT images at 325 MHz and 610 MHz are shown in Figure 2.3 and were obtained using the imaging parameters reported in Table 2.2. The flux density scale in the images was set by calibration on 3C48 (at 610 MHz) and 3C286 (at 325 MHz) using the models from [Scaife & Heald \(2012\)](#). We adopt a flux scale uncertainty of 10% for the GMRT observations (e.g. [Chandra et al. 2004](#)), which is quadratically added

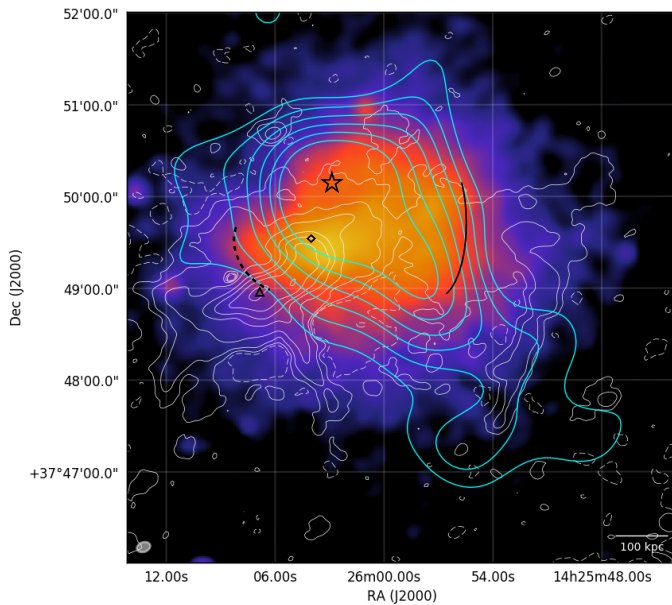


Figure 2.5: Full-resolution ($9'' \times 6''$) LOFAR image overlaid on an exposure-corrected, background-subtracted *Chandra* image in the 0.5-2.0 keV energy band with a total integration time of 22.9ks. The LOFAR contours (white) show the $(1,2,4,\dots) \times 5 \times \sigma_{\text{LOFAR}}$ levels and the dashed white contours show the $-3\sigma_{\text{LOFAR}}$, where $\sigma_{\text{LOFAR}} = 150 \mu\text{Jy beam}^{-1}$. The cyan contours are the weak lensing measurements showing the dark matter distribution. The star, square, and triangle show the peak of the dark matter distribution, X-ray peak, and radio peak, respectively. The solid black and dashed black line show the tentative location of the shock and cold front suggested by [Botteon et al. \(2018a\)](#).

to the (random) uncertainties of all flux density measurements in the GMRT images.

2.1.3 VLA data reduction

We obtained observations of Abell 1914 at 1.4 GHz from the VLA archive (projects AF367 and AF372). The cluster was observed in C and D configurations for 160 minutes each, using two 50 MHz-wide intermediate frequency (IF) channels centred at 1.365 and 1.435 GHz; only the low-frequency IF was found to be usable in the D-configuration observation because of RFI. The data were calibrated and reduced in the standard fashion using the NRAO Astronomical Image Processing System package (AIPS). Several loops of phase self-calibration were applied to reduce the effects of residual phase errors in the data. The C- and D-configuration data sets were first processed and self-calibrated separately, then combined together to produce the final images. The flux density scale was set using the [Perley & Butler \(2013\)](#) coefficients, which typically results in flux errors within 5%.

2.1.4 Chandra data reduction

X-ray images of Abell 1914 were produced using two ACIS-I *Chandra* observations taken in VFAINT mode (ObsID: 542, 3593), for a total exposure time of 26.9 ks. The contamination due to soft proton flares occurring during the observations was corrected by inspecting the light curves extracted in chip S3 using the `deflare` script. After this procedure, the net exposure time was 22.9 ks. The images we present were produced in the 0.5 – 2.0 keV band adding the two ObsIDs with the `merge_obs` routine. Data were analysed with CIAO v4.9 and *Chandra* CALDB v4.7.3. For more detailed description see [Botteon et al. \(2018a\)](#).

2.1.5 CFHT data

Abell 1914 was observed with MegaCam on the Canada-France-Hawaii Telescope (CFHT) as part of the Canadian Cluster Comparison Project (CCCP; [Hoekstra et al. 2012](#), [Mahdavi et al. 2013](#), [Hoekstra et al. 2015](#)). The main aim of this project was to study scaling relations, using weak gravitational lensing masses as reference. The *r*-band data we used were obtained with seeing < 0.8 arcsec with a total integration time of 4800 s. Further details about the data can be found in [Hoekstra et al. \(2012\)](#). In their most recent lensing analysis

Hoekstra et al. (2015) determined a mass of $M_{500} = (7.3 \pm 1.3) \times 10^{14} h_{70}^{-1} M_{\odot}$ using the location where the X-ray emission peaks as centre. For this paper we used the lensing measurements to reconstruct the projected mass surface density using the direct inversion algorithm from Kaiser & Squires (1993). The approach is identical to that described in Mahdavi et al. (2007) in their study of the complex merger Abell 520. The reconstruction is smoothed with a Gaussian smoothing kernel with a full width at half maximum (FWHM) of $60''$, which is the consequence of the limited number density of sources in ground-based data. The resulting mass reconstruction is shown in Figure 2.2 by purple contours. The cluster is clearly detected, as is the elongation along the merger direction. Moreover the results clearly indicate that the mass distribution peaks at the location of BCG 2.

2.1.6 Spectral index maps and integrated spectrum calculation

Table 2.2 lists the images made with the radio data and their corresponding resolution and sensitivity. These images were used to create a high-resolution spectral index maps between 150 MHz and 610 MHz. To sample the same spatial scales at both frequencies, we used the same inner uv range of 200λ to image both LOFAR and GMRT data. For the high-resolution spectral index map, we used a uv taper of $6''$. The resulting images were convolved with a Gaussian to produce images with the same restoring beam, accurately aligned in the image plane, and regridded onto the same pixel grid. Surface brightness below 3σ in respective images were masked. These images were then used to create spectral index maps where a power-law spectral index was calculated for each pixel. The error on the fit was calculated given the error on the LOFAR and GMRT pixel values (ΔS_1 and ΔS_2) with

$$\Delta\alpha = \frac{1}{\ln \frac{\nu_1}{\nu_2}} \sqrt{\left(\frac{\Delta S_1}{S_1}\right)^2 + \left(\frac{\Delta S_2}{S_2}\right)^2}, \quad (2.2)$$

where $\Delta S_i = \sqrt{(\sigma_i)^2 + (f S_i)^2}$ (with $i = [1, 2]$) is the total uncertainty associated with the measured flux density S_i and the subscripts stand for 150 MHz and 610 MHz, respectively, and f is the flux scale uncertainty as described in Section 2.1.2, for the LOFAR image. The total error propagation takes into account the flux scale uncertainty and, σ_i , the rms noise of the respective image. A similar procedure was used to create a low-resolution spectral index map

between 150 MHz and 1.4 GHz. The resulting spectral index images are shown in Figure 2.6.

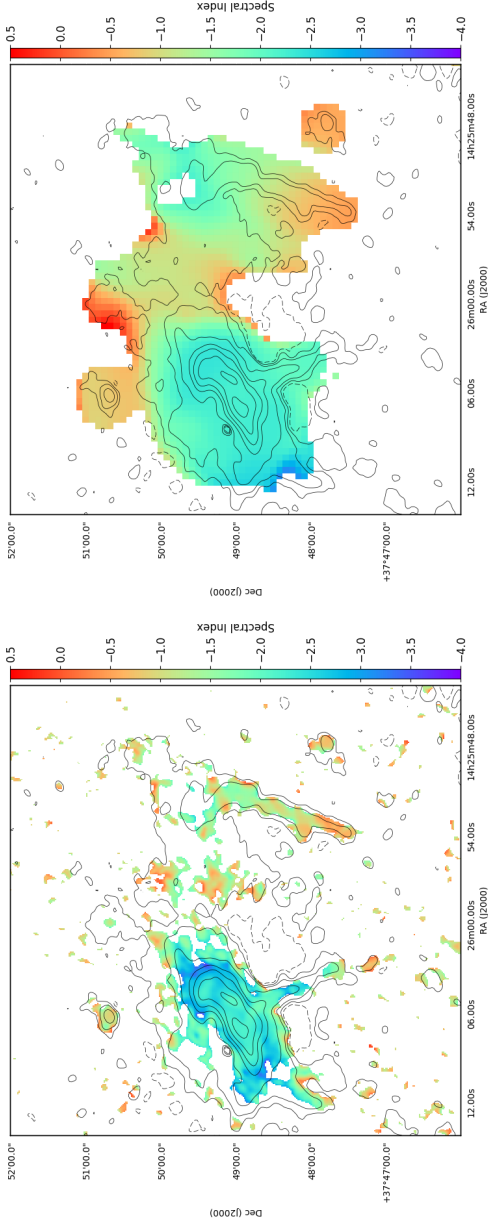


Figure 2.6: Spectral properties of emission from Abell 1914 at 150 MHz to 610 MHz high-resolution ($6'' \times 6''$) (left panel) and 150 MHz–610 MHz–1.4 GHz low-resolution $30'' \times 30''$ (right panel). In both figures, emission lower than 3σ has been blanked, where $\sigma_{\text{LOFAR}_{150,6\text{arcsec}}} = 175 \mu\text{Jy beam}^{-1}$, $\sigma_{\text{GMRT}_{610,6\text{arcsec}}} = 120 \mu\text{Jy beam}^{-1}$, $\sigma_{\text{LOFAR}_{150,30\text{arcsec}}} = 1500 \mu\text{Jy beam}^{-1}$, $\sigma_{\text{GMRT}_{610,30\text{arcsec}}} = 230 \mu\text{Jy beam}^{-1}$, and $\sigma_{\text{VLA}_{1.4,30\text{arcsec}}} = 51 \mu\text{Jy beam}^{-1}$

2.2 Results

In Figure 2.1 we labelled three main regions of diffuse emission associated with Abell 1914 which are discussed in the following sections.

2.2.1 RP: A radio phoenix candidate

The source RP is arguably the most interesting feature of this system. The source, classified as 4C38.39 is known to have a steep spectrum ($\alpha \sim -2$) and a possible curvature (Komissarov & Gubanov 1994, Roland et al. 1985). The RP consists of a bright, resolved region surrounded by fainter diffuse emission (see Figure 2.1). The bright region extends ~ 650 kpc in the NW-SE direction and ~ 230 kpc in the perpendicular direction. In the GMRT 325 MHz and 610 MHz images (Figure 2.3) the source RP is clearly detected, but the diffuse component surrounding it is marginally detected at 325 MHz. Figure 2.4 shows the low-resolution 150 MHz LOFAR and VLA 1.4 GHz images.

In order to measure the integrated spectral index of the source RP we made a set of new images (not shown) at all available radio frequencies with the same imaging parameters and matched minimum uv range. We measured the flux density over exactly the same area, defined by the 3σ contour of the LOFAR image (Figure 2.1) while excluding the RH region. The measured total flux densities at 150 MHz, 325 MHz, 610 MHz, and 1.4 GHz are $S_{150} = 4.68 \pm 0.46$ Jy, $S_{325} = 0.83 \pm 0.08$ Jy, $S_{610} = 0.277 \pm 0.02$ Jy, and $S_{1.4} = 34.8 \pm 2.0$ mJy, respectively. A single power-law fit gives an integrated spectral index measurement of $\alpha_{150-1400} = -2.17 \pm 0.11$ for the source RP. We used the LOFAR 150 MHz and GMRT 610 MHz higher resolution maps to create a resolved spectral index map. Figure 2.6 reveals a fairly uniform spectral index distribution with small variations; the spectral index value ranges from -1.9 to -2.3. The spectral index tends to get flatter in the southern direction. We used the additional flux measurements from Komissarov & Gubanov (1994) and plotted the spectrum of RP (Figure 2.7). We note that measurements in Komissarov & Gubanov (1994) were obtained using different imaging parameters than ours, which may have an impact on the relative accuracy between their measurements and ours. We fitted a line and a second order polynomial in log-log space to the data. The goodness of the fits was determined by the parameter sum of squares due to error (SSE), which measures the total deviation of the response values from the fit to the response values. The SSE values are 0.70 and 0.13 for the linear and second order polynomial fit, which suggests that the second order polynomial fit the data points better than the linear fit. Therefore, the spectrum shows hints

of possible spectral curvature, as suggested in Komissarov & Gubanov (1994). In order to confirm the curvature, we need additional, accurate measurements, especially at the lowest frequencies such as future LOFAR LBA (Low Band Antenna) observations.

In Figure 2.2 the weak lensing mass reconstruction based on the CFHT optical image shows that the total mass distribution (dominated by dark matter) roughly traces the galaxy distribution. The peak of the radio emission of RP (triangle marker) does not coincide with the nearby BCG positions (star markers). RP has an interesting extension towards the south-west, which we associate with an optical counterpart (circle marker, labelled RG). While an apparent tail of radio emission extends from RG towards RP, it is unclear if all radio emission in RP originates from RG. We do not identify any other obvious optical counterparts for RP. In Figure 2.5 the peak of the radio emission (triangle marker) does not coincide with the X-ray peak (square marker). The X-ray emission is elongated in the SE-NW direction, which is a similar orientation to the weak lensing mass reconstruction, but the latter is more elongated.

As a consequence of the extreme steep spectrum, combined with the filamentary morphology, peripheral location, misalignment with X-ray, and weak-lensing mass distribution, the source RP does not match the typical observational properties of giant radio haloes or radio relics, but it could be a radio phoenix. This is discussed in more detail in Section 2.3.

2.2.2 HT: A head-tail galaxy

We identify the source HT as a head-tail galaxy. In Figure 2.2 the CFHT r -band optical image is overlaid with the LOFAR 150 MHz map contours shows the optical counterpart of the head of the HT (marked as A). Another optical counterpart (B) is not a member of Abell 1914 (Sifón et al. 2015). The extent of the tail is 630 kpc in the NW direction. From the high-resolution spectral index map (Figure 2.6 left panel) we observe the typical steepening of the radio spectrum ($-0.89 \geq \alpha \geq -1.15$) along the length of the tail. The emission towards the end of the tail blends into the diffuse emission around the region of RP, which we discuss in the following section.

2.2.3 RH: A radio halo candidate

The faint emission region between sources RP and HT in Figure 2.1, labelled with RH, appears to be morphologically disconnected from the neighbouring sources. The region RH resembles radio halo emission, but cannot be traced

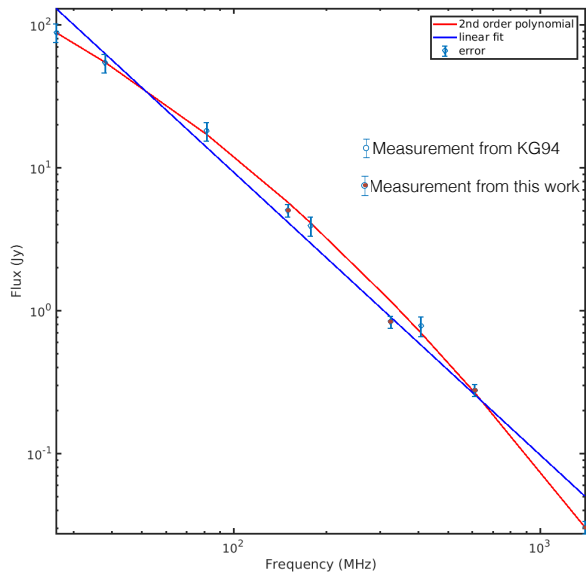


Figure 2.7: Total flux density as a function of frequency of the source RP. The brown points show the flux measurements at 150 MHz, 325 MHz, 610 MHz, and 1.4 GHz (this paper), while the blue points show the measurements from Komissarov & Gubanov (1994).

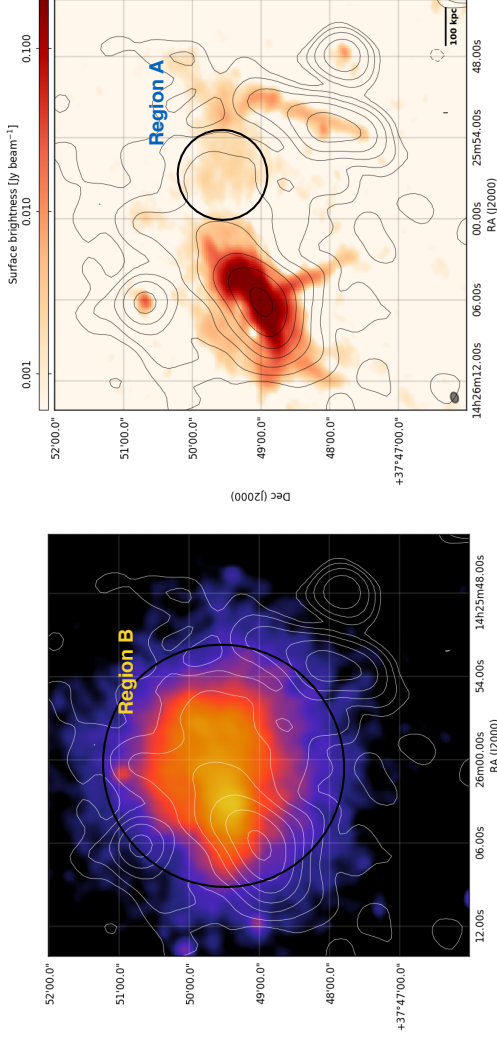


Figure 2.8: *Left panel:* Low-resolution, $30'' \times 30''$ VLA 1.4 GHz image contours overlaid on the *Chandra* image. The VLA contours (white) show the $(1,2,4,\dots) \times 3 \times \sigma_{\text{VLA}}$, where $\sigma_{\text{VLA}} = 55 \mu\text{Jy beam}^{-1}$. Region B was used to extrapolate the radio halo flux (see section 3.3). *right panel:* The same low-resolution VLA image contours (in black) overlaid on the LOFAR 150 MHz extended emission subtracted image. Region A shows the portion where the radio halo emission is not contaminated by the RP and HT.

over the full extent of the X-ray emission owing to the contaminating presence of both RP and HT. Large-scale emission in this region is also seen in low-resolution LOFAR 150 MHz and VLA 1.4 GHz images (Figure 2.4). Assuming it is part of a radio halo, we selected the region A (~ 70 kpc) as shown in Figure 2.8 (*right panel*) to calculate the flux density and spectral index. In this region, the halo emission is likely separated from the emission from RP and HT. From the 150 MHz LOFAR and 1.4 GHz VLA images we measure the integrated spectral index of the halo in region A to be $\alpha = -1.15 \pm 0.20$.

We estimate the radio halo power at 1.4 GHz using the VLA image. The measured total flux density of the region A is 2.34 ± 0.15 mJy. Using the 1.4 GHz flux measurements we calculated a k -corrected 1.4 GHz radio power $P_{1.4\text{GHz}} = 4\pi S_{1.4\text{GHz}} D_L^2 (1+z)^{-\alpha-1} = (1.94 \pm 0.14) \times 10^{23} \text{ W Hz}^{-1}$. The value of the radio power at 1.4 GHz is underluminous when compared with the $P_{1.4} - M_{500}$ relation presented in [Cassano et al. 2013](#). However, because of the contamination from RP, HT, and negative bowls around RP, the radio halo flux may be significantly underestimated. To show an example, we assume that the radio halo spans the region B (~ 1 Mpc diameter) as shown in Figure 2.8 (*left panel*). To calculate the total radio halo flux density in region B, we assume that it has the same surface brightness as region A. The extrapolated total flux density of region B is 18.72 ± 1.23 mJy. We note that the error does not properly reflect the intrinsic uncertainty of our assumptions. With this value of the radio halo flux density, we measure a k -corrected 1.4 GHz radio power $P_{1.4\text{GHz}} = (1.55 \pm 0.11) \times 10^{24} \text{ W Hz}^{-1}$. This value of the radio power falls within the scatter of the correlation presented in [Cassano et al. 2013](#).

We also attempted to separate possible radio halo emission from the emission of sources RP and HT by re-imaging the LOFAR data while leaving out the shortest baselines, which suppresses the extended emission and leaves only compact source emission. In principle, this source model could then be subtracted from the visibility data, leaving only extended emission in the data. However, the clean subtraction of a complex, bright source such as RP on a scale of > 100 kpc turns out to be too inaccurate to be of much practical use.

2.3 Discussion

The radio emission in Abell 1914 has previously been classified as an irregularly shaped radio halo with a steep spectrum (B03, G04) and a hint of spectral curvature ([Komissarov & Gubanov 1994](#)). With the new LOFAR observations, combined with archival GMRT, VLA, CFHT, and *Chandra* data, we are able

to separate the emission into three different components: a candidate radio phoenix, a possible radio halo and a tailed radio galaxy. These components are discussed below.

Radio phoenix

[Komissarov & Gubanov \(1994\)](#) suggested that the USS radio source 4C38.39 in Abell 1914 may indicate the presence of a very old radio galaxy. When the core of the radio galaxy had ceased its activity, the supply of fresh relativistic electrons into the radio lobes also stopped. Synchrotron losses of these electrons can explain the unusually steep spectrum nature. However, more recent studies of this source suggested it was part of a radio halo (B03, G04). The LOFAR and GMRT observations show that the properties of the emission in this region are quite distinct from those expected for a radio halo. Instead we note that this source very much resembles a radio phoenix source because (i) it has an unusually steep spectrum, (ii) the morphology of the source is quite filamentary when compared to a classical radio halo morphology, (iii) the X-ray morphology is displaced from the radio emission, and (iv) the source shows hints of having a curved spectrum.

Radio phoenixes are aged radio galaxy lobes whose emission is boosted by adiabatic compression (e.g. [Enßlin & Gopal-Krishna 2001](#), [Enßlin & Brüggen 2002](#)). There is evidence of these kind of sources in literature (e.g. [Slee et al. 2001](#), [van Weeren et al. 2009](#), [van Weeren et al. 2011](#), [Ogorean et al. 2011](#), [Cohen & Clarke 2011](#), [Stroe et al. 2013](#), [de Gasperin et al. 2015](#)). There is an interesting connection between the source RP and the radio galaxy (indicated with RG in Figure 2.2). RP can be a radio bubble detached by a shock from the tail of the radio galaxy (e.g. [Jones et al. 2017b](#)) unless the connection is just a projection effect. Besides adiabatic compression, shocks that are introduced by merging events might also be able to re-accelerate electrons via Fermi-type processes. However the hint of curvature and the fact that the source is very steep may rule out the possibility of shock acceleration, since in the case of shock acceleration the spectrum tends to get flatter (e.g. [Bonafede et al. 2014](#), [Botteon et al. 2016](#), [van Weeren et al. 2017](#)). Instead the above facts are more consistent with the adiabatic compression scenario. Therefore, detection of shocks near the location of RP is crucial to confirm the radio phoenix compression scenario.

[Botteon et al. \(2018a\)](#) suggested that the merging scenario in Abell 1914 is similar to that observed in the bullet cluster ([Markevitch et al. 2002](#)) where a subcluster is moving from the E to the W direction, producing a cold front in the direction of the motion. On the eastern side of Abell 1914, they claimed the

presence of a shock moving in the cluster outskirts, similar to the reverse shock found in the Buller cluster (Shimwell et al. 2015). Deeper X-ray observations are needed to confirm this.

Radio halo

In previous work, Abell 1914 was suggested to host a steep spectrum radio halo (B03, G04), but there the bright source 4C38.39 was assumed to be part of the halo. While the latter is likely not true, we do detect diffuse radio emission in between 4C38.39 and the tailed radio galaxy that might be part of a larger radio halo. The spectral index of the region RH is flatter than the tail of HT and RP (Figure 2.6 *right* panel). The measured, k -corrected 1.4 GHz radio power of the radio halo (region A in Figure 2.8) in Abell 1914 (discussed in Section 2.2.3) is $P_{1.4\text{GHz}} = (1.94 \pm 0.14) \times 10^{23}$ W/Hz. It is known that the radio power at 1.4 GHz and mass of the hosting cluster are correlated for giant radio haloes (e.g. Cassano et al. 2013). According to our estimates (Section 2.2.3) the luminosity of the halo in Abell 1914 is significantly smaller than previously thought (Cassano et al. 2013) and the halo appears to be underluminous with respect to expectations based on the radio power – mass correlation. Predictions suggest that USS radio haloes are underluminous when compared with the correlation (Cassano et al. 2010). However, at least for the region A, the low-resolution spectral index map between 150 MHz LOFAR, 325 MHz GMRT, 610 MHz GMRT, and 1.4 GHz VLA (Figure 2.6; *right* panel) suggests a spectral index of $\alpha = -1.15 \pm 0.20$. With the availability of current data there is no evidence of the radio halo being ultra-steep.

Recently hadronic models have also been invoked to explain underluminous radio haloes (Cuciti et al. 2018), but in these cases the radio halo should be centred on the X-ray peak location. So these models cannot explain the scenario in which the radio halo in Abell 1914 is underluminous. However, it is important to note that the measurement of the radio halo power is highly uncertain owing to the contamination from RP and HT. In Section 2.2.3 we also estimated the radio halo flux and corresponding radio halo power in a much larger region B (Figure 2.8) indicating that the value of the radio power can lie in between these two measurements. Higher resolution observations at GHz frequencies are needed to confirm the spectral properties of the radio halo.

Head-tail galaxy

The head of the head-tail galaxy on the west side of Abell 1914 was reported as a discrete source by B03, while the diffuse tail was unresolved and blended together with the other diffuse sources. In this paper, with the help of detailed spectral index maps, we classify this source unambiguously as a head-tail radio galaxy. From the spectral index maps (Figure 2.6) a clear spectral steepening can be observed towards its tail due to the synchrotron ageing. The disrupted X-ray morphology, mass distribution, and presence of a radio halo indicates that the cluster is undergoing a merger, but its effect on the HT is not clear. Initially the tail is more collimated and undisturbed, whereas the end of the tail seems to be more disrupted and blended with the radio halo emission. The spectral index at the end of the tail is similar to that of the radio halo emission, which could be the evidence for re-acceleration. In this scenario, old electrons in the turbulent end of the tail are mixed with the ICM and re-accelerated in the same way as radio halo particles are accelerated (which is still debated). [Botteon et al. \(2018a\)](#) suggested a presence of a shock (Figure 2.5) near the location in between RH and HT, which could also play a role in local particle re-acceleration.

2.4 Summary and conclusions

In this paper, we presented new LOFAR HBA radio observations at 150 MHz of the merging galaxy cluster Abell 1914. We also analysed GMRT and VLA data and presented high- and low-resolution spectral index maps. These allowed us to constrain spectral properties of this system. We summarise the main results as follows:

Abell 1914 was thought to host a radio halo but with quite unusual properties. With the new LOFAR observations at high resolution ($9'' \times 6''$) we were able to properly resolve the radio structure, which was not possible in previous studies. With the new resolved radio maps, we find that the overall radio emission of Abell 1914 is unlikely to be a single radio halo but rather the superposition of a revived fossil plasma source, a radio halo, and a head-tail radio galaxy.

We characterise the revived fossil plasma source as a radio phoenix candidate. The source RP (Figure 2.1) has an integrated spectral index measurement of -2.17 ± 0.11 with a possible curvature (Figure 2.7). Usually these sources are thought to be old fossil plasma, originating from a dead radio galaxy, which

has been adiabatically compressed by the passage of shocks (Enßlin & Gopal-Krishna 2001; Enßlin & Brüggén 2002). The hint of curvature and ultra-steep nature probably rules out the possibility of shock acceleration. Botteon et al. (2018a) do not find clear evidence of a shock near the vicinity with the present shallow X-ray observations. Deeper X-ray observations are needed to confirm this.

The possible presence of a faint radio halo is inferred from emission in a region that seems not to be contaminated by radio phoenix or head-tail emission. Based on our estimates, the radio halo appears underluminous with respect to its mass, as predicted by the $P_{1.4GHz} - M_{500}$ correlation plot presented by Cassano et al. (2013). Usually USS radio haloes are underluminous in the correlation plot. However, in the region of the halo where it is possible to measure the spectrum, we find the spectral index to be -1.15 ± 0.20 . It is important to note that the measured value of the radio power is uncertain and may significantly be underestimated because of the possible contamination from RP and HT.

From the radio intensity and spectral index maps (Figures 2.1 and 2.6) we identify a head-tail radio galaxy with an optical counterpart in the head and a clear spectral steepening towards its tail. One interesting aspect is the connection of the tail with the assumed radio halo emission, which could be a source of mildly relativistic electron injection. A few other examples of possible connections between radio haloes and head-tail galaxies are found in Wilber et al. (2018) and Rajpurohit et al. (2018).

Acknowledgments

We thank the anonymous referee for useful comments. This paper is based (in part) on data obtained with the International LOFAR Telescope (ILT) under project code LC0.037. LOFAR (van Haarlem et al. 2013) is the LOw Frequency ARray designed and constructed by ASTRON. It has observing, data processing, and data storage facilities in several countries, which are owned by various parties (each with their own funding sources) and are collectively operated by the ILT foundation under a joint scientific policy. The ILT resources have benefited from the following recent major funding sources: CNRS-INSU, Observatoire de Paris and Université d'Orléans, France; BMBF, MIWF-NRW, MPG, Germany; Science Foundation Ireland (SFI), Department of Business, Enterprise and Innovation (DBEI), Ireland; NWO, The Netherlands; and The Science and Technology Facilities Council, UK. We thank the staff of the GMRT who made these observations possible. GMRT is run by the National Centre

for Radio Astrophysics of the Tata Institute of Fundamental Research. This paper is based on the data obtained with the International LOFAR Telescope (ILT). RJvW acknowledges support from the ERC Advanced Investigator programme NewClusters 321271 and the VIDI research programme with project number 639.042.729, which is financed by the Netherlands Organisation for Scientific Research (NWO). DNH acknowledges support from the ERC Advanced Investigator programme NewClusters 321271. F.d.G. is supported by the VENI research programme with project number 1808, which is financed by the Netherlands Organisation for Scientific Research (NWO). AD acknowledges support by the BMBF Verbundforschung under the grant 05A17STA. Basic research in radio astronomy at the Naval Research Laboratory is supported by 6.1 Base funding. This research made use of APLpy, an open-source plotting package for Python hosted at <http://aplpy.github.com>.

Chapter 3

Revived fossil plasma sources in galaxy clusters

Based on
S. Mandal, H. T. Intema, R. J. van Weeren, T. W. Shimwell, A. Botteon,
G. Brunetti, F. de Gasperin, M. Brügger, G. Di Gennaro, R. Kraft,
H. J. A. Röttgering, M. Hardcastle, C. Tasse
A&A 634, A11 (2020)

Abstract

It is well established that particle acceleration by shocks and turbulence in the intra-cluster medium can produce cluster-scale synchrotron emitting sources. However, the detailed physics of these particle acceleration processes is still not well understood. One of the main open questions is the role of fossil relativistic electrons that have been deposited in the intracluster medium (ICM) by radio galaxies. These synchrotron-emitting electrons are very difficult to study as their radiative lifetime is only tens of Myr at gigahertz frequencies, and they are therefore a relatively unexplored population. Despite the typical steep radio spectrum due to synchrotron losses, these fossil electrons are barely visible even at radio frequencies well below the gigahertz level. However, when a pocket of fossil radio plasma is compressed, it boosts the visibility at sub-gigahertz frequencies, creating what are known as radio phoenixes. This compression can be the result of bulk motion and shocks in the ICM due to merger activity. In this paper we demonstrate the discovery potential of low-frequency radio sky surveys to find and study revived fossil plasma sources in galaxy clusters. We used the 150 MHz TIFR GMRT Sky Survey (TGSS) and the 1.4 GHz NVSS sky survey to identify candidate radio phoenixes. A subset of three candidates was studied in detail using deep multi-band radio observations (LOFAR and GMRT), X-ray observations (*Chandra* or *XMM-Newton*), and archival optical observations. Two of the three sources are new discoveries. Using these observations, we identified common observational properties (radio morphology, ultra-steep spectrum, X-ray luminosity, dynamical state) that will enable us to identify this class of sources more easily, and will help us to understand the physical origin of these sources.

3.1 Introduction

Galaxy clusters are the largest gravitationally bound systems in the Universe. Their main mode of growth is through accretion of smaller groups of galaxies, and through major mergers with other clusters. A huge amount of gravitational binding energy of the order of $\sim 10^{64}$ ergs is released when galaxy clusters merge (e.g. [Kravtsov & Borgani 2012](#)). This energy strongly affects the physical properties of the different constituents of clusters (e.g. the density distribution and velocity dispersion of the galaxies) and the temperature, metallicity, and density distribution of the X-ray emitting thermal intracluster medium (ICM). Cluster mergers also generate shocks that cause density and temperature jumps

(Markevitch & Vikhlinin 2007) and turbulence in the ICM, which can amplify magnetic fields ($\sim \mu\text{G}$), affect the spatial transport, and (re)-accelerate relativistic particles (Lorentz factor $\gamma > 1000$). This particle acceleration can lead to cluster-scale synchrotron emission most commonly in the form of central radio halos and peripheral radio relics (see e.g. van Weeren et al. 2019 for recent observational reviews, and Brunetti & Jones 2014 for a theoretical review). The spectral index (α)¹ of this emission is generally steep ($\alpha \lesssim -1$), making it relatively bright at radio frequencies below a few hundred MHz.

Radio halos are extended ($\gtrsim 1$ Mpc) diffuse radio sources at the centre of merging clusters (e.g. Cassano et al. 2010; Cuciti et al. 2015; Kale et al. 2015), with a morphology similar to the X-ray morphology of the system. Radio halos have been discovered in ~ 50 disturbed clusters (e.g. van Weeren et al. 2019). Observational evidence collected in the last decade suggests that they are caused by the continuous acceleration of electrons in turbulent gas (Brunetti et al. 2001; Petrosian 2001, Brunetti & Lazarian 2007). In addition, continuous injection of secondary particles through proton-proton collisions (Dennison 1980, Enßlin et al. 2011) can be re-accelerated together with the primary electrons (Brunetti & Lazarian 2011, Pinzke et al. 2017) in these regions, and may play a role in the generation of radio halos. However, the lack of gamma ray detection puts constraints on such a mechanism (e.g. Brunetti et al. 2017 and references therein).

Apart from radio halos, diffuse radio sources in clusters can be broadly divided into radio relics (e.g. Kempner et al. 2004; van Weeren et al. 2019) and radio phoenixes (revived fossil plasma sources). Cluster radio relics are elongated linearly polarised ($>10\%$ - 30% at GHz frequencies) regions (~ 1 - 2 Mpc) at the cluster outskirts, which typically have a convex morphology with respect to the cluster centre and exhibit a radio spectral steepening towards the cluster centre (van Weeren et al. 2010; Bonafede et al. 2012; Stroe et al. 2013; de Gasperin et al. 2015; Kierdorf et al. 2017). Radio relics are generally found to trace merger-induced shock waves (e.g. Finoguenov et al. 2010; Bourdin et al. 2013; Akamatsu & Kawahara 2013; Shimwell et al. 2015; Botteon et al. 2016; Eckert et al. 2016; Urdampilleta et al. 2018). The particle (re)-acceleration processes at the location of radio relics is still debated. There are cases where the luminosity of the radio relics is much higher than expected from diffuse shock acceleration (DSA) of electrons in the thermal pool (e.g. Brunetti & Jones 2014, Botteon et al. 2016, van Weeren et al. 2016a, Botteon et al. 2019). Therefore, the role of fossil plasma (seed particles) in the ICM has been invoked, as simulations

¹ $S \propto \nu^\alpha$, where S is the measured flux density and ν is the observed frequency

Cluster name / Target	RA (J2000)	Dec (J2000)	Redshift (z)	Arcsec to kpc conversion
Abell 2593	23 ^h 24 ^m 13.0 ^s	+14°41'38"	0.041	0.811
SDSS-C4-DR3-3088	09 ^h 46 ^m 45.4 ^s	+54°25'37"	0.046	0.904
Abell 2048	15 ^h 15 ^m 09.7 ^s	+04°24'37"	0.097	1.797

Table 3.1: Target list of three TGSS clusters with their properties, as given in the literature.

indicate that (re)-acceleration of seed relativistic electrons is more efficient than the DSA (e.g. Kang & Ryu 2015).

Radio phoenixes are a less widely studied class of diffuse radio sources in the ICM, and are thought to be a manifestation of fossil plasma in galaxy clusters. Likely candidates for the fossil electrons are lobes and tails of radio galaxies, which have ultra-steep spectra (USS) due to synchrotron aging and inverse Compton (IC) losses. After being deposited in the ICM, these fossil electrons are visible only for tens of Myrs at GHz frequencies. When an aged lobe or tail is compressed (e.g. by a merger shock), the electrons are re-energised which boosts their visibility at sub-GHz frequencies (Enßlin & Gopal-Krishna 2001; Enßlin & Brüggen 2002). Sources powered by this mechanism can maintain electrons at higher energies than what radiative cooling alone would allow. Although deposited locally, when given enough time, fossil plasma can occupy a significant fraction of the (turbulent) ICM due to advection and diffusion. The relative importance of this mechanism to explain the origin of the other diffuse cluster radio sources (halos, relics) is unclear. To date, only a few radio phoenixes have been found using low-frequency observations of clusters (e.g. Slee et al. 2001; Kempner et al. 2004; van Weeren et al. 2009; van Weeren et al. 2011; de Gasperin et al. 2015, Mandal et al. 2019). Even though radio tails and lobes are abundant in clusters, the ultra-steep nature of these sources makes it hard to identify, especially from large-area sky surveys at GHz frequencies. To firmly establish radio phoenixes as a distinct class of objects, it is crucial to identify their common observable and physical properties for comparison with radio halos and relics. Identifying common observational properties also enables an efficient search for more radio phoenixes, which in itself will help us to better understand the nature and physical mechanisms behind this relatively unexplored population of radio sources.

Radio sky surveys below 300 MHz such as the VLA Low-frequency Sky Survey (VLSS; Cohen et al. 2007; Lane et al. 2012; Lane et al. 2014), the GaLactic and Extragalactic All-sky Murchison Wide-field Array Survey (GLEAM; Wayth et al. 2015, Hurley-Walker et al. 2017), and the LOFAR Multi-frequency Snapshot Sky Survey (MSSS; Heald et al. 2015) have a great potential for discovery in this area, but the low spatial resolution of these surveys makes it difficult to distinguish between diffuse radio emission and emission from individual active radio galaxies. The TIFR GMRT Sky Survey (TGSS ADR; Intema et al. 2017) is a high-resolution sky survey at 150 MHz. The combination of very large area (about 37,000 square degrees, all radio sky between -53° and $+90^\circ$), high resolution ($25''$), and high sensitivity ($2\text{-}5\text{ mJy beam}^{-1}$ rms noise) makes the TGSS a very suitable resource to search for radio phoenixes based on their

diffuse morphology, ultra-steep radio spectrum, and location in galaxy clusters.

In this paper we present a pilot study for identifying the properties of radio phoenixes and their interplay with the dynamics and properties of the hosting clusters from multi-band radio observations, complemented with optical and X-ray observations. We selected 11 radio phoenix candidates from the TGSS based on their morphology, steep spectra, and location (see Section 3.2). For three of the candidates, we were able to obtain data sets at three different radio (LOFAR 150 MHz, GMRT 325 MHz, and 610 MHz) and X-ray (*Chandra* or *XMM-Newton*) bands, which we present in this paper as an exploratory study. The layout of the paper is as follows. In Section 3.2 we present the method of the sample selection. In Section 3.3 we describe the observations and data reduction methods. In Section 3.4 we discuss the results deduced from the radio, X-ray, optical, and spectral index images of these sources, followed by a discussion in Section 3.5 and our conclusions in Section 3.6.

Throughout the paper we assume a Λ CDM cosmology with $H_0 = 70$ $\text{kms}^{-1}\text{Mpc}^{-1}$, $\Omega_m = 0.3$, and $\Omega_\Lambda = 0.7$. All sky coordinates are epoch J2000 coordinates.

Source	LOFAR 150 MHz (120-168)MHz	GMRT 325 MHz (308-340)MHz	GMRT610 MHz (594-626)MHz	Chandra (0.5-2.0)keV	XMM-Newton (0.5-2.0)keV
Abell 2593	8.33 h	3.83 h	3.18 h	7 ks	NA
SDSS-C4-DR3-3088	8.33 h	3.68 h	3.55 h	17 ks	NA
Abell 2048	8.33 h	10 h	10 h	NA	68 ks

Table 3.2: Observation Details (on-source time) of Abell 2593, SDSS-C4-DR3-3088 and Abell 2048.

Source Name	Frequency (MHz)	Robust	Taper ($''$)	Θ_{FWHM} " \times "", (PA)	σ_{rms} $\mu\text{Jy beam}^{-1}$
Abell 2593	LOFAR 150	-0.5	0	9 \times 6, (75.45)	220
	GMRT 325	-0.5	0	11 \times 7, (18.53)	66
	GMRT 610	-0.5	0	5 \times 4, (20.75)	38
SDSS-C4-DR3-3088	LOFAR 150	-0.25	0	6 \times 6, (90.00)	80
	GMRT 325	-0.25	0	13 \times 7, (46.18)	43
	GMRT 610	-0.25	0	7 \times 4, (-21.82)	40
Abell 2048	LOFAR 150	-0.5	0	13 \times 6, (85.74)	266
	GMRT 325	-0.5	0	11 \times 8, (66.60)	125
	GMRT 610	-0.5	0	8 \times 5, (-63.51)	117

Table 3.3: Imaging parameters and image properties of the LOFAR and GMRT maps of Abell 2593, SDSS-C4-DR3-3088, and Abell 2048. The beam position angle (PA) is measured in degrees from north through east.

Cluster	$\langle kT \rangle$ (keV)	Metallicity (Z) (Z_{\odot})	R_{500} (kpc)	M_{500} $M_{\odot} \times 10^{14}$
Abell 2593	4.16 ± 0.28	$0.28^{+0.19}_{-0.17}$	1011^{+33}_{-35}	$3.06^{+0.31}_{-0.30}$
SDSS-C4-DR3-3088	3.13 ± 0.41	$0.79^{+0.53}_{-0.37}$	829^{+59}_{-65}	$1.69^{+0.39}_{-0.36}$
Abell 2048	4.15 ± 0.10	$0.55^{+0.06}_{-0.06}$	982^{+12}_{-11}	$2.97^{+0.10}_{-0.11}$

Table 3.4: Global properties of the clusters derived from X-ray observations. Quoted errors are at the 1σ confidence level. R_{500} and M_{500} are derived using the scaling relations from [Arnaud et al. \(2005\)](#).

3.2 Sample selection

To search for candidate radio phoenixes in galaxy clusters, we convolved the TGSS images (resolution $25''$) to the resolution of the NRAO VLA Sky Survey (NVSS; [Condon et al. 1998](#): resolution $45''$) images, combined the two, and identified extended steep-spectrum emission. We selected sources based on the following properties:

- An ultra-steep radio spectrum ($\alpha \leq -2$);
- A 150 MHz total flux density $S_{150} \geq 30$ mJy (detection above $\sim 10\sigma$);

- A morphology compatible with diffuse cluster emission (no point sources associated with dead active galactic nuclei (AGNs));
- Located in the vicinity (within 1 Mpc) of a known cluster position from the SDSS cluster catalogue by [Wen et al. 2012](#) or the ROSAT All-Sky Survey (RASS; [Voges et al. 1999](#)) catalogue.

The limiting values of the spectral index and flux density in selecting the sample is somewhat arbitrary, aimed at identifying very steep-spectrum, extended, and relatively bright candidates to enable a more detailed study using follow-up observations. This bright sample is likely the tip of the iceberg of the population, and in this way the contamination of other types of sources (such as radio relics and halos) is also minimal. Our final sample consists of 11 candidate revived fossil plasma sources. For this study we performed follow-up observations for three of the sources with LOFAR 150 MHz, GMRT 325 MHz, GMRT 610 MHz, and *Chandra* and/or *XMM-Newton* X-ray observations. An overview of these three objects is given in Table 3.1. The detailed observation summary is given in Table 3.2. The remainder of our sample will be followed up with future observations.

3.3 Observations and methods

3.3.1 GMRT data reduction

We observed two of our targets (Abell 2593 and SDSS-C4-DR3-3088) with the GMRT at 325 and 610 MHz (project codes 31_018 and 33_014), while for the third target (Abell 2048) we used archival observations at the same frequencies (project codes 15HRA01 and 16_065). The data were processed using the SPAM pipeline ([Intema et al. 2017](#)), which includes radio frequency interference (RFI) mitigation schemes, direction-dependent calibration, and ionospheric modelling ([Intema et al. 2009](#)). The final full-resolution GMRT images are shown in the middle panels of Figures 3.1, 3.2, and 3.3, and were created using the imaging parameters listed in Table 3.3. The flux densities were set using calibration on 3C286 (at 325 MHz) and 3C48 (at 610 MHz) using the models from [Scaife & Heald \(2012\)](#). We adopted a flux uncertainty of 10% for GMRT observations ([Chandra et al. 2004](#)), which is quadratically added to the uncertainties of all flux density measurements from the GMRT observations.

3.3.2 LOFAR data reduction

All three sources presented in this paper were observed with the LOFAR at 150 MHz (project codes LC9_027 for Abell 2593 & Abell 2048, and LC6_015 for SDSS-C4-DR3-3088) in HBA_DUAL_INNER mode. The LOFAR data were processed with the standard direction-independent (DI) calibration pipeline² as described in van Weeren et al. (2016a) and Williams et al. (2016) to correct for DI effects (see de Gasperin et al. 2019 for a description of the latest version of this pipeline). The processing was performed on computer facilities that are local to the LOFAR long-term archive sites to mitigate issues with downloading large quantities of data to local compute clusters (see Mechev et al. 2018). After DI calibration was completed, the data were processed with the latest version of the LoTSS (Shimwell et al. 2017 and Shimwell et al. 2019) direction-dependent (DD) calibration and imaging pipeline that will be presented in detail in Tasse et al., (in prep.) and is also summarised in Shimwell et al. (2019, Sect. 5.1). This pipeline makes use of KMS (Tasse 2014 and Smirnov & Tasse 2015) for DD calibration, and DDFacet (Tasse et al. 2018) is used to apply the DD calibration solutions during the imaging.

After completion of the LoTSS data processing pipeline, a post-processing step is conducted to subtract all the sources except for the targets and to calibrate in the directions of the targets. This post-processing procedure will be described in van Weeren et al. (in prep.).

Due to normalisation issues and inaccurate beam models, LOFAR flux scales can show systematic offsets that need to be corrected by comparison with other surveys (van Weeren et al. 2016b, Hardcastle et al. 2016). We cross-matched catalogues of LOFAR point sources near the targets with the TGSS (Intema et al. 2017). The adopted correction factor is approximately 15% on the LOFAR flux densities that were derived from the total flux density ratio between the LOFAR and the TGSS.

3.3.3 Spectral index maps and integrated spectrum calculation

In Table 3.3 we list the properties of the images made with the radio data. These images were used to create high-resolution spectral index maps for 150 MHz, 325 MHz, and 610 MHz. In order to sample the same spatial scales at all frequencies, we remade the images using the same inner uv -range of 200λ for all the radio frequencies. Only for Abell 2048 was an inner uv -range of 600λ used to

²<https://github.com/lofar-astron/prefactor>

suppress ripples caused by calibration errors on shorter baselines. The uv -taper parameter was varied for individual data sets (see Table 3.3). The resulting images were convolved with a 2D Gaussian to produce images with the same restoring beam size, accurately aligned in the image plane, and re-gridded onto the same pixel grid. To calculate the spectral index maps, only pixels with a surface brightness $> 3\sigma$ that were detected in at least two images were used (where σ is the local rms background noise). These masked images were then used to create spectral index maps where a power-law function was fit for each pixel. The errors in the spectral index were calculated taking into account the image noise and a flux scale uncertainty of 15% for LOFAR and 10% for GMRT. Spectral index error maps are included in Appendices A and B.

3.3.4 X-ray data reduction

Abell 2593 and SDSS-C4-DR3-3088 were observed with *Chandra* ACIS-I in VFaint mode as part of the GTO program (Obs IDs 20780 and 20781). Abell 2048 was already observed twice with EPIC on board *XMM-Newton* in full-frame mode (Obs IDs 0653810601 and 0760230301). We retrieved these data sets (see Table 3.2 for more details) and analysed the *Chandra* data with CIAO v4.11 and CALDB v4.8.2, while we made use of the ESAS implemented in SAS v16.1.0 to process the *XMM-Newton* data. The observations were reduced following standard reduction procedures, including the removal of bad pixels, screening for periods affected by soft proton flares, and detection and excision of point sources prior to spectral extraction. We used the 0.5-2.0 keV energy band to produce the cluster images shown in this paper.

Spectral analysis was performed with XSPEC v12.10.0c (Arnaud 1996) to derive global properties of the clusters. Given the low redshifts of Abell 2593 and SDSS-C4-DR3-3088 and their large angular extent in the ACIS-I field of view (FoV), we made use of the *Chandra* blank sky field data sets scaled by the ratio of the 9.5-12 keV count rates to estimate the local background. The larger FoV of *XMM-Newton* and smaller angular size of Abell 2048 allowed us to perform accurate modelling of the background components in a cluster-free region. We followed Ghirardini et al. (2019), adopting their phenomenological model for the non-X-ray background and an astrophysical component composed of the combined cosmic X-ray background together with the Galactic foreground emission in the direction of the cluster. The ICM emission was modelled with an absorbed thermal plasma model PHABS*APEC, fixing the redshift of the cluster to the value given in Table 3.1 and the column density to the Galactic absorption value towards the target (Kalberla et al. 2005). The normalisation,

temperature, and metallicity (solar abundance table by [Asplund et al. 2009](#)) of the APEC model were free to vary in the fit.

Derivation of the cluster global properties

We derived the global temperature and metallicity of the clusters from spectra extracted in the region $0.1 \times R_{500} < r < 0.4 \times R_{500}$, a choice that is commonly used in the literature to avoid the effect of the cool core (if present), and obtained values at the virial radius. As R_{500} is not known for our clusters, we used an iterative approach to compute $\langle kT \rangle$ and R_{500} (see [Liu et al. 2018](#), [Mernier et al. 2019](#)): we first fixed R_{500} arbitrarily and evaluated the corresponding $\langle kT \rangle$, then we used the scaling relations of [Arnaud et al. \(2005\)](#) to compute R_{500} (and M_{500}) and compared it with the new $\langle kT \rangle$ obtained until we obtained a self-consistent result. The global properties of the clusters are summarised in Table 3.4.

3.4 Results

Our three radio phoenix candidates are associated with the clusters as listed in Table 3.1. A list of global cluster properties (temperature, metallicity, R_{500} , and M_{500}) as derived from the X-ray observations is provided in Table 3.4. We first discuss the results for the three individual radio sources in their respective clusters.

3.4.1 Abell 2593

The galaxy cluster Abell 2593 is located at a redshift of $z = 0.041$ with an Abell richness class of $R = 0$ ([Ulmer et al. 1981](#)). The top left panel of Figure 3.1 shows the image of the X-ray gas overplotted with the contours of the 150 MHz radio emission (in white) as seen by LOFAR. The morphology of the X-ray emission appears roundish and we do not see strong evidence for elongation of the emission in any particular direction, as is typically the case for merging clusters. However, the X-ray emission is not peaked at the centre, suggesting that the dynamical state could be somewhat disturbed.

The radio source in this cluster has a filamentary morphology with distinctive features. The top right panel shows the high-resolution LOFAR 150 MHz image of the source that extends 450 kpc in the SE-NW direction (labelled regions A and C), and an elongated structure extending about 200 kpc in the NE direction

(region B). There is a hint of diffuse emission towards the SW (region D). The middle left and right panels of Figure 3.1 show the GMRT 325 and 610 MHz images, respectively. The GMRT 325 MHz image has a very similar morphology to the LOFAR 150 MHz image, but there is an apparent disconnection towards the south of region B. Region A has a similar morphology in the GMRT 610 MHz image as well, but we do not detect the significant emission in regions B and D. In addition, the radio emission in region C is very faint in the GMRT 610 MHz image, which is indicative of steep-spectrum radio emission. The bottom left panel shows the LOFAR 150 MHz contours (in red) overlaid on an SDSS r-band image (Wen et al. 2012) of Abell 2593. The brightest cluster galaxy (labelled BCG) is associated with a compact radio source visible in all three radio maps. Two other optical galaxies (RG1-A and RG2-A) are also found to be associated with radio emission. The peak of the X-ray emission coincides with the BCG position. Given that it is a poor cluster of galaxies (since it is of low mass), it is hard to determine the dynamical state of the cluster based on very few galaxy cluster members.

In order to measure the integrated radio spectral index of the different regions of the radio emission Abell 2593, we made a set of images (not included in this paper) at all available radio frequencies with identical imaging parameters and minimum uv -range (see Section 3.3.3 for details). The integrated flux densities of the whole source measured over the same area (defined by the 3σ contours of the LOFAR image) at 150 MHz, 325 MHz, and 610 MHz are $S_{150} = 3.57 \pm 0.36$ Jy, $S_{325} = 1.45 \pm 0.15$ Jy, and $S_{610} = 0.69 \pm 0.07$ Jy, respectively. A single power-law fit gives an integrated spectral index measurement of $\alpha_{150-325-610} = -1.17 \pm 0.12$. This is less steep than the integrated spectral index measured between 150 MHz TGSS and 1.4 GHz NVSS flux densities. This apparent discrepancy is discussed in Section 3.5. We used the LOFAR 150 MHz, GMRT 325, and 610 MHz maps to create a spatially resolved spectral index map (see Section 3.3.3) to look for trends in the variation of α at a resolution of $20''$. The bottom right panel of Figure 3.1 shows the spectral index distribution across the source. The spectral index values at the location of RG1-A and RG2-A (region A) are -0.8 (flat). For the source RG1-A, the spectral index steepens in the NW direction to a value of -1.7. Regions B and C are more uniformly steep with small variations ranging from -1.7 to -2.0. Region D has a very steep spectral index value of -3.0. We note that the compact radio emission from the BCG has a spectral index of -0.7.

The integrated spectral index value of the entire source from 150 MHz to 325 MHz–610 MHz is not very steep due to the contributions of the radio flux at the location of RG1-A, RG2-A, and the BCG and is not an accurate repre-

sentation of the spectral index of the diffuse regions of the source. The spectral index value tends to get steeper when we add flux density measurements from 1.4 GHz NVSS images, which suggests a possibly curved spectrum at higher frequencies. However, deeper 1.4 GHz observations are needed in order to confirm the spectral curvature.

3.4.2 SDSS-C4-DR3-3088

The galaxy cluster SDSS-C4-DR3-3088 is located at a redshift of $z = 0.046$. Sixty-one cluster members were spectroscopically confirmed by [Simard et al. \(2009\)](#). The top left panel of Figure 3.2 shows the 150 MHz LOFAR image contours overlaid on our *Chandra* X-ray image. The peak in the diffuse X-ray emission resides towards the east of the radio source at a large distance of 500 kpc (labelled as the ‘X-ray peak’). We note that this peak is due to the contribution from a point source (CGCG 265-040, $z = 0.047$; [Yang et al. 2007](#)). Since the X-ray emission is irregular in morphology, it suggests that the cluster could be dynamically disturbed.

The top right panel shows the 150 MHz LOFAR image of the radio source. The middle left and right panels show the GMRT 325 and 610 MHz images, respectively. In all the images the radio source has an irregular filamentary morphology with what looks to be a wide-angle radio tail. Regions of interest have been indicated on the LOFAR 150 MHz image. Starting from region A, the source extends about 400 kpc in the NW direction. There is a linear feature along the edge of the source 500 kpc in length. In the LOFAR 150 MHz image, this linear feature appears to be connected to a compact source (labelled RG). However, this extension of the diffuse emission is not recovered in the GMRT 325 MHz and 610 MHz images, suggesting that it is steep-spectrum emission. The central ‘Filaments’ region is detected at all radio frequencies. The radio source gives of an oddly shaped radio tail wedge with RG-A in its focus. The morphological connection of RG-A with the larger scale radio emission is persistent across all radio frequency bands, which strongly suggests a physical connection. The bottom left panel of Figure 3.2 shows the SDSS r-band image of the cluster overlaid with the LOFAR 150 MHz contours in red. We do not identify any optical counterpart to the compact radio source RG (see top right panel). Given the fairly low redshift of the cluster ($z = 0.046$), this likely means that the compact radio source is a background object at higher redshift, and the apparent connection with the diffuse emission at 150 MHz is a chance alignment. We find an optical galaxy at the location of RG-A, which we identify as its host. The brightest cluster galaxy is located near the peak in the X-ray

emission (outside the extent of the optical image).

To measure the integrated spectral index of the source, a set of new images was made with the same uv -range in order to match same spatial scales in all available radio frequencies (see Section 3.3.3 for details). The measured integrated flux densities of the source over exactly the same area (defined by the 3σ contours of the LOFAR image) at 150 MHz, 325 MHz, and 610 MHz are $S_{150} = 1.83 \pm 0.18$ Jy, $S_{325} = 0.45 \pm 0.50$ Jy, and $S_{610} = 0.16 \pm 0.02$ Jy. A single power-law fit gives an integrated spectral index measurement of $\alpha_{150-610} = -1.74 \pm 0.23$. We also used the NVSS image to calculate the total flux density and adding this extra frequency point; the single power-law fit gives an integrated spectral index measurement of $\alpha_{150-1400} = -2.00 \pm 0.06$. This suggests that there could be a hint of curvature at the higher frequency. To create a high-resolution ($7''$) spectral index map (same method as in Section 3.4), we only used the LOFAR 150 MHz and 610 MHz (excluding the GMRT 325 MHz map), which is shown in Figure 3.2, bottom right panel. The spectral index at the location of the optical host galaxy RG-A is -0.8. The spectral index steepens in the NW direction over a distance of 100 kpc (region A) to a value of -1.3. The filaments have an overall steep spectral index distribution that is flatter than the surrounding diffuse emission. The linear feature has a spectral index value ranging from -1.3 to -1.5 prior to the ‘Filaments’ region. The diffuse emission apparently connecting to the source RG (Figure 3.2 *left* panel) has the steepest spectral index with a value of -3.0 (See Appendix B for additional spectral index maps).

3.4.3 Abell 2048

Abell 2048 is a galaxy cluster located at a redshift of $z = 0.0972$ (Struble & Rood 1999). The top left panel of Figure 3.3 shows the LOFAR 150 MHz contours (in white) overplotted on a background-corrected *XMM-Newton* X-ray image. The brightest cluster galaxy of the system is labelled BCG (and lies outside the extend of the radio and optical images). The morphology of the X-ray emission is slightly elongated along the NW-SE direction and is not strongly peaked at the centre. This could indicate that the dynamical state of this cluster is disturbed.

The steep-spectrum radio source is located at the outskirts of the cluster. The top right panel in Figure 3.3 shows the 150 MHz LOFAR image of the filamentary radio source with a complex morphology. The largest extent of the source is 400 kpc. Three distinctive arm-like features are marked in the same figure. There is a hint of a connection between the extension of ‘Arm-3’ and

the compact source labelled ‘RG’. In the middle panel we show the GMRT 325 MHz and GMRT 610 MHz images in the left and right panel, respectively. At 610 MHz most of the diffuse emission in the arms is faint, suggesting it has a very steep radio spectrum. [van Weeren et al. \(2011\)](#) presented the VLA 1.4 GHz image in ‘C’ configuration, which confirms the steep nature of the diffuse emission, and set an upper limit on the polarisation fraction of 8% for the source.

The bottom left panel shows the optical DSS2 r-band image of the cluster overlaid with the LOFAR 150 MHz contours in red. We identified the elliptical galaxy MCG+01–39–011 ($z = 0.095$) as the host of the radio source RG based on accurate co-location. There are no other obvious optical counterparts associated with the radio emission in the arms, although several cluster galaxies lie within the arm areas.

In order to measure the spectral properties of the radio source in Abell 2048, we used the same uv -range to re-image the data set in all available radio frequencies (see Section 3.3.3 for details). The measured integrated flux densities of the source are $S_{150} = 1.57 \pm 0.25$ Jy, $S_{325} = 0.50 \pm 0.05$ Jy, and $S_{610} = 0.17 \pm 0.02$ Jy as measured at 150 MHz, 325 MHz, and 610 MHz, respectively. A single power-law fit gives an integrated spectral index measurement of $\alpha_{150-610} = -1.59 \pm 0.17$. We also recalculated the integrated spectral index value by adding the 1.4 GHz VLA total flux density measurement (from [van Weeren et al. 2011](#)). The resulting value of $\alpha_{150-1400} = -1.94 \pm 0.20$ suggests that the radio source possibly has a curved spectrum. We re-imaged the LOFAR and GMRT observations to make a high-resolution spectral index map, which is shown in Figure 3.3 (bottom left panel). The value of the spectral index is uniformly steep (on average) in the arm regions with $\alpha = -1.65 \pm 0.10$ with small variations. No particular trend (flattening or steepening) of the spectral index is noticed along any direction. The spectral index of the source RG is flat with a value of $\alpha = -0.8$.

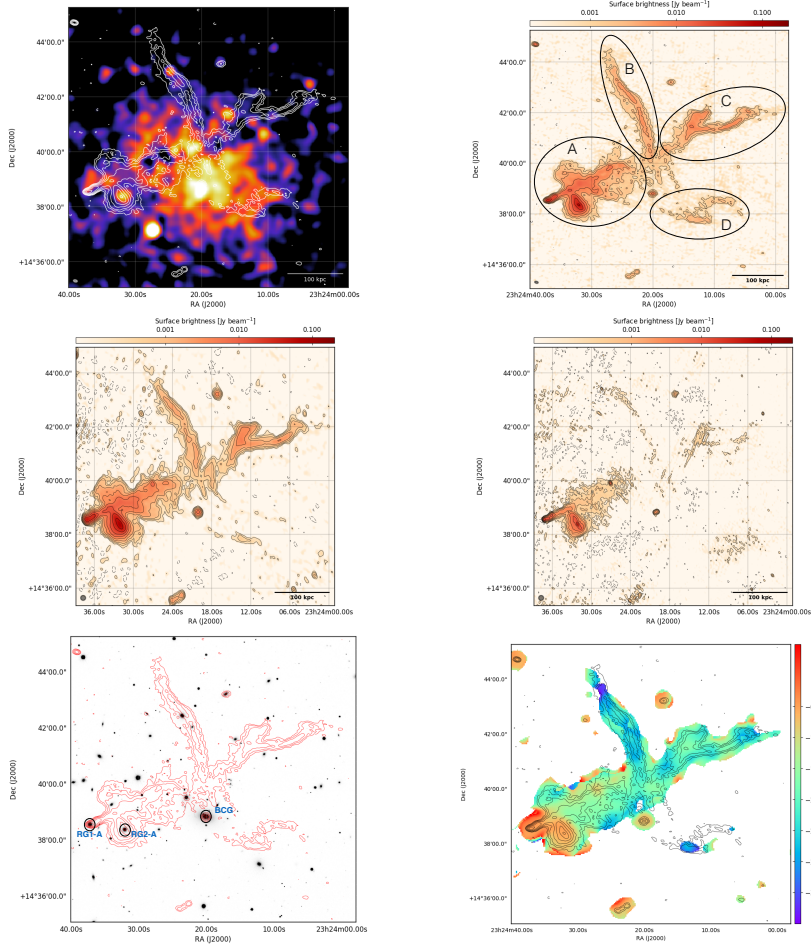


Figure 3.1: *Top left* panel: Full-resolution LOFAR image contours (white; as shown in the *right* panel) of Abell 2593, overlaid on an exposure-corrected *Chandra* image in the 0.5-2.0 keV energy band with a total integration time of 7ks. *Top right* panel: 150 MHz LOFAR image ($9'' \times 6''$). The black contours and dashed lines show the $(1,2,4,\dots) \times 5 \times \sigma_{\text{LOFAR}150}$ and $-3 \times \sigma_{\text{LOFAR}150}$ levels, respectively, where $\sigma_{\text{LOFAR}150} = 219 \mu\text{Jy}/\text{beam}$. *Middle left* panel: 325 MHz GMRT image ($11'' \times 7''$). The black contours and dashed lines show the $(1,2,4,\dots) \times 5 \times \sigma_{\text{GMRT}325}$ and $-3 \times \sigma_{\text{GMRT}325}$ levels, respectively, where $\sigma_{\text{GMRT}325} = 66 \mu\text{Jy}/\text{beam}$. *Middle right* panel: 610 MHz GMRT image ($5'' \times 4''$). The black contours and dashed lines show the $(1,2,4,\dots) \times 5 \times \sigma_{\text{GMRT}610}$ and $-3 \times \sigma_{\text{GMRT}610}$ levels, respectively, where $\sigma_{\text{GMRT}610} = 38 \mu\text{Jy}/\text{beam}$. *Bottom left* panel: LOFAR 150 MHz contours (shown in the *top left* panel) in red overlaid on an SDSS r-band image of Abell 2593. The labelled galaxies (RG1-A and RG2-A) are the possible counterparts for the radio emission of regions A and C. The BCG label indicates the brightest cluster galaxy. *Bottom right* panel: LOFAR 150 MHz contours (shown in the *top right* panel) overplotted on the high-resolution ($20'' \times 20''$) spectral index map of Abell 2593.

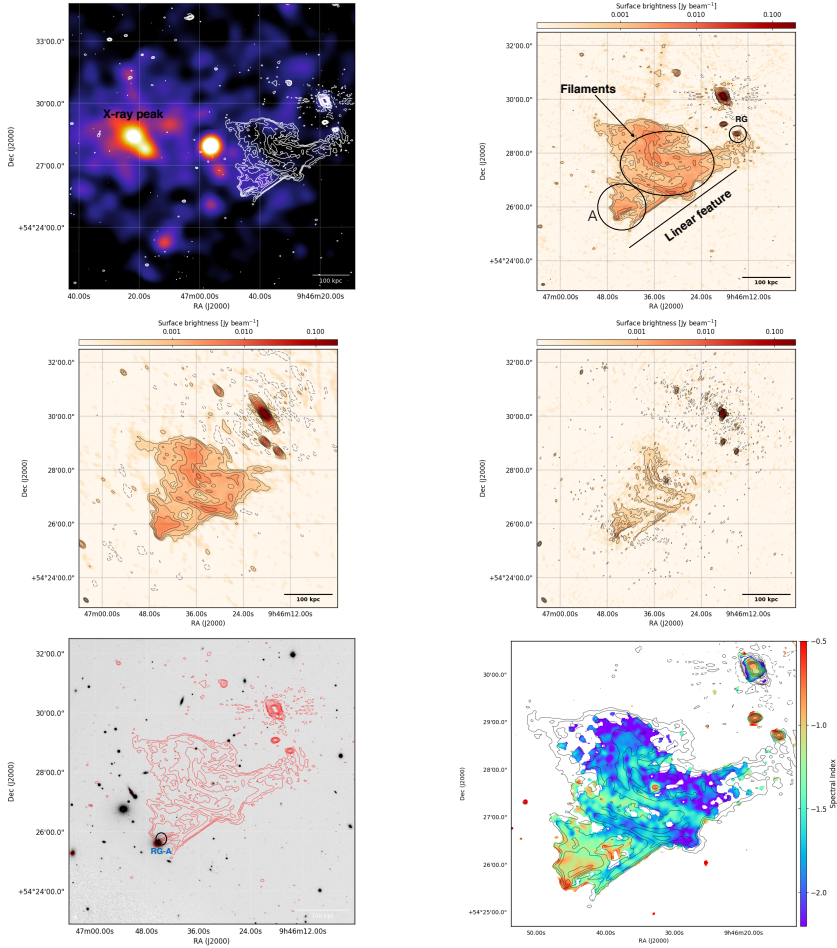


Figure 3.2: *Top left* panel: Full-resolution LOFAR image contours (white; as shown in the *right* panel) of SDSS-C4-DR3-3088, overlaid on an exposure-corrected *Chandra* image in the 0.5-2.0 keV energy band with a total integration time of 17ks. *Top right* panel: 150 MHz LOFAR image of SDSS-C4-DR3-3088 ($6'' \times 6''$). The black contours and dashed lines show the $(1,2,4,\dots) \times 5 \times \sigma_{\text{LOFAR}150}$ and $-3 \times \sigma_{\text{LOFAR}150}$ levels, respectively, where $\sigma_{\text{LOFAR}150} = 80 \mu\text{Jy}/\text{beam}$. *Middle left* panel: 325 MHz GMRT image ($13'' \times 7''$). The black contours and dashed lines show the $(1,2,4,\dots) \times 5 \times \sigma_{\text{GMRT}325}$ and $-3 \times \sigma_{\text{GMRT}325}$ levels, respectively, where $\sigma_{\text{GMRT}325} = 43 \mu\text{Jy}/\text{beam}$. *Middle right* panel: 610 MHz GMRT image ($6'' \times 4''$). The black contours and dashed lines show the $(1,2,4,\dots) \times 5 \times \sigma_{\text{GMRT}610}$ and $-3 \times \sigma_{\text{GMRT}610}$ levels, respectively, where $\sigma_{\text{GMRT}610} = 40 \mu\text{Jy}/\text{beam}$. *Bottom left* panel: LOFAR 150 MHz contours (shown in left panel in red) overlaid on an SDSS r-band image of SDSS-C4-DR3-3088. A possible optical counterpart is labelled RG-A. *Bottom right* panel: LOFAR 150 MHz contours (shown in the top *right* panel) overplotted on the high-resolution ($7'' \times 7''$) spectral index map of SDSS-C4-DR3-3088.

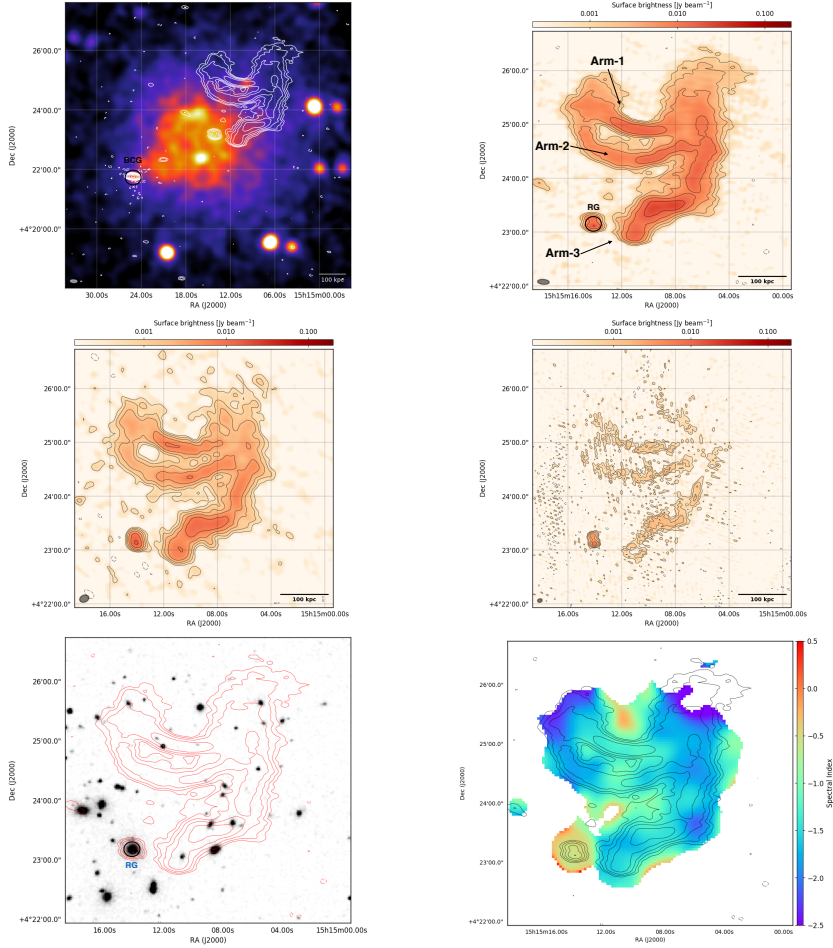


Figure 3.3: *Top left* panel: Full-resolution LOFAR image contours (white; shown in the *top right* panel) of Abell 2048, overlaid on an exposure-corrected background-subtracted *XMM-Newton* image in the 0.5–2.0 keV energy band with a total integration time of 68 ks. *Top right* panel: 150 MHz LOFAR image ($13'' \times 6''$) of the source Abell 2048. The black contours and dashed lines show the $(1,2,4,\dots) \times 5 \times \sigma_{\text{LOFAR}150}$ and $-3 \times \sigma_{\text{LOFAR}150}$ levels, respectively, where $\sigma_{\text{LOFAR}150} = 266 \mu\text{Jy}/\text{beam}$. *Middle left* panel: 325 MHz GMRT image ($11'' \times 8''$) of Abell 2048. The black contours and dashed lines show the $(1,2,4,\dots) \times 5 \times \sigma_{\text{GMRT}325}$ and $-3 \times \sigma_{\text{GMRT}325}$ levels, respectively, where $\sigma_{\text{GMRT}325} = 125 \mu\text{Jy}/\text{beam}$. *Middle right* panel: 610 MHz GMRT image ($8'' \times 5''$) of Abell 2048. The black contours and dashed lines show the $(1,2,4,\dots) \times 5 \times \sigma_{\text{GMRT}610}$ and $-3 \times \sigma_{\text{GMRT}610}$ levels, respectively, where $\sigma_{\text{GMRT}610} = 117 \mu\text{Jy}/\text{beam}$. *Bottom left* panel: LOFAR 150 MHz contours (shown in the *left* panel in red) overlaid on an DSS2 r-band image of Abell 2048. A possible optical counterpart is labelled RG. *Bottom right* panel: LOFAR 150 MHz contours (shown in the *top right* panel) overlaid on the high-resolution ($20'' \times 20''$) spectral index map of Abell 2048.

3.5 Discussion

In this paper, we present a multi-wavelength study of three ultra-steep spectrum diffuse radio sources in galaxy clusters. The morphology of these sources does not fit with a scenario in which they are mere aged confined bubbles from AGNs in the ICM. Also, the spectral index shows patchy structures with no clear trend within the source. In addition, the kinematic age (travel time of the electrons in the ICM) of the source (\sim gigayear) is much larger than the radiative lifetime (\sim megayear) of the electrons; which suggests re-energisation of the electrons occurs at the location. Although limited in numbers, this study aims to explore the properties of this relatively unexplored class of sources to look at possible common characteristics and the connection with the dynamical properties of the hosting cluster. Below we discuss the common physical properties of these sources based on these observations.

3.5.1 AGN connection

All these sources show a very filamentary, irregular morphology at low radio frequencies. As shown in the results section, these sources are morphologically connected with an AGN: RG1-A, RG2-A for Abell 2593; RG-A for SDSS-C4-DR3-3088; and RG for Abell 2048. Spectral index values at these locations are of the order of -0.7, which is in agreement with the injection spectral index of an AGN, and the spectral index tends to steepen along the tail of the radio galaxy.

3.5.2 Spectral index

The three sources have an overall ultra-steep radio spectrum. The relatively strong low-frequency emission traces an old population of electrons because high-energy electrons age due to synchrotron and IC losses and are visible only for tens of Myrs. Old lobes of radio galaxies (AGNs) are one of the main candidates for these fossil plasma. The measured integrated spectral index for 150 MHz, 325 MHz, and 610 MHz is less steep than the index measured for 150 MHz, 325 MHz, 610 MHz, and 1400 MHz (see Section 4.1), which suggests that there might be curvature towards higher frequencies. Deep observations at 1.4 GHz are needed to confirm this. It is important to note that all the sources have a non-uniform spectral index across the source. This suggests that there could be a possible mix of cosmic-ray populations with different ages, losses, and re-acceleration efficiencies. Therefore, the re-energisation of these particles can also be different across the source. So, even though there is a hint of curvature

in the integrated spectral index, the sources should not be interpreted as a reservoir of homogeneous cosmic-ray population. In addition, we note that the integrated spectral indices of these sources are much steeper than the classical radio relics (Feretti et al. 2012).

3.5.3 Mass, temperature, dynamical state, and position of the radio source in the cluster

In Table 3.4 we list the derived mass and the global temperature of each galaxy cluster, which shows that they are only moderately massive ($M_{500} < 10^{15} M_{\odot}$). Most of the previously discovered radio phoenix candidates (apart from the one in Abell 1914; Mandal et al. 2019) tend to be located in less massive systems of galaxy clusters. In the same table we see that the radio sources reside well within the R_{500} value and extend about 500 kpc. This means that the radio sources are located within the ICM towards the cluster centre. Deeper X-ray observations are needed in order to map the temperature in different regions and characterise the merger dynamics more accurately. However, the apparent disturbed morphologies of these clusters suggest that the systems could be unrelaxed and undergoing minor mergers. Although radio phoenix candidates with highly disturbed clusters also exist (e.g. Abell 1914; Mandal et al. 2019 and Abell 2443; Clarke et al. 2013), a clear connection of a shock with a radio phoenix is still missing.

Interpretation

Ultra-steep spectrum radio sources in clusters with complex filamentary morphologies have sporadically been seen in previous studies (e.g. Slee et al. 2001, Kempner et al. 2004) and were characterised as relic or ghost radio galaxies and proposed to name these radio phoenixes. It has been speculated that the origin of these sources are AGNs. Slee et al. (2001) showed that the estimated travel time of the brightest cluster galaxies are much longer than the modelled ages of relic radio sources, and a nearby bright elliptical galaxy always provided a decent match as a candidate source of origin. Based on our observations and results, the sources presented in this paper also appear to belong to the same class of objects.

Shocks and ICM motion can affect the morphology of ghost plasma or bubbles. Recent simulations of cluster radio galaxy tails, passing through ICM shocks or with large relative motions, show filamentary morphologies and ultra-steep and curved spectra (Nolting et al. 2019) similar to what is observed. Ear-

lier it was proposed that shocks can compress the radio plasma if it is still poorly mixed with the ICM. This compression re-energises the electrons to boost their visibility at frequencies below a few hundred MHz (Enßlin & Gopal-Krishna 2001, Enßlin & Brüggen 2002).

Another scenario for the formation of these ultra-steep spectrum sources in clusters invokes shock re-acceleration of fossil plasma through the Fermi-I mechanism (DSA; e.g. Kang & Ryu 2015). This will flatten the curved radio spectrum and if the shock is strong enough, the spectrum follows a power-law distribution, as is typically the case for giant radio relics. Contrary to re-acceleration, compression only shifts the spectrum in the flux-frequency space without changing the underlying shape.

For our sources we found spatially non-uniform spectral indices. Together with the observed filamentary morphologies, this suggests a different degree of mixing of the relativistic particles from the AGNs with the ICM. This means that the compression scenario proposed by Enßlin & Gopal-Krishna (2001) does not explain all the aspects. The in-homogeneous mixing of relativistic particles with the ICM implies an averaging effective adiabatic index ($(4/3) < \gamma_{ad} < (5/3)$) value, which consequently leads to different effective compression ratios across the source. Under these conditions and driven by a complex cluster dynamics, plasma instabilities may also play an important role in the re-acceleration of particles within the radio sources. These mechanisms cannot be modelled by existing numerical simulations. Recently, however, with the help of low-frequency (sub-GHz) observations, de Gasperin et al. 2017 showed the possibility of an interplay between fossil plasma and the perturbed ICM which can gently re-accelerate relativistic particles injected by AGNs of the galaxy cluster Abell 1033. If this kind of gentle re-acceleration mechanism is common for aged plasma in clusters of galaxies, it could provide a seed population of relativistic electrons and a possible connection between radio galaxies and re-acceleration mechanisms in radio halos or radio relics. An example of this scenario could be the Abell 3411-3412 galaxy cluster pair, where van Weeren et al. 2017 showed a morphological connection between a radio galaxy and a radio relic.

3.6 Conclusion

In this paper we studied three ultra-steep spectrum sources in galaxy clusters based on radio and X-ray observations. We found that these three sources i) have complex filamentary radio morphology, ii) show hints of curved spectra, and iii) are probably related to AGN fossil radio plasma. Based on these properties, we

conclude that these sources belong to the category of ‘radio phoenixes’, as was defined by [Kempner et al. \(2004\)](#).

In this work we found that these three sources are located in galaxy clusters that are low mass ($\lesssim 10^{15} M_{\odot}$) and have an un-relaxed dynamical state. This provides support for the scenario that phoenixes are connected with shocks and/or ICM motions. In addition, we determined that these sources have spatially non-uniform spectral indices. This suggests a different degree of mixing of the relativistic particles from the AGNs with the ICM and implies that several mechanisms are operating for the re-energisation of the plasma.

With the advancement of low-frequency radio telescopes and data processing techniques, upcoming high-resolution and sensitive surveys at or below 150 MHz (such as LoTSS at 150 MHz; [Shimwell et al. 2019](#), $6''$, $100 \mu\text{Jy}/\text{beam}$; LoLSS at 50 MHz; de Gasperin et al. in prep., $20''$, $1.5 \text{ mJy}/\text{beam}$) will be excellent tools for identifying many more revived fossil plasma sources in galaxy clusters, enabling statistical analysis of larger samples.

Acknowledgments

We thank the anonymous referee for useful comments. This paper is based (in part) on data obtained with the International LOFAR Telescope (ILT) under project code LC9_027 and LC6_015. LOFAR ([van Haarlem et al. 2013](#)) is the Low Frequency Array designed and constructed by ASTRON. It has observing, data processing, and data storage facilities in several countries, that are owned by various parties (each with their own funding sources), and that are collectively operated by the ILT foundation under a joint scientific policy. The ILT resources have benefitted from the following recent major funding sources: CNRS-INSU, Observatoire de Paris and Université d’Orléans, France; BMBF, MIWF-NRW, MPG, Germany; Science Foundation Ireland (SFI), Department of Business, Enterprise and Innovation (DBEI), Ireland; NWO, The Netherlands; The Science and Technology Facilities Council, UK; Ministry of Science and Higher Education, Poland; Istituto Nazionale di Astrofisica (INAF), Italy. We thank the staff of the GMRT that made these observations possible. GMRT is run by the National Centre for Radio Astrophysics of the Tata Institute of Fundamental Research. This paper is based on the data obtained with the International LOFAR Telescope (ILT). The Leiden LOFAR team acknowledge support from the ERC Advanced Investigator programme NewClusters 321271 and the VIDI research programme with project number 639.042.729, which is financed by the Netherlands Organisation for Scientific Research (NWO). MJH acknowledges

support from STFC [ST/R000905/1]. This research made use of APLpy, an open-source plotting package for Python hosted at <http://aplpy.github.com>.

3.A Spectral index error map

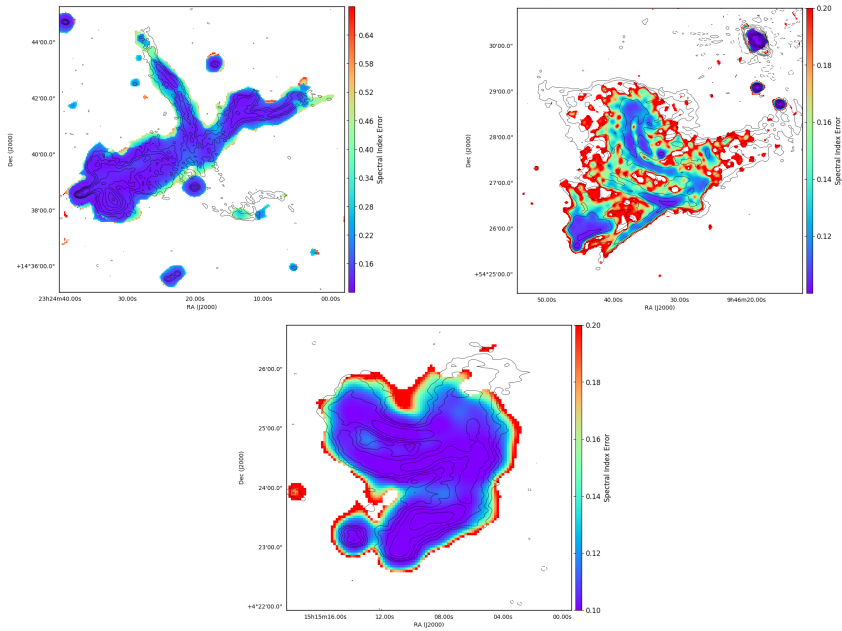


Figure 3.4: Spectral index error maps of Abell 2593, SDSS-C4-DR3-3088, and Abell 2048. The overplotted contours are the same as in the LOFAR 150 MHz images for each sources.

3.B Additional spectral index and error maps of SDSS-C4-DR3-3088

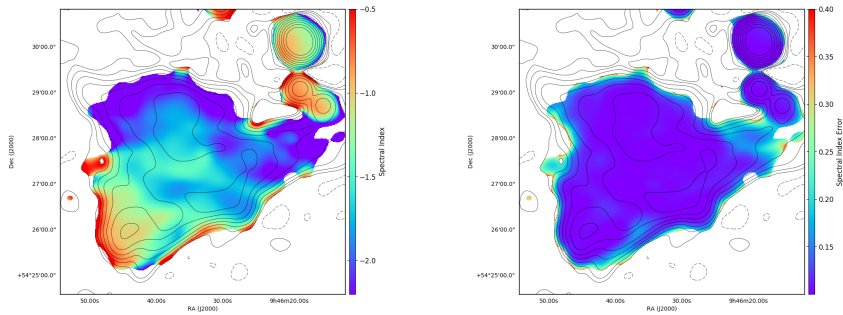


Figure 3.5: Low-resolution ($22''$) spectral index and error maps of SDSS-C4-DR3-3088.

Chapter 4

Towards a sample of radio phoenices in galaxy clusters

Based on
S. Mandal, R. J. van Weeren, T. W. Shimwell, H. T. Intema, A. Botteon,
F. de Gasperin, G. Di Gennaro, M. Grespan, G. Brunetti, M. Brüggen,
M. Brienza, F. Gastaldello, M. J. Hardcastle, H. Röttgering, R. Kraft,
R. Cassano, A. Drabent, M. Hoeft, D. Jung, L. K. Morabito, A. Shulevski,
W. L. Williams et al. Submitted to A&A

Abstract

Over the last decade, it has been well established that shocks and turbulent motions in the intra-cluster medium (ICM) generated through cluster mergers can produce observable large scale synchrotron emission. However, the related particle acceleration mechanisms responsible for these phenomena are still not clearly understood. In addition, the complexity of objects observed has put the traditional taxonomy of diffuse radio sources as consisting of radio halos and radio relics into question. In order to explain the acceleration efficiencies for radio relics and radio halos, the presence of fossil plasma has been suggested. Old lobes of radio galaxies are one of the key candidates for the source of these mildly relativistic particles. Typically these lobes have an ultra-steep spectrum because the high-energy radio emitting electrons would have lost their energy due to synchrotron and inverse Compton (IC) losses. However, with plasma instabilities driven by complex cluster dynamics and their interplay with the ICM that can re-energise old fossil electrons to emit observable radio waves again, these sources of emission are known as radio phoenixes. In this paper we present an observational overview of all the known radio phoenixes. Out of 25 sources that are presented, 8 are discoveries that we present here and for these we show results from new radio (GMRT and/or LOFAR) and, for a subset, X-ray observations. The sample allows us to study the common physical properties of radio phoenixes (such as radio morphology, dynamical state of the host cluster, location of the phoenixes inside the cluster and spectral behaviour) to establish the nature of this relatively unexplored class of objects. These radio phoenixes are found to have an AGN origin and are located well within the R_{500} of the clusters. Presence of dynamical disturbance in the cluster supports the formalism that they are associated with ICM motion and or shocks. Finally, while these revived fossil plasma sources are found to have a curved spectra at higher frequencies, presence of non-uniform spectral indices suggests that they should not be thought to represent a reservoir of uniform cosmic-ray population.

4.1 Introduction

Clusters of galaxies are the grow via the accretion of smaller groups of galaxies and through major mergers with other clusters of galaxies. Galaxy cluster mergers release a huge amount ($10^{63} - 10^{64}$ ergs) of energy into the Intra-cluster medium (ICM) (e.g. [Kravtsov & Borgani 2012](#)). This released binding energy strongly affects the physical properties of the ICM ([Markevitch & Vikhlinin](#)

2007). In addition, a fraction of energy can be channeled into non-thermal components, relativistic particles and magnetic fields, that produce observable synchrotron emission on cluster scale (Brunetti & Jones 2014). The synchrotron emission has a steep spectra ($S \propto \nu^\alpha$; where α is the spectral index, S is the total flux density and ν is the observed frequency) and is observed in the form of radio halos, radio relics etc. (van Weeren et al. 2019).

Radio halos are extended (~ 1 Mpc) diffuse radio sources which has a morphology and centroid that roughly matches the X-ray emission from the thermal ICM (e.g. Cassano et al. 2010, Kale et al. 2015, Cuciti et al. 2015). The most favoured scenario suggests that radio halos are formed by continuous (re)-acceleration of electrons due to turbulence generated from cluster mergers (Brunetti et al. 2001, Petrosian 2001, Brunetti & Lazarian 2007, Brunetti & Lazarian 2011, Miniati & Beresnyak 2015, Brunetti & Lazarian 2016, Pinzke et al. 2017). Recently it has been proposed by Brügggen & Vazza (2020) that these mechanisms may also be responsible for radio bridges between clusters (Botteon et al. 2018b, Govoni et al. 2019).

Radio relics are linearly polarised (10% to 30% at GHz frequencies) and have an elongated morphology. They are located at the outskirts of merging clusters and are thought to trace shock waves (Ensslin et al. 1998, van Weeren et al. 2010, Finoguenov et al. 2010, Bonafede et al. 2012, Bourdin et al. 2013, Akamatsu & Kawahara 2013, Stroe et al. 2013, de Gasperin et al. 2015, Shimwell et al. 2015, Botteon et al. 2016, Urdampilleta et al. 2018 etc). Diffusive shock acceleration (DSA: a Fermi I mechanism) had primarily been proposed to be responsible for the non-thermal energy gain of the particles at shock fronts (Ensslin et al. 1998, Roettiger et al. 1999). However, recent observations have put this framework into question. In a fraction of cases, it has been shown that the acceleration efficiency is not high enough to generate such bright radio relics with electrons from the thermal pool (e.g. Botteon et al. 2016, Eckert et al. 2016, van Weeren et al. 2016a, Botteon et al. 2019). In this regard, the role of seed particles (fossil plasma) in the ICM has been invoked, since re-acceleration of seed electrons is more efficient than that the DSA (Markevitch et al. 2002, Kang et al. 2012, Kang & Ryu 2015).

Radio phoenixes are a less widely studied class of objects that are thought to be a manifestation of fossil plasma in the ICM (Kempner et al. 2004, van Weeren et al. 2019). Lobes and tails of radio galaxies in clusters are likely candidates for these fossil electrons. When the central AGN of a radio galaxy switches off and there is no supply of freshly injected particles, the so-called ‘AGN remnant lobes’ can diffuse into the surrounding medium. After being deposited in the ICM, electrons from these lobes are only visible for tens of

Myrs at higher (\sim GHz) frequencies. Due to adiabatic and radiative losses, their spectrum becomes steep ($\alpha \leq -1.2$) and curved. The fossil plasma becomes invisible and hard to detect, even at sub GHz frequencies (Brienza et al. 2017, Hardcastle 2018, English et al. 2019). However, in a cluster environment, these low-energy relativistic ($\gamma \sim 100$) electrons can still be poorly mixed with the ICM (Sarazin 1999; Petrosian 2001; Pinzke et al. 2013).

When (weak) shocks generated from cluster mergers pass through these old radio lobes, they can adiabatically compress and re-energize the electrons, thereby boosting their visibility at lower-radio (hundreds of MHz) frequencies (Enßlin & Gopal-Krishna 2001, Enßlin & Brüggen 2002). Thus these revived fossil plasma sources provide us with a unique opportunity to study this otherwise invisible populations of electrons. Although these fossil electrons are deposited locally, over time, due to advection and turbulent diffusion, they can occupy a large fraction of ICM. Therefore, old radio lobes could provide a seed population of relativistic electrons and a possible connection between radio galaxies and re-acceleration mechanisms in both radio halos and relics. For example, de Gasperin et al. (2017) showed evidence of an interplay between fossil radio plasma and the perturbed ICM which appeared to gently re-accelerate relativistic particles injected by an AGN. Also, it has been shown that shocks generated through cluster mergers can power radio relic type sources by re-accelerating electrons of AGN origin (van Weeren et al. 2017). However, the relative importance of these mechanisms to explain the diffuse radio sources, is not fully understood and to date, only few radio phoenixes have been discovered (Slee et al. 2001, Kempner et al. 2004, van Weeren et al. 2009, van Weeren et al. 2011, de Gasperin et al. 2015, Di Gennaro et al. 2018, Mandal et al. 2020). In order to understand the acceleration mechanisms responsible for the generation of radio phoenixes, it is crucial to identify their common observational and physical properties and compare them with those of radio halos and relics. This will also help in establishing radio phoenixes as a distinct class of objects and enable us in better understanding of the physics of particle acceleration and the nature of this relatively unexplored population. Even though fossil electrons from radio lobes in clusters of galaxies are abundant, their ultra-steep nature makes them hard to be identify at high (GHz) frequencies. Due to the ultra-steep spectral nature of these sources, large area surveys at low frequencies (\sim below 300 MHz) are ideal to look for radio phoenixes. One promising example, is the TIFR GMRT Sky Survey (TGSS ADR; Intema et al. 2017) which is a $25''$ resolution sky survey at 150 MHz which covers the radio sky between -53° to $+90^\circ$ (approximately 90%) with a sensitivity of $2\text{-}5\text{mJy beam}^{-1}$ rms noise.

As part of a pilot study, we discovered 11 new radio phoenix candidates.

In [Mandal et al. \(2020\)](#), we presented detailed follow-up (radio and X-ray) observations for three of these sources. In this paper, we present the results from the follow-up observations for the other 8 sources, for one of which, polarisation results are also included. In addition, we extend our sample of radio phoenixes by including all the previously known candidates we are aware of in the literature (see Section 4.2 for details) and use this larger sample to investigate the global physical properties of this class of sources.

The layout of the paper is as follows. In Section 4.2 we describe the method of sample selection, that we used to identify candidate radio phoenixes. This is followed by observation and data reduction methods in Section 4.3. In Section 4.4 we present the results deduced from the whole sample of radio phoenixes (new discoveries and previously known sources) and discussed the possible common properties of this sample in Section 4.5. This is followed by discussions and possible interpretations described in Section 4.6 and conclusions in Section 4.7.

Throughout the paper we assume a Λ CDM cosmology with $H_0 = 70$ $\text{kms}^{-1}\text{Mpc}^{-1}$, $\Omega_m = 0.3$, and $\Omega_\Lambda = 0.7$. All sky coordinates are epoch J2000 coordinates. This paper makes use of the cosmology calculator ([Wright 2006](#)) to compute cosmological parameters.

Table 4.1: List of all radio phoenix candidates (known to date) along with their properties.

Cluster name / Target	RA (J2000)	Dec (J2000)	Redshift (z)	Conversion (kpc/arcsec)	Reference ^a
Abell 1914	14 ^h 26 ^m 01.6 ^s	+37°49'38"	0.171	2.914	1
SDSS-C4-DR3-3088	09 ^h 46 ^m 45.4 ^s	+54°25'37"	0.046	0.904	2
Abell 2593	23 ^h 24 ^m 20.2 ^s	+14°39'04"	0.041	0.810	2
Abell 2048	15 ^h 15 ^m 17.8 ^s	+04°22'56"	0.097	1.796	2,7
Abell 1033	10 ^h 31 ^m 33.7 ^s	+35°04'34"	0.126	2.257	3
Abell 2443	22 ^h 26 ^m 02.6 ^s	+17°22'41"	0.108	1.975	4,18
Abell 133	01 ^h 02 ^m 42.1 ^s	-21°52'25"	0.057	1.105	5,17
Abell 85	00 ^h 41 ^m 50.1 ^s	-09°18'07"	0.055	1.069	5,6
24P73	22 ^h 17 ^m 36.2 ^s	+59°44'07"	0.15	2.616	7
Ophiuchus	17 ^h 12 ^m 26.0 ^s	-23°22'33"	0.028	0.562	8,9
Abell 2256	17 ^h 03 ^m 43.5 ^s	+78°43'03"	0.058	1.123	10
Abell 1931	14 ^h 31 ^m 59.7 ^s	+44°15'48"	0.17	2.898	11
MaxBCG J217.95869+13.53470	14 ^h 31 ^m 50.1 ^s	+13°32'05"	0.16	2.758	12,13
Abell 725	09 ^h 01 ^m 11.6 ^s	+62°36'14"	0.090	1.680	14
Abell 4038	23 ^h 47 ^m 43.2 ^s	-28°08'29"	0.028	0.562	15
Abell 13	00 ^h 13 ^m 38.3 ^s	-19°30'08"	0.094	1.746	5
Abell S753	14 ^h 03 ^m 35.9 ^s	-33°59'16"	0.014	0.286	16
CIZA J1926.1+4833	19 ^h 26 ^m 10.6 ^s	+48°32'44"	0.098	1.812	this work
MKW8	14 ^h 40 ^m 38.2 ^s	+03°28'35"	0.027	0.543	"
Abell 565	07 ^h 07 ^m 24.8 ^s	+71°45'22"	0.105	1.925	"
Abell 2675	23 ^h 55 ^m 33.4 ^s	+11°25'42"	0.071	1.354	"
Abell 272	01 ^h 55 ^m 19.1 ^s	+33°56'41"	0.088	1.646	"
Abell 566	07 ^h 04 ^m 24.5 ^s	+63°18'58"	0.097	1.795	"
Abell 2751	00 ^h 16 ^m 19.8 ^s	-31°21'55"	0.107	1.958	"
Abell 661	08 ^h 27 ^m 15.7 ^s	+53°08'06"	0.12	2.164	"

^a 1: Mandal et al. (2019), 2: Mandal et al. (2020), 3: de Gasperin et al. (2015), 4: Clarke et al. (2013), 5: Slee et al. (2001), 6: Durret et al. (2005), 7: van Weeren et al. (2009), 8: Werner et al. (2016), 9: Murgia et al. (2010), 10: van Weeren et al. (2012b), 11: Brüngen et al. (2018), 12: O'grean et al. (2011), 13: Shulevski et al. (2015), 14: Kempner & Sarazin (2001), 15: Kale et al. (2018), 16: Subrahmanyan et al. (2003), 17: Randall et al. (2010), 18: Cohen & Clarke (2011)

Table 4.2: Observation details of the radio phoenixes that are presented in this paper. ROSAT All-Sky Survey data have been used for the sources that do not have *Chandra* or *XMM-Newton* data.

Source ^a	LOFAR 150 MHz (120-168)MHz	GMRT 325 MHz (308-340)MHz	GMRT 610 MHz (594-626)MHz	<i>Chandra</i>	<i>XMM-Newton</i>
Abell 1914	8.33 h	3.83 h	3.18 h	✓	-
SDSS-C4-DR3-3088	8.33 h	3.68 h	3.55 h	✓	-
Abell 2593	8.33 h	3.83 h	3.18 h	✓	-
Abell 2048	8.33 h	10 h	10 h	-	✓
Abell 1033	8.33 h	4.85 h	-	✓	-
Abell 2443	8.33 h	-	-	-	✓
Abell 133	-	5.21 h	-	-	✓
Abell 85	-	4.11 h	-	-	✓
24P73	-	9.66 h	7.7 h	✓	-
Ophiuchus	-	-	6.0 h	-	✓
Abell 2256	-	-	6.6 h	✓	-
Abell 1931	-	-	-	✓	-
MaxBCG J217.95869+13.53470	-	9.16 h	-	✓	-
Abell 725	8.33 h	-	-	-	-
Abell 4038	-	5.35 h	-	-	✓
CIZA J1926.1+4833	-	3.75 h	3.23 h	-	✓
MKW8	8.33 h	7.06 h	8.33 h	-	✓
Abell 565	-	3.68 h	-	-	✓
Abell 2675	-	3.33 h	-	-	✓
Abell 272	8.33 h	6.23 h	-	-	✓
Abell 566	-	4.83 h	-	-	-
Abell 2751	-	3.71 h	3.81 h	-	-
Abell 661	-	4.18 h	3.73 h	-	-

^a Abell 13 and Abell S753 lack legacy GMRT or LOFAR data and we do not show any radio images for these two sources. Therefore, these two sources are not in this list.

Table 4.3: Mass, radio power at 325 MHz and dynamical state of the host clusters for the sample of radio phoenixes.

Cluster name / Target	Mass ^a (M_{500}) ($\times 10^{14} M_{\odot}$)	Radio Power (P_{325}) ($\times 10^{24}$ W/Hz)	Radius (R_{500}) ^b (kpc)	Dynamical state
Abell 1914 ⁽¹⁾	$7.24_{-0.26}^{+0.26}$	81.0 ± 8.0	1294 ± 15	Un-relaxed
SDSS-C4-DR3-3088 ⁽²⁾	$1.69_{-0.39}^{+0.39}$	2.34 ± 0.26	828 ± 61	Un-relaxed
Abell 2593 ⁽¹⁾	$1.82_{-0.18}^{+0.17}$	5.80 ± 0.60	1011 ± 27	Un-relaxed
Abell 2048 ⁽²⁾	$2.97_{-0.11}^{+0.18}$	14.3 ± 1.4	983 ± 12	Un-relaxed
Abell 1033 ⁽¹⁾	$3.24_{-0.30}^{+0.30}$	17.8 ± 1.9	1037 ± 32	Un-relaxed
Abell 2443 ⁽¹⁾	$3.77_{-0.27}^{+0.26}$	13.4 ± 0.70	1060 ± 25	Un-relaxed
Abell 133 ⁽¹⁾	$3.01_{-0.16}^{+0.18}$	34.3 ± 3.4	1000 ± 19	Un-relaxed
Abell 85 ⁽¹⁾	$4.91_{-0.17}^{+0.16}$	21.7 ± 2.2	1178 ± 12	Un-relaxed
24P73	—	29.0 ± 2.8	—	Un-relaxed
Ophiuchus ⁽³⁾	5.31	12.0 ± 1.2	1219	Un-relaxed
Abell 2256 ⁽¹⁾	$6.21_{-0.09}^{+0.10}$	2.81 ± 0.28	1122 ± 7	Un-relaxed
Abell 1931 ⁽⁴⁾	$1.62_{-0.72}^{+2.04}$	0.27 ± 0.58	784 ± 58	Un-relaxed
MaxBCG: J217.95869+13.53470 ⁽³⁾	1.00	4.8 ± 0.5	670	Un-relaxed
Abell 725 ⁽³⁾	3.20	7.94 ± 0.9	1010	N/A
Abell 4038 ⁽¹⁾	$1.48_{-0.10}^{+0.11}$	2.66 ± 0.27	796 ± 19	Un-relaxed
Abell 13 ⁽¹⁾	$2.75_{-0.23}^{+0.23}$	15.3 ± 1.5	981 ± 28	Un-relaxed
Abell S753 ⁽³⁾	0.26	3.80 ± 0.4	448	N/A
CIZA J1926.1+4833 ⁽¹⁾	$3.09_{-0.22}^{+0.19}$	8.77 ± 0.9	995 ± 22	Un-relaxed
MKW8 ⁽¹⁾	$1.10_{-0.20}^{+0.18}$	0.43 ± 0.04	722 ± 42	Un-relaxed
Abell 565 ⁽³⁾	1.62	3.11 ± 0.31	801	N/A
Abell 2675 ⁽¹⁾	$2.39_{-0.23}^{+0.25}$	1.32 ± 0.13	922 ± 31	Un-relaxed
Abell 272 ⁽³⁾	2.83	4.43 ± 0.40	970	Un-relaxed
Abell 566 ⁽¹⁾	$2.94_{-0.27}^{+0.24}$	40 ± 4.0	979 ± 28	N/A
Abell 2751 ⁽³⁾	1.26	56.0 ± 6.0	736	N/A
Abell 661	—	296 ± 30	—	N/A

^a The M_{500} values are taken from (1) Planck Catalogue (Planck Collaboration et al. 2016), (2) Scaling relations from Arnaud et al. (2005), (3) MCXC Catalogue (Piffaretti et al. 2011) and (4) Brüngen et al. (2018)

^b $R_{500} = \sqrt[3]{\frac{3M_{500}}{4\pi(500\rho_c)}}$, where ρ_c is the critical density of the Universe at the given redshift.

Table 4.4: Largest linear scales, distances from the cluster centre and integrated spectral indices for the sample of radio phenices. Note that, for the calculation of the largest linear scales, we have used the radio images at the lowest available frequencies. See Table 4.2 for the summary of radio and X-ray data.

Cluster name / Target	LLS (kpc)	Dist (kpc)	Spectra Index 1 ($\alpha_{150-325}$)	Spectral Index 2 ($\alpha_{325-1400}$)
Abell 1914	492	189	-2.23 ± 0.18	-2.17 ± 0.07
SDSS-C4-DR3-3088	300	349	-1.81 ± 0.19	-2.09 ± 0.10
Abell 2593	432	76	-2.16 ± 0.18	-1.10 ± 0.07
Abell 2048	360	260	-1.35 ± 0.25	-2.30 ± 0.17
Abell 1033	304	76	-1.34 ± 0.14	-1.58 ± 0.07
Abell 2443	541	50	-2.83 ± 0.26	-2.84 ± 0.16
Abell 133	425	283	-1.24 ± 0.19	-2.05 ± 0.10
Abell 85	290	438	-1.38 ± 0.17	-2.89 ± 0.09
24P73	339	117	-1.58 ± 0.13	-2.41 ± 0.18
Ophiuchus	140	200	-1.16 ± 0.09	-0.97 ± 0.04
Abell 2256	274	238	-0.66 ± 0.18	-1.94 ± 0.07
Abell 1931	520	230	-3.01 ± 0.38	-1.37 ± 1.32
MaxBCG J217.95869+13.53470	124	165	-1.09 ± 0.23	-2.80 ± 0.12
Abell 725	372	221	-0.85 ± 0.19	-0.86 ± 0.08
Abell 4038	54	20	-1.45 ± 0.20	-2.15 ± 0.08
Abell 13	260	200	-1.92 ± 0.34	-2.08 ± 0.12
Abell S753	–	–	-1.44 ± 0.0	-1.99 ± 0.0
CIZAJ1926.1+4833	496	207	-1.61 ± 0.11	-2.33 ± 0.11
MKW8	120	50	-1.84 ± 0.19	-3.23 ± 0.10
Abell 565	348	47	-1.28 ± 0.19	-2.05 ± 0.08
Abell 2675	173	71	-1.23 ± 0.20	-1.72 ± 0.08
Abell 272	291	208	-1.64 ± 0.18	-2.43 ± 0.07
Abell 566	270	63	-1.88 ± 0.21	-2.32 ± 0.09
Abell 2751	454	368	-0.77 ± 0.20	-1.34 ± 0.09
Abell 661	361	587	-0.62 ± 0.20	-1.06 ± 0.08

4.2 Sample Selection

One of the key observational properties of radio phoenixes is their ultra-steep nature. Therefore, we used the 150 MHz TGSS (resolution: $25''$) and convolved it to the resolution of 1.4 GHz NRAO VLA Sky Survey (NVSS; Condon et al. 1998: resolution $45''$) and combined the two, to look for ultra-steep spectrum sources. We selected bright (see below) sources that have a spectral index (α) ≤ -2 . The value of the spectral index in the selection of sources is somewhat arbitrary, but was necessary to limit the sample size for follow-up observations. The ultra-steep spectral index in combination with the sensitivity limit also minimise the possibility of a source being a radio halo or relic which typically have spectral indices of -1.3 to -1.1 (van Weeren et al. 2019). In addition, we also imposed the following criteria:

- A 150 MHz TGSS total flux density $S_{150} > 30$ mJy (10σ detection);
- located in the vicinity of a known cluster position (within ~ 1 Mpc) from the SDSS cluster catalogue (Wen et al. 2012) or the ROSAT All-Sky Survey (RASS: Voges et al. 1999) data;
- A morphology compatible with extended cluster emission

This sample of objects with an ultra-steep spectrum nature and extended morphology is likely the tip of the iceberg of the population. Our search also yielded ultra-steep spectrum objects that included previously known radio phoenixes and a serendipitous detection of Jupiter.¹ Our final sample consisted of 11 revived fossil plasma sources which are new discoveries and three of which were previously followed up. For this sample, we obtained deeper data at different radio frequencies with GMRT and/or LOFAR. Note that, previously known radio phoenixes were not re-observed. For three of the objects (Abell 2593, SDSS-C4-DR3-3088 and 24P73), we also obtained pointed X-ray data. In Mandal et al. (2020), we presented a detailed study of three of these revived fossil plasma sources. To extend our sample of radio phoenixes we inspected all the sources that are classified as ‘revived fossil plasma sources’ (referred as ‘F’ in the very recent review by van Weeren et al. 2019). If these sources have a filamentary morphology, appear to be resolved and have a steep spectra ($\alpha \leq -1$; with a hint of a curvature towards high-frequency), we consider them in our sample of radio

¹One of the target sources was not detected in follow-up observations. Closer inspection of the TGSS observational details revealed that this was a chance-alignment of Jupiter moving in front of a galaxy cluster.

phoenices. This yielded a list of 25 sources including the new discoveries from our search. This list of sources is provided in Table 4.1.

4.3 Observations and Methods

4.3.1 GMRT Data Reduction

We observed 6 of our targets (Abell 1914, SDSS-C4-DR3-3088, Abell 2593, CIZAJ1926.1+4833, Abell 2751, Abell 661) with the GMRT at 325 MHz and 610 MHz (project code 31_018 and 33_014). For the remaining 16 sources (Abell 2048, Abell 1033, Abell 133, Abell 85, 24P73, Ophiuchus, Abell 2256, Abell 1931, MaxBCG J217.95869+13.53470, Abell 725, Abell 4038, MKW8, Abell 565, Abell 2675, Abell 272, Abell 566), we used archival observations. Note that, Abell S753, Abell 2443 and Abell 13 lack legacy GMRT observations. See Table 4.2 for the observation details. We processed the GMRT data with the SPAM pipeline (Intema et al. 2017) that includes radio frequency interference (RFI) mitigation schemes, direction-dependent calibration, and ionospheric modelling (Intema et al. 2009). The final images of these sources are shown in Figure 4.3. The flux densities were set to the scale from Scaife & Heald (2012). A conservative 10% uncertainty was adopted for the flux density scale bootstrapping (Chandra et al. 2004) and was added quadratically to the uncertainties of all flux density measurements from the GMRT observations.

4.3.2 LOFAR Data Reduction

For 10 sources, we obtained LOFAR data at 144 MHz and they were observed in HBA_DUAL_INNER mode. 5 sources were observed as part of the LoTSS (Shimwell et al. 2017; Shimwell et al. 2019) and the other 5 targets were observed through pointed observations (project codes: LC0_037, LC6_015, LC9_027 and LC11_015). See Table 4.2 for the observation details. The standard direction-independent (DI) pipeline² (see de Gasperin et al. 2019 for the latest version) was used to correct for the DI effects, as described in detail in van Weeren et al. (2016a) and Williams et al. (2016). After the DI calibration was completed, the data were processed with the version 2.2 of the direction-dependent (DD) calibration and imaging pipeline in order to correct for DD effects. This is going to be described in detail in Tasse et al. (in prep) and is summarised briefly in Shimwell et al. (2019). This pipeline uses kMS (Tasse 2014, Smirnov & Tasse

²<https://github.com/lofar-astron/prefactor>

2015) for DD calibration and DDFacet³ (Tasse et al. 2018) for imaging with direction dependent calibration solutions applied.

A further post-processing step is conducted to subtract all the sources except for those in the vicinity of the targets and to perform additional phase and amplitude self-calibration loops for each target. This method has already been used in recent LOFAR studies (Hardcastle et al. 2019, Cassano et al. 2019, Botteon et al. 2019) and will be described in detail in van Weeren et al. (in prep.). Final images were processed by using WSCLEAN v2.8 (Offringa et al. 2014) with multi-scale multi-frequency deconvolution mode (Offringa & Smirnov 2017). The resulting images (see the legends) are shown in Figure 4.3.

Due to inaccurate beam models, the LOFAR flux scales are inaccurate and need to be corrected by comparison with other surveys (van Weeren et al. 2016b, Hardcastle et al. 2016). Here, we used catalogues from the TGSS Intema et al. (2017) to cross-match point sources near the target and compare the flux densities, similar to the approach used by Botteon et al. 2018b, Wilber et al. 2018, Mandal et al. 2019.

4.3.3 VLA Data Reduction

MKW8 has been observed with the VLA in the 1–2 GHz frequency band (project code: SH0396), with the B-, C- and D-configuration for a total time of 9 hrs (2, 5 and 2 hrs, respectively). The VLA data reduction follows the procedure as described in Di Gennaro et al. (2018). The calibration solutions were then applied to the target, and several self-calibration runs were performed to refine the amplitude and phase calibration. During these runs, automatic clean masks were employed with the PYthon Blob Detector and Source Finder (PYBDSF; Mohan & Rafferty 2015). Additional rounds of self-calibration were performed optimized for a bright source located outside of the primary beam, whose side-lobes were affecting the quality of the image. These self-calibration rounds were done by pre-subtracting all other sources in the field of view. The off-axis interfering source was then subtracted using these optimized self-calibration solutions from the uv-data. Final calibration uncertainties are of the order of 3% for the flux density scale.

4.3.4 X-ray Data Reduction

Three of the sources (Abell 2593, SDSS-C4-DR3-3088 and 24P73) were observed with *Chandra* ACIS-I in VFaint mode as part of the Guaranteed Time Ob-

³<https://github.com/mhardcastle/ddf-pipeline>

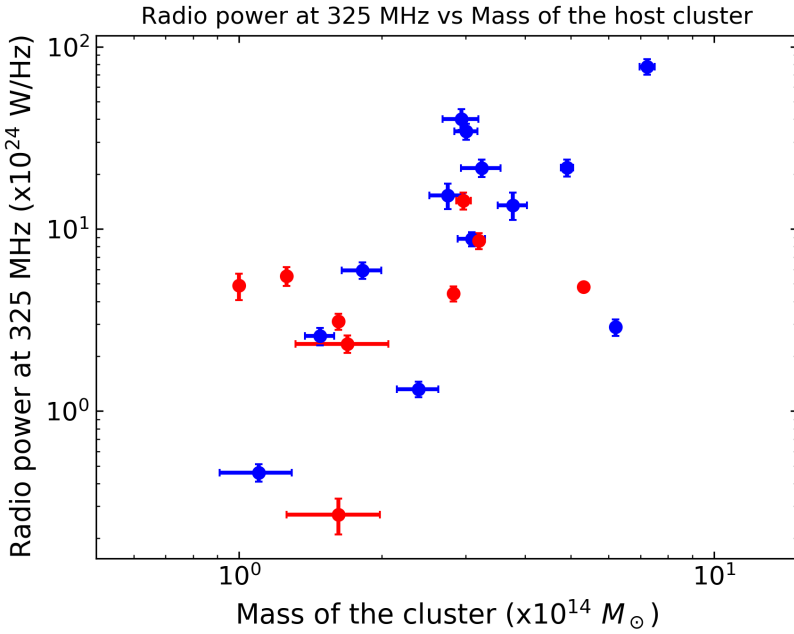


Figure 4.1: Radio power at 325 MHz for the sources in our sample as a function of the M_{500} of the host cluster. The values of M_{500} of the blue data points are from [Planck Collaboration et al. \(2016\)](#). The red data points correspond to the values of M_{500} that are taken either from [Piffaretti et al. \(2011\)](#) or derived using the scaling relations from [Arnaud et al. \(2005\)](#). See Table 4.3 for the details. The obtained Pearson and Spearman correlation coefficients from this plot are 0.48 ± 0.02 and 0.36 ± 0.08 , respectively.

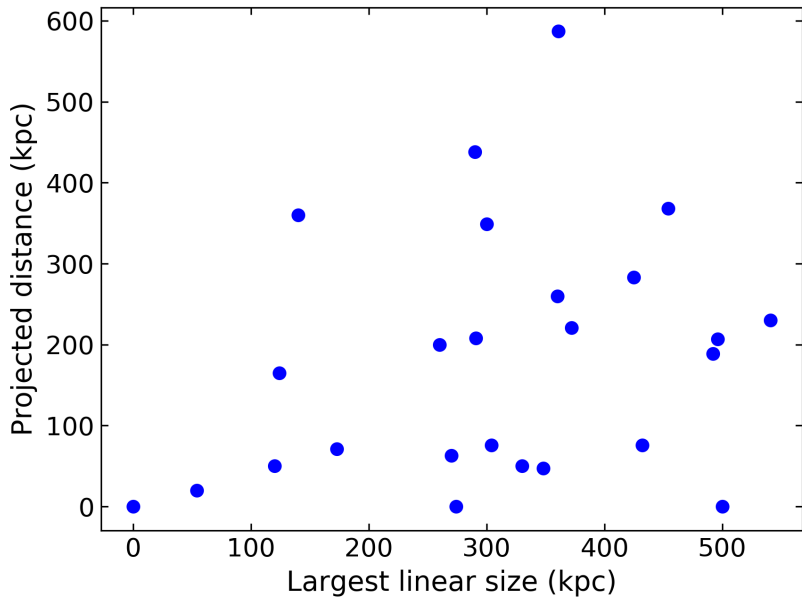


Figure 4.2: Projected distances of the radio phoenixes from the cluster centre as a function of their largest linear scales (LLS). The obtained Spearman and Pearson correlation coefficient are 0.26 ± 0.20 and 0.31 ± 0.13 respectively. See Section 4.4 for the details on how the cluster centre has been defined for this analysis.

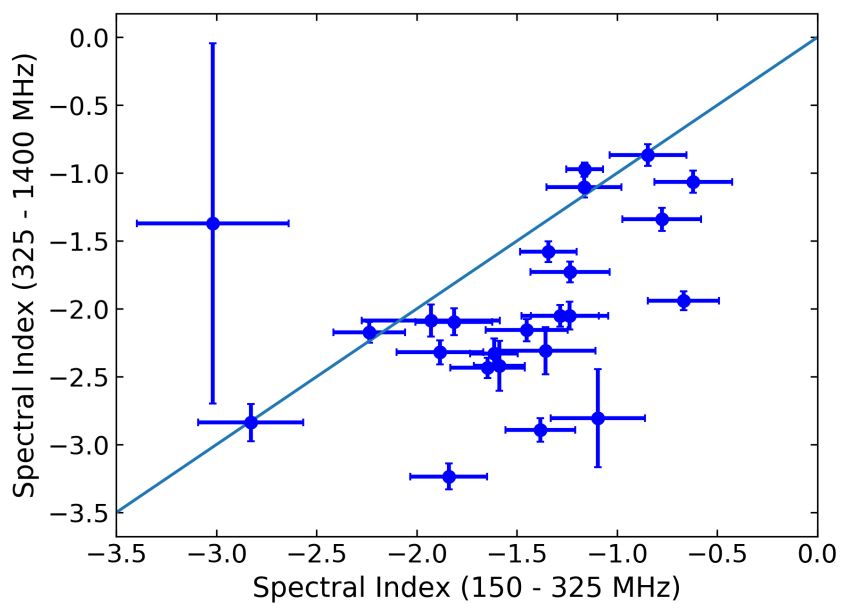


Figure 4.3: Color-color diagram for all the radio phoenixes presented in this paper. The measured flux densities (with associated error bars) and the spectral indices at different frequencies are provided in Appendix 4.5 and Table 4.4, respectively. The light blue line shows the 1:1 line.

servers (GTO) program (Obs IDs 20780, 20781 and 21710, respectively). For the rest of the sources from the sample of 25 sources, we searched in the *Chandra* and *XMM-Newton* archives for pointed observations. See Table 4.2 for the observation summary. Data were retrieved and processed with *Ciao* v4.12 (CalDB v4.9.0) and *SAS* v16.1.0 following standard reduction recipes, with the aim of obtaining exposure corrected cluster images in the 0.5 – 2.0 keV energy band. The X-ray images overlaid with contours from radio images are presented in Figure 4.3. These images were used to determine the position of the radio phoenixes in the clusters and qualitatively constrain the dynamical state of the host clusters.

4.3.5 Integrated spectral index

Due to the lack of homogeneous data available for the radio phoenixes, performing detailed spectral analysis of the sample is beyond the scope of this paper. In this paper we study the integrated spectral indices of the sources and investigate the spectral behaviour in between 150 MHz and 1.4 GHz. To sample the same spatial scales at 150 MHz and 325 MHz, we used the same inner uv -range of 200λ to image both LOFAR and GMRT data. For the sources that do not have any LOFAR 150 MHz data, we measured the total flux densities from the TGSS (Intema et al. 2017) images. Similarly, we used the NVSS (Condon et al. 1998) images to measure the total flux densities at 1.4 GHz. List of the measured flux densities at different frequencies and the source of these values are provided in Appendix 4.5.

4.4 Results

To date, 14 (candidate) radio phoenixes were known to exist in clusters. Our search yielded 11 new revived fossil plasma sources. Three out of 11 sources had been presented in detail in Mandal et al. (2019) and Mandal et al. (2020). This paper presents a sample of all radio phoenixes known to date to investigate the global physical properties of these sources and to understand the physical origin of this class. In Table 4.2 the observation details are provided. Table 4.3 shows a selection of derived / measured global properties of the host cluster. We have taken the mass of the host cluster from the Planck (Planck Collaboration et al. 2016) and MCXC (Piffaretti et al. 2011) catalogues (Note: the M_{500} values taken from the MCXC catalogues do not include any error bars). For Abell 2593, SDSS-C4-DR3-3088 and Abell 2048, we derived the mass by

using the X-ray luminosity and the scaling relations of [Arnaud et al. \(2005\)](#) (see [Mandal et al. 2020](#) for the details). Figure 4.3 shows the images of these radio phoenixes (which are marked with black ellipses) derived from the observations (as reported in Table 4.2). Note that, no radio images have been shown for Abell 13 and Abell S753, since they do not have LOFAR / GMRT data. Figure 4.3 and 4.4 shows the contour images of these sources overlaid on X-ray (*Chandra* or *XMM-Newton*) and optical (2nd Digitized Sky Survey Red) maps, respectively. The optical images are marked with black circles that show possible galaxies that could have originated the plasma associated with the diffuse radio emission (See Section 4.5 for more details). This association has been done by inspecting morphological connection with an optical counterpart and the respective redshift information.

First, we describe each of the 8 newly discovered sources and followed by briefer descriptions of sources that were previously known:

New Discoveries

- CIZAJ1926.1+4833 is a low-mass ($M_{500}=3.09^{+0.19}_{-0.22} \times 10^{14} M_{\odot}$) galaxy cluster located at $z = 0.098$ ([Planck Collaboration et al. 2016](#)). The 325 MHz GMRT image shows the presence of a bright radio source in the west of the cluster with a complex filamentary morphology. This radio source has an integrated spectral index of $\alpha_{325-1400} = -2.32 \pm 0.11$ and $\alpha_{150-325} = -1.61 \pm 0.12$, indicating that the spectra is curved towards higher frequency. To the SE (with respect to the source) we also identify a very long head tail galaxy (about 770 kpc). The tail of this galaxy is very faint at the 610 MHz (figure in Appendix 4.A). The X-ray emission (from *XMM-Newton*) is not peaked at the centre, suggesting that the dynamical state could be somewhat disturbed.
- MKW8 is a poor galaxy cluster ($M_{500}=1.10^{+0.18}_{-0.20} \times 10^{14} M_{\odot}$) located at $z = 0.027$ ([Planck Collaboration et al. 2016](#)). Previous radio observations ([Bharadwaj et al. 2014](#)) reported the presence of a central compact bright radio source NGC 5718 (one of the BCG's; marked with a black circle in Figure 4.4). Our LOFAR 150 MHz image shows previously undetected diffuse radio emission (located ~ 50 kpc towards NW side of NGC 5718) which has an extremely steep spectrum ($\alpha_{150-1400} = -2.75 \pm 0.06$) and filamentary morphology. A GMRT 610 MHz image is shown in the Appendix A where the diffuse emission is barely visible. [Tümer et al. \(2019\)](#)

did not find any presence of a cool core and classified MKW8 as a disturbed system. Using wide-band VLA observations, we investigated the polarisation properties of MKW8 (see Appendix 4.A for the VLA Stokes I image of MKW8). The total linear polarised intensity image, averaged in the 1–2 GHz band, was obtained with the `pyrmsynth tool`⁴ (see Di Genaro et al. submitted for the details). No evidence of polarised emission is detected in this source. We estimated an upper limit for the polarisation degree of 0.8%.

- Abell 565 is a low-mass cluster ($M_{500}=1.62 \times 10^{14} M_{\odot}$) located at a redshift of $z = 0.105$ (Piffaretti et al. 2011). The GMRT 325 MHz map shows that the radio emission has a complex and filamentary morphology. The radio phoenix candidate has a spectral index of $\alpha_{150-1400} = -1.79 \pm 0.05$. The BCG of the cluster (WISEA J070819.13+715224.7) is morphologically connected with the diffuse radio emission (marked with a black circle in Figure 4.4). There is no dedicated X-ray observation available for this cluster and, as a result, we classify the dynamical state of this cluster as uncertain.
- Abell 2675 ($M_{500}=2.39^{+0.25}_{-0.23} \times 10^{14} M_{\odot}$; Planck Collaboration et al. 2016) is located at a redshift of $z = 0.071$. In the *XMM-Newton* X-ray image of this cluster, we do not detect any peaked X-ray emission at the centre and classify it as an un-relaxed system. The BCG of the system (WISEA J235542.59+112035.5) is the most likely candidate associated with the diffuse radio emission. The measured integrated spectral indices of the source are $\alpha_{325-1400} = -1.72 \pm 0.08$ and $\alpha_{150-325} = -1.23 \pm 0.20$.
- Abell 272 ($z = 0.088$) is a low-mass galaxy cluster ($M_{500}=2.83 \times 10^{14} M_{\odot}$; Piffaretti et al. 2011). The two bright X-ray peaks are associated with two cluster members: ZwCl 0152.0+3337 06 & ZwCl 0152.0+3337 08 which are marked as X1 and X2, respectively, in Figure 4.4. The LOFAR 150 MHz radio image shows an elongated morphology in the north-south direction. The elongated feature is also visible in the GMRT 325 MHz image (shown in Appendix 4.A). However, some of the diffuse emission that is visible at 150 MHz, is not well recovered at 325 MHz, suggesting that its spectrum is steep. The measured integrated spectral indices are $\alpha_{325-1400}$

⁴<https://github.com/mrbell/pyrmsynth>

$= -2.43 \pm 0.07$ and $\alpha_{150-325} = -1.64 \pm 0.18$. We locate three galaxies that are morphologically connected with the radio emission and are cluster members: A (ZwCl0152.0+3337 03), B (ZwCl0152.0+3337 04) and C (ZwCl0152.0+3337 05). The X-ray emission (see Figure 4.3) does not appear to be peaked, hence we classify it as an un-relaxed system.

- Abell 566 ($z = 0.097$) was known (Harris et al. 1982) to host a very steep-spectrum object: 4C63.10 ($\alpha_{38-408} \sim -1.7$). In the GMRT 325 MHz image presented in this paper, we find two BCGs of this cluster (marked as ‘A’: ZwCl 0658.3+6320 e and ‘B’: ZwCl 0658.3+6320 a in the optical image). The location of the brightest radio emission coincides with the position of the host galaxy ‘A’. The measured integrated spectral indices of this source are $\alpha_{325-1400} = -2.32 \pm 0.09$ and $\alpha_{150-325} = -1.88 \pm 0.21$, indicating that the spectra is curved towards higher frequency. We do not have pointed *Chandra* or *XMM-Newton* observations of this source. In the Appendix 4.A, we showed a Suzaku X-ray image of this cluster. Even though the cluster has regular morphology, it is not peaked at the centre suggesting the dynamical state could be un-relaxed. This needs to be confirmed with dedicated *Chandra* or *XMM-Newton* observations in future.
- Abell 2751 ($z = 0.107$) is a very low-mass galaxy cluster ($M_{500} = 1.26 \times 10^{14} M_{\odot}$; Piffaretti et al. 2011) that has peculiar radio emission. Towards the west, we identify an elongated region extending towards the south. The brightest part of the radio emission has an optical counterpart with a galaxy (marked as ‘A’: PKS 0013-316 in the optical image). The measured integrated spectral indices of the diffuse, filamentary region towards the east side of the cluster are $\alpha_{325-1400} = -1.34 \pm 0.09$ and $\alpha_{150-325} = -0.77 \pm 0.20$. At this location, we identify an optical galaxy WISEA J001657.00-312134.9 (marked as ‘B’ in the optical image) that could be associated with the diffuse radio emission. Note that the source appears to have regions with a very steep spectral indices of ≤ -2 (de Gasperin et al. 2018).
- Abell 661 is located at a redshift of $z = 0.12$. The radio emission has three distinctive features and only part of the diffuse emission at the north is identified to have steep spectrum. From the north to the

south, we have identified three optical galaxies which are marked as ‘A’ (WISEA082708.33+531108.0), ‘B’ (WISEJ082720.91+530748.2) and ‘C’ (WISEJ082729.73+530733.5) in the optical image. The eastern part of the emission in the north has a very steep spectra (see Appendix for the GMRT 610 MHz map) and filamentary morphology. X-ray observations are needed in order to investigate the dynamical state of this cluster.

Previously known sources

- Abell 1914 is a well studied massive ($M_{500}=7.24_{-0.26}^{+0.26} \times 10^{14} M_{\odot}$; [Planck Collaboration et al. 2016](#)) galaxy cluster located at a redshift of $z = 0.17$. Recent LOFAR and GMRT observations ([Mandal et al. 2019](#)) showed the ultra-steep spectrum source (4C38.39), previously thought to be part of a radio halo ([Bacchi et al. 2003](#), [Govoni et al. 2004](#)), is a distinct source with properties that are consistent with radio phoenixes. *Chandra* observations ([Botteon et al. 2018a](#)) showed that Abell 1914 has a very disturbed morphology with possible shocks present. However, the shock is not located at the radio phoenix.
- In [Mandal et al. \(2020\)](#), we studied SDSS-C4-DR3-3088 ($z = 0.046$; [Simard et al. 2009](#)) and Abell 2593 ($z = 0.041$; [Ulmer et al. 1981](#)) in detail with radio (LOFAR and GMRT) and X-ray (*Chandra*) observations and classified them as radio phoenixes. SDSS-C4-DR3-3088 contains what looks to be a wide-angle radio tail. Abell 2593 has a morphology more similar to a narrow-angle radio tail. Both of them show filamentary structure with patchy spectral index along the source. The dynamical states of these clusters are not relaxed.
- [van Weeren et al. \(2009\)](#) followed up Abell 2048 ($z = 0.098$; [Struble & Rood 1999](#)) with GMRT and VLA observations and classified it as a relic radio source. In [Mandal et al. \(2020\)](#) we studied this cluster with additional LOFAR data and recovered more extended diffuse emission compared to previous studies. The dynamical state of this cluster was classified as un-relaxed with *XMM-Newton* observations.
- Abell 1033 ($z = 0.126$) is a moderately massive galaxy cluster that underwent a recent merger and [de Gasperin et al. \(2015\)](#) presented the detection

of a radio phoenix close to the moment of its formation. Later, with the help of GMRT and LOFAR observations, [de Gasperin et al. \(2017\)](#) detected another ultra-steep spectrum source that is related with the cluster merger and classified as a gently re-energized tail (GR_eET).

- The radio phoenix in Abell 2443 ($z = 0.108$) was first shown in [Cohen & Clarke \(2011\)](#). Later, with deep *Chandra* observations, [Clarke et al. \(2013\)](#) demonstrated that the cluster is highly disturbed. A tentative shock at the location of the radio phoenix was also reported.
- [Slee et al. \(2001\)](#) presented results from 1.4 GHz observations of four sources in the clusters: Abell 133 ($z = 0.057$), Abell 85 ($z = 0.055$), Abell 13 ($z = 0.094$) and Abell 4038 ($z = 0.028$). Even though Abell 133 has been identified as a cool-core cluster ([Cavagnolo et al. 2009](#)), *Chandra* observations showed presence of dynamical disturbance ([Randall et al. 2010](#)). The X-ray emission in Abell 85 is peaked at the centre, however, *XMM-Newton* observations have shown the presence of dynamical activity revealing that it is not fully relaxed ([Durret et al. 2005](#)). Abell 13 has been classified as a system that has undergone a recent merger ([Juett et al. 2008](#)). [Kale et al. \(2018\)](#) showed an absence of a cool core in Abell 4038 and classified it as an un-relaxed system. In this work, we have shown GMRT 325 MHz images for Abell 133 and Abell 85. These 325 MHz images reveal much more extended emission compared to the ones presented by [Slee et al. \(2001\)](#) at 1.4 GHz. Note that we do not show any image for Abell 13 in this paper. The 325 MHz flux measurements are taken from [Joshi et al. \(1986\)](#).
- The radio source 24P73 was found to have an unusually steep spectrum ([Green & Joncas 1994](#)) and [van Weeren et al. \(2011\)](#) classified it as a radio phoenix. The galaxy cluster associated with this source is currently not confirmed due to high extinction from the Galactic plane. However, using Hubble-R relation, [van Weeren et al. \(2011\)](#) estimated a redshift of this source to be $z = 0.15 \pm 0.1$. Recently this source has been observed with *Chandra* and the resulting image is shown in Figure 4.3. We do not detect any peaked X-ray emission at the centre of the cluster and classify as un-relaxed system.

- [Kempner & Sarazin \(2001\)](#) detected diffuse radio emission in Abell 725 ($z = 0.09$) from the WENSS. In this paper we have shown the 325 MHz GMRT image of the source. The brightest radio source is associated with the elliptical galaxy (marked in the optical image). The diffuse radio emission located towards the north-eastern side of this elliptical galaxy (marked with a circle in the radio image), has an ultra-steep spectrum. The X-ray gas is thought to be slightly elongated along the axis connecting the ultra-steep spectrum source and the cluster centre ([Kempner & Sarazin 2001](#)).
- The Ophiuchus cluster is located at a redshift of $z = 0.028$ and is the second brightest galaxy cluster in the X-ray sky. With deep *Chandra* observations, [Werner et al. \(2016\)](#) showed that the core of the cluster is dynamically disturbed with multiple sloshing induced cold fronts. Their deep 1.4 GHz map reveals the presence of a very filamentary source towards the NE of the cluster centre, that was classified as a radio phoenix. Similar features were also reported in [Murgia et al. \(2010\)](#).
- Abell 2256 ($z = 0.058$) is a well-studied massive galaxy cluster that is presently undergoing a merger with a smaller sub-cluster. Even though the main focus of studies of this cluster in the past has been the radio relic, halo and the long head-tail galaxy, this system is known to host ultra-steep spectrum sources. ‘Source F’ is one of the objects that was discovered by [Bridle et al. \(1979\)](#) and classified as a radio phoenix by [van Weeren et al. \(2012a\)](#). This source is located towards the east of the main relic. In this paper, we have shown the 325 MHz image of this source.
- Abell 1931 ($z = 0.17$) is a low-mass ($M_{500}=1.62_{-0.72}^{+2.04} \times 10^{14} M_{\odot}$) galaxy cluster. The *Chandra* image of this cluster is not peaked at the centre (see Figure 4.3) and hence is classified as un-relaxed. With the use of LOFAR 150 MHz data, [Brüggen et al. \(2018\)](#) showed the presence of diffuse ultra-steep emission in this cluster that has not been detected in 325 MHz and 610 MHz. A bright, red elliptical galaxy (SDSS J143212.84+441620.4) was claimed to be the BCG and a possible host for the diffuse emission.
- MaxBCG J217.95869+13.53470 ($z = 0.16$) is a low-mass ($M_{500}=1.00 \times 10^{14} M_{\odot}$) galaxy cluster that is undergoing a merger event. With GMRT

325 MHz & 610 MHz observations [Ogrea et al. \(2011\)](#) showed the presence of a radio phoenix towards the SW of the cluster that is not associated with X-ray or optical emission. However, a bridge of faint radio emission is connected with the central radio source (AGN). [Shulevski et al. \(2015\)](#) presented a low-frequency spectral index map between 150 and 325 MHz of this source, that does not show signs of patchiness in the spectral indices. However, the source is only a few beam-widths across and beam smearing can play a roll.

- Abell S753 ($z = 0.014$) is known to have an ultra-steep spectrum radio source: PKS B1400–33 ([Sarazin 2013](#)). [Subrahmanyan et al. \(2003\)](#) presented the VLA 330 MHz and ATCA 2.4 GHz observations and identified the bright X-ray emission in this cluster to be associated with NGC 5419. The radio source has an integrated spectral index of < -1.4 between 85 MHz and 330 MHz and tends to get steeper (~ -2) at higher (2.4 GHz) frequency, suggesting a possible curved spectrum. Note that we do not show any image for Abell S753 and refer to [Subrahmanyan et al. \(2003\)](#).

4.5 Common properties

In this section, based on the results presented in Section 4.4, we list physical properties of the radio phoenixes.

Connection with an AGN?

A key question that needs to be answered is what is the source of these fossil electrons in the ICM? It is clear that galaxy clusters host a number of radio galaxies that have an active galactic nuclei (AGN). In the results section, we showed the presence of nearby optical galaxies / AGNs that belong to the host cluster and have a tentative morphological connection with the diffuse radio emission. The possible optical counterparts of these AGNs are marked in Figure 4.4. Note that, a morphological connection with an optical counterpart is not obvious for the sources: Abell 2443, 24P73, Ophiuchus, MKW8 and MaxBCG J217.95869+13.53470. Indeed, the plasma from an AGN can move in the ICM with respect to its source of origin, making the identification of optical hosts harder ([Duchesne & Johnston-Hollitt 2019](#), [Randriamanakoto et al.](#)

2020). At the location of the (possible) optical counterparts, the spectral index value (Abell 1914, SDSS-C4-DR3-3088, Abell 2593, Abell 2048, Abell 1033, Abell 2443, Abell 133, Abell 2256, Abell 4038; see Table 4.1 for references) is flatter (~ -0.8) which is in agreement with the expectation from the lobes of an active AGN.

Radio power of the source and mass of the host cluster

Studying the correlation of thermal and non-thermal components in clusters can be useful to understand the dynamics in the ICM. Since deep radio data at 325 MHz is available for a large fraction of the whole sample of radio phoenixes, we calculated the k -corrected 325 MHz radio power $P_{325\text{MHz}} = 4\pi S_{325\text{MHz}} D_L^2 (1+z)^{-(\alpha+1)}$ (the values of the measured flux densities and radio powers with associated errors are reported in the Appendix 4.5). The spectral indices of these sources vary over the frequency range from 150 MHz to 1.4 GHz (See Table 4.4). Therefore, we used a conservative value of the spectral indices from -2 to -1.5 to calculate the k -corrected radio power. It is important to note that, using this range of spectral indices, does not change the value of the derived radio power significantly, given the fact that these sources reside in nearby Universe. Using the mass reported in Table 4.3, we have investigated if there is a trend between the derived radio power at 325 MHz as a function of the mass (M_{500}) of the host cluster (see Figure 4.1). The values of the Pearson (0.48 ± 0.02) and Spearman (0.36 ± 0.08) and correlation coefficients do not suggest a strong correlation between these two measured quantities.

Position and Size of the sources

Previous studies of radio relics found that they are usually located in the outskirts of clusters and that there is a correlation between the largest linear size (LLS) and the distance from the cluster centre (de Gasperin et al. 2014). We therefore compare the LLS of the radio phoenixes with the projected distance from the cluster centre. Since the morphologies of these radio phoenixes are very filamentary and irregular compared to radio halos and radio relics, robustly estimating the ‘position of the source’ from a reference point is not trivial. Therefore, by analogy with centre of mass, we define a parameter ‘centre of intensity’ which can be described as a unique point where the weighted relative position of the distributed flux densities sums to zero. The regions of the emission that go into these calculations are also marked in the radio images. We take the contribution of the whole emission from the ‘phoenix’ source into account. If

the flux density at a location (x,y) is $I(x,y)$, the co-ordinates of the centre of intensity (X and Y) are:

$$X = \frac{\sum I(x,y) \times x}{\sum I(x,y)} \quad (4.1)$$

$$Y = \frac{\sum I(x,y) \times y}{\sum I(x,y)} \quad (4.2)$$

Having found this position, the distance from the cluster centre is then calculated as the distance from the location of the pixel with the brightest emission in X-ray, from (X,Y) . The plot of projected distance vs LLS is shown in Figure 4.2. We do not find any strong correlation between these two measured parameters. The measured Spearman and Pearson correlation coefficients are 0.26 ± 0.20 and 0.31 ± 0.13 , respectively. Note that we have used the RASS data for the sources that do not have any *Chandra* or *XMM-Newton* observations. We have also reported the values of R_{500} in Table 4.3. We note that the radio phoenixes are all located well within R_{500} of their host clusters.

Dynamical state of the host cluster

In Figure 4.3, we show the X-ray images overplotted with the contours from the radio emission (in white). Images of only 18 sources are shown that have dedicated X-ray observations (See Table 4.2 for the summary of the observation details and Section 4.3 for the method of data reduction). Visual inspection of X-ray images is one of the qualitative ways that can be used to identify dynamical state of a cluster (Lovisari et al. 2017). Based on our visual inspection of the X-ray emission and on the literature studies, we have summarised the dynamical state of these systems of galaxy clusters in Table 4.3. For a more quantitative analysis, it is important to study morphological parameters (such as centroid shift, concentration parameters, power ratios etc.) of a cluster. However, homogeneous deep X-ray data would be highly advantageous for this purpose.

We see that all the 19 sources out of 25 sources that have pointed observation reside in somewhat dynamically un-relaxed clusters. Systematic deep X-ray observations will follow in future to characterise the dynamical state of the clusters more accurately and map the temperature in different regions.

Spectral properties

While sources in our sample have ultra-steep spectrum by selection, also all the previously known radio phoenixes show an overall ultra-steep radio spectrum. Previous literature studies found that the spectral index measurements from different observations tend to show a hint of a curved spectrum towards high (\sim GHz) frequencies (Slee et al. 2001, Cohen & Clarke 2011, de Gasperin et al. 2017, Kale et al. 2018, Mandal et al. 2019, Mandal et al. 2020). For the newly discovered sources, a hint of spectral steepening is also noticed while comparing the spectral index measurements from 150 MHz (TGSS or LOFAR) to 325 MHz and 325 MHz to 1.4 GHz (NVSS) measurements. The measured total flux densities are listed in Appendix 4.5. See Table 4.4 for the values of spectral indices as measured from these flux density measurements. In order to investigate the overall spectral shape, we used so called three frequency ‘color-color’ plots which is shown in Figure 4.3. Here, we have plotted the high-frequency spectral indices ($\alpha_{325-1400}$) vs the low-frequency spectral indices ($\alpha_{150-325}$). The light blue line shows 1:1 line. The fact that most of the sources lie below the identity line, shows that these sources have a curved spectrum towards high frequencies. However, it is important to note here that deeper high resolution, i.e. VLA 1.4 GHz observations are important to confirm this claim.

4.6 Discussion

In the last decades, the taxonomy of (diffuse) radio sources has become clearer. However, in many cases for example, the distinction between ‘radio relics’ and ‘radio phoenixes’ was not evident. For instance, some of the present day radio relics (Abell 2256, Abell 3667 etc.) were previously thought to be in the category of radio phoenixes. Statistical follow-up observations of radio relics have made the contrast with radio phoenixes clearer. However, radio phoenixes are still a poorly studied class of the population of diffuse cluster radio sources. Here we discuss insights obtained from the observations and results presented in the previous sections.

Source of relativistic particles: AGN origin

From the optical maps presented in Figure 4.4, we observe that (most of) these sources are morphologically connected with an AGN (radio galaxy) which implies that lobes and tails of radio galaxies in clusters are likely candidates for the

source of relativistic particles that power radio phoenixes. The typical length scales of these phoenixes are $\leq 500\text{--}600$ kpc (see Table 4.4 for the LLS of the phoenixes). A definite identification of the host galaxy for these sources is not trivial. However, we find that in general, nearby elliptical galaxies are more likely candidates to be associated with these phoenixes. Although, the BCGs could also be a possible candidate for the source of seed particles (for ex: Abell 133, Abell 725, MKW8 etc.).

Location of the phoenixes in the cluster

An interesting result is that all the radio phoenixes are located well within the R_{500} (at least in projection) of the cluster (See Table 4.3 and 4.4 for the R_{500} and the distance from the cluster centre, respectively).

In the inner regions of clusters, the pressure of the ICM is higher compared to the outskirts. These high pressure environments do not allow the free expansion of the fossil radio plasma and the plasma remains more confined (Parma et al. 2007, Murgia et al. 2011). Thus, low-frequency radio emission from these fading plasma can last longer if their expansion is reduced by the high pressure environment. In addition, if the expansion of the lobes is prevented, the synchrotron losses are expected to be much higher due to the higher internal magnetic fields (Bonafede et al. 2011) of pressure confined radio plasma. As a result, the radio source could exhibit ultra-steep spectrum. On the contrary, if radio plasma lives in the cluster outskirts, the ambient environment is not dense enough to prevent the expansion of the lobes into the ICM. Due to the expansion, the strength of the internal magnetic field also decreases, and so as the radiative losses. Therefore, the radio emission can become too faint to be detected, even at the lower-frequencies. For these reasons, steep-spectrum radio phoenixes are more likely to be found in dense environments. This is also one of the key differences when compared to radio relics which tend to reside in cluster outskirts (Feretti et al. 2012, van Weeren et al. 2019).

Spectral behaviour and acceleration mechanism

In Table 4.4, we reported the values of the integrated spectral indices of the radio phoenixes. Figure 4.3 shows the variation of high-frequency spectral indices ($\alpha_{325-1400}$) with respect to the low-frequency spectral indices ($\alpha_{150-325}$). Most of the sources lie below the 1:1 line in this three frequency color-color diagram indicating that the spectral indices are flatter at the lower (between 150 – 325 MHz) frequencies and steeper at higher (between 325 – 1400 MHz) frequencies;

i.e. in general the radio phoenixes show spectral steepening at higher frequencies similar to the lobes of remnant radio galaxies that also have a curved spectra (Murgia et al. 2011, Brienza et al. 2016) due to IC and radiative losses.

It has been shown that in the absence of dynamical processes, low-energy relativistic electrons from lobes of radio galaxies can be poorly mixed with the thermal ICM (Sarazin 1999; Petrosian 2001; Pinzke et al. 2013). Therefore, temperature inside the radio plasma (that is mixed with the thermal plasma) increases and also the sound speed is high. Under these conditions, a weak shock in the ICM will not transfer as a shock in the lobe. Instead of shock re-acceleration, it can compress these old lobes of radio galaxies adiabatically (Ensslin et al. 1998, Enßlin & Brüggen 2002). Compression only shifts the spectral shape of the spectrum towards higher frequencies and does not change the underlying shape of the electron population.

It is important to note here, that all the previously known radio phoenixes tend to show a patchy distribution of spectral indices (see the respective references on Table 4.3 for the spectral index maps). They do not have a clear gradient in their spectral indices across the source⁵. This might be a key difference with merely aged tails from (remnant) radio galaxies that show instead a spectral gradient across the lobes (Murgia et al. 2011, Shulevski et al. 2017). On the other hand, as a contrast, radio relics also show spectral gradient and their spectrum follow a power-law distribution (van Weeren et al. 2019, Rajpurohit et al. 2020).

Therefore, for the phoenixes, this suggests a possible mix of cosmic-ray particles that have different ages and losses. This in-homogeneous mixing of the ICM and the relativistic particles from an AGN also implies an averaging of the effective adiabatic index ($\frac{4}{3} < \gamma_{ad} < \frac{5}{3}$) that could lead to different adiabatic compression ratios and re-acceleration efficiencies across the source. Hence, even if we find that radio phoenixes tend to follow a curved spectra, these sources should not be thought of a reservoir of uniform cosmic-ray population.

Dynamical state of the host cluster

We find that 19 out of 25 sources in our sample (the rest of the sources do not have pointed X-ray observations and hence, no information is available) are residing in clusters that are dynamically un-relaxed (See Table 4.3 for a

⁵Although, some of the newly discovered sources lack multi-frequency radio data to create resolved spectral index maps that are essential to investigate spatial variation of spectral indices.

summary and Section 4.4 for the method of qualitative determination of the dynamical states).

Dynamically un-relaxed clusters have (weak) shocks and ICM bulk motions which can affect ghost plasma from radio galaxies (Jones et al. 2017a). In line with our observations, recent simulations (Nolting et al. 2019 and O’Neill et al. 2019) have shown that old radio lobes in presence of (weak) shocks and/or relative motion with respect to the ICM can show filamentary morphologies and curved spectra. However, it is important to note that, to date, there has not been a clear detection of a shock at the location of a radio phoenix. The lack of a detection of a shock could potentially be related to our finding that these phoenixes are mostly located within the R_{500} of a cluster. The Mach number of a merger shock and its surface area increase with the distance from the cluster centre (Vazza et al. 2012). Which essentially means, the central regions of the ICM are crossed by weak shocks and they are much harder to be detected (Botteon et al. 2018a).

Scaling relations

Studying the correlation between thermal and non-thermal components helps to understand the dynamics in the ICM. For radio halos and relics it has been found that the measured radio power and the mass (M_{500}) of the host cluster are correlated (radio halos: Cassano et al. 2010, Cassano et al. 2013; radio relics: de Gasperin et al. 2014, Brüggén & Vazza 2020). For radio phoenixes, we do not notice any strong correlation between these two quantities (reported in Figure 4.1). Also, we see that only four (Abell 1914, Ophiuchus, Abell 2256 and Abell 85) out of 25 sources, are located in (moderately) massive clusters; the rest are mostly residing in lower-mass systems. The fact that these systems seem to be located mostly in lower-mass systems could be because low-mass clusters are more abundant than massive clusters. Indeed, clusters with mass $> 4 \times 10^{14} M_{\odot}$ are rare in the local Universe (Planck Collaboration et al. 2016) and our sample is mainly driven by the TGSS, which is sensitive only to the luminous sources that are nearby.

In addition, we also do not find any correlation between the distance from the cluster centre with the largest linear scales of the radio phoenixes (see Figure 4.2). This is also in contrast with the scaling relations found by Bonafede et al. (2012) and de Gasperin et al. (2014) for radio relics. The fact that there is a lack of correlation between these measured quantities suggests that the formation of these sources do not directly depend on the energy released due to the merger. Rather, their formation may be more closely related to the state of AGN activity

for respective cases.

It is important to note here that recently it has also been found that smaller radio relics can occur at the periphery of clusters (Nuza et al. 2017) and analysing the ‘shape’ of radio sources as a function of the distance from the cluster centre could be a better proxy in order to distinguish radio relics and radio phoenixes. This will also enable us to understand the dynamics of the cluster and its relation with the non-thermal emission. Upcoming sensitive radio (such as LoTSS; Shimwell et al. 2019) and X-ray (eRosita) surveys will be crucial to address this question in an unbiased way.

Future study: polarization properties of radio phoenixes

In future, it will be important to observe these radio phoenixes at \sim GHz frequencies to determine the sources’ polarization fraction and the polarization angle. Simulations indicate that if these sources are indeed shock compressed, there should be a correlation between the total linear polarization and the viewing angle because of the magnetic field ordering (Enßlin & Brüggen 2002). In our sample, we could investigate the polarisation properties only for MKW8, being able to put an upper limit for the polarisation degree (i.e. 0.8%). It could be the case that the source is not intrinsically polarised. However, since the source is located near the cluster centre (\sim 50 kpc), it is likely that the source can suffer extreme depolarisation due to the ICM (Rotation Measure: $RM \propto \int n_e \times B_{\parallel} dl$, where n_e and $B_{\parallel} dl$ the electron density and the perpendicular component of the magnetic field integrated along the distance to the source L). We also do not detect polarized signal from the BCG of this cluster. Future wide S-band observations with the VLA would be crucial to determine if strong depolarization can occur from the ICM.

Drawing general conclusions on the polarisation properties for the whole population is beyond the scope of this paper. But we also notice that these phoenixes are located mostly towards the centre of the cluster (see the R_{500} values in Table 4.3). This suggests that the sources could be highly de-polarized. Also, if these sources are indeed associated with weak shocks, the expected alignment and amplification of the magnetic field are also less. Finally, given the fact that these phoenixes have a very steep spectra, they could be very faint at GHz frequencies. Therefore, statistical follow-up observations to study the polarisation may not be trivial.

4.7 Summary and conclusion

In this paper, we have presented an exploratory study in which we look for ultra-steep spectrum sources using the 150 MHz TGSS and the 1.4 GHz NVSS. Our search yielded 11 new discoveries that were followed up with radio and/or X-ray observations. Based on the results from these observations, we classify them in the category of radio phoenixes. In addition, to extend our sample of radio phoenixes and to be as complete as possible we inspected all the sources that are classified as ‘revived fossil plasma sources’ (referred as ‘F’ in the latest review by [van Weeren et al. 2019](#)). Sources that are resolved, have a filamentary morphology, have a steep spectrum ($\alpha \leq -1$) with a hint of a curvature towards high-frequency, were considered to be candidate phoenixes. We present the results from all the known or newly discovered radio phoenixes along with their common physical properties in order to establish the nature of this relatively unexplored class of objects. Below we summarize our findings:

- These radio phoenixes appear to have an AGN origin and are located well within the R_{500} of the cluster. This is one of the key differences when compared to radio relics that reside towards the outskirts of the cluster. The high-pressure environments inside the cluster region do not allow the free expansion of the fossil radio plasma (from an AGN), making it more confined. Also, synchrotron losses are greater inside the cluster, which could explain the unusually steep spectra of these sources.
- These sources show a spectral steepening towards high frequencies, suggesting the integrated spectra is curved. Also, they have spatially non-uniform spectral indices. So even if the phoenixes tend to follow a curved spectra, these sources should not be thought of a reservoir of uniform cosmic-ray population. Resolved spectral index maps are also crucial tools to distinguish between different class of diffuse radio sources and to probe the energy distribution of relativistic particles within a (radio) source.
- From the X-ray observations, we notice that 19 of the sources (6 out of 25 sources do not have pointed X-ray observations) tend to live in clusters that are dynamically un-relaxed, therefore supporting the scenario that these are associated with ICM motion and/or shocks.
- We find that 19 out of 23 sources (2 of the clusters do not have any measurements on their masses) are located in low-mass ($< 4 \times 10^{14} M_{\odot}$) clusters of galaxies. Also, for these sources, we compared: a) the 325 MHz

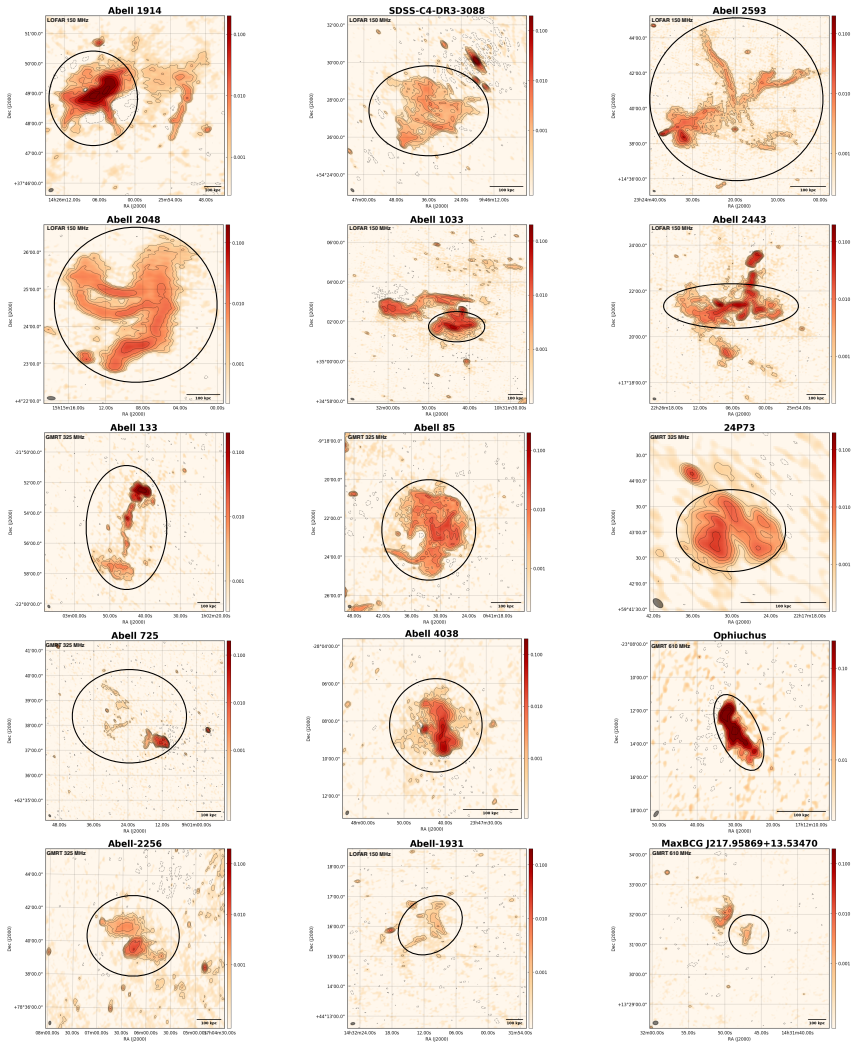
measured radio power as a function of the cluster mass, and b) the largest linear scale of the sources as a function of projected distance from the cluster centre. We do not notice any strong correlations between these measured quantities.

Our method to look for these ultra-steep spectrum sources in galaxy clusters was driven by the TGSS at 150 MHz and only the brightest sources were followed up which is necessarily the tip of the iceberg of this population. Future much deeper and sensitive low-radio-frequency surveys such as LoTSS at 144 MHz ([Shimwell et al. 2019](#)) & LoLSS at 53 MHz (de Gasperin et al. in prep) will be excellent tools to further investigate the nature of these fossil electron populations. Since these forthcoming surveys are an order of magnitude deeper in terms of both resolution and depth, they will most likely also be able to pick sources that are at higher redshift. Thus, it will be possible to compile a more unbiased and complete sample of radio phoenixes and investigate their occurrence rate in clusters.

Acknowledgments

This paper is based (in part) on data obtained with the International LOFAR Telescope (ILT) under project code LC0_037. LOFAR ([van Haarlem et al. 2013](#)) is the Low Frequency Array designed and constructed by ASTRON. It has observing, data processing, and data storage facilities in several countries, that are owned by various parties (each with their own funding sources), and that are collectively operated by the ILT foundation under a joint scientific policy. The ILT resources have benefitted from the following recent major funding sources: CNRS-INSU, Observatoire de Paris and Université d'Orléans, France; BMBF, MIWF-NRW, MPG, Germany; Science Foundation Ireland (SFI), Department of Business, Enterprise and Innovation (DBEI), Ireland; NWO, The Netherlands; The Science and Technology Facilities Council, UK ; Istituto Nazionale di Astrofisica (INAF), Italy. We thank the staff of the GMRT that made these observations possible. GMRT is run by the National Centre for Radio Astrophysics of the Tata Institute of Fundamental Research. This paper is based on the data obtained with the International LOFAR Telescope (ILT). The Leiden LOFAR team acknowledge support from the ERC Advanced Investigator programme NewClusters 321271 and the VIDI research programme with project number 639.042.729, which is financed by the Netherlands Organisation for Scientific Research (NWO). AD acknowledges support by the BMBF

Verbundforschung under the grant 05A17STA. The Jülich LOFAR Long Term Archive and the German LOFAR network are both coordinated and operated by the Jülich Supercomputing Centre (JSC), and computing resources on the supercomputer JUWELS at JSC were provided by the Gauss Centre for supercomputing e.V. (grant CHTB00) through the John von Neumann Institute for Computing (NIC). AB and RJvW acknowledges support from the VIDI research programme with project number 639.042.729, which is financed by the Netherlands Organisation for Scientific Research (NWO). MB acknowledges support from the ERC-Stg DRANOEL, no 714245. GDG acknowledges the support from the ERC Starting Grant ClusterWeb 804208. WLW acknowledges support from the CAS-NWO programme for radio astronomy with project number 629.001.024, which is financed by the Netherlands Organisation for Scientific Research (NWO). The scientific results reported in this article are based in part on observations made by the Chandra X-ray Observatory and in part by XMM-Newton, an ESA science mission with instruments and contributions directly funded by ESA Member States and NASA. This research made use of APLpy, an open-source plotting package for Python hosted at <http://aplpy.github.com>.



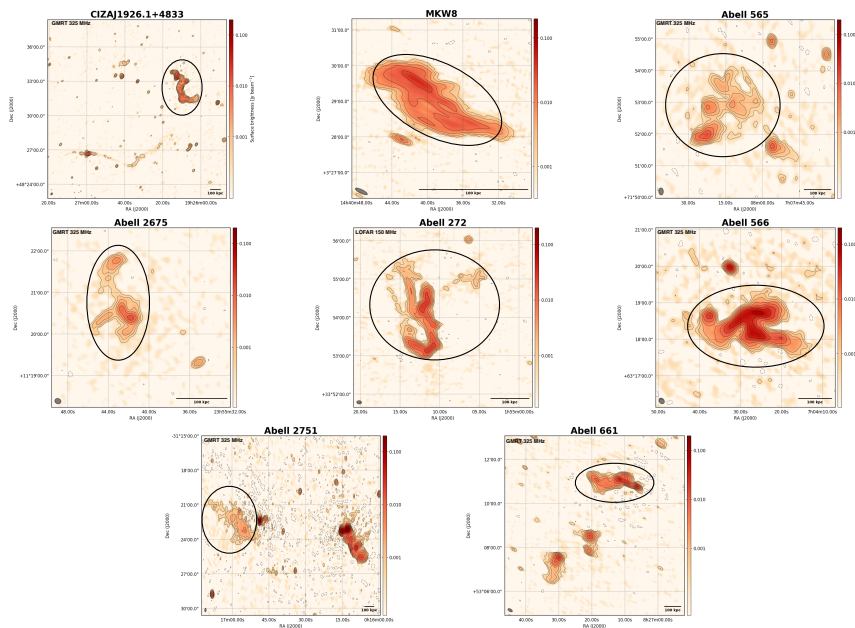
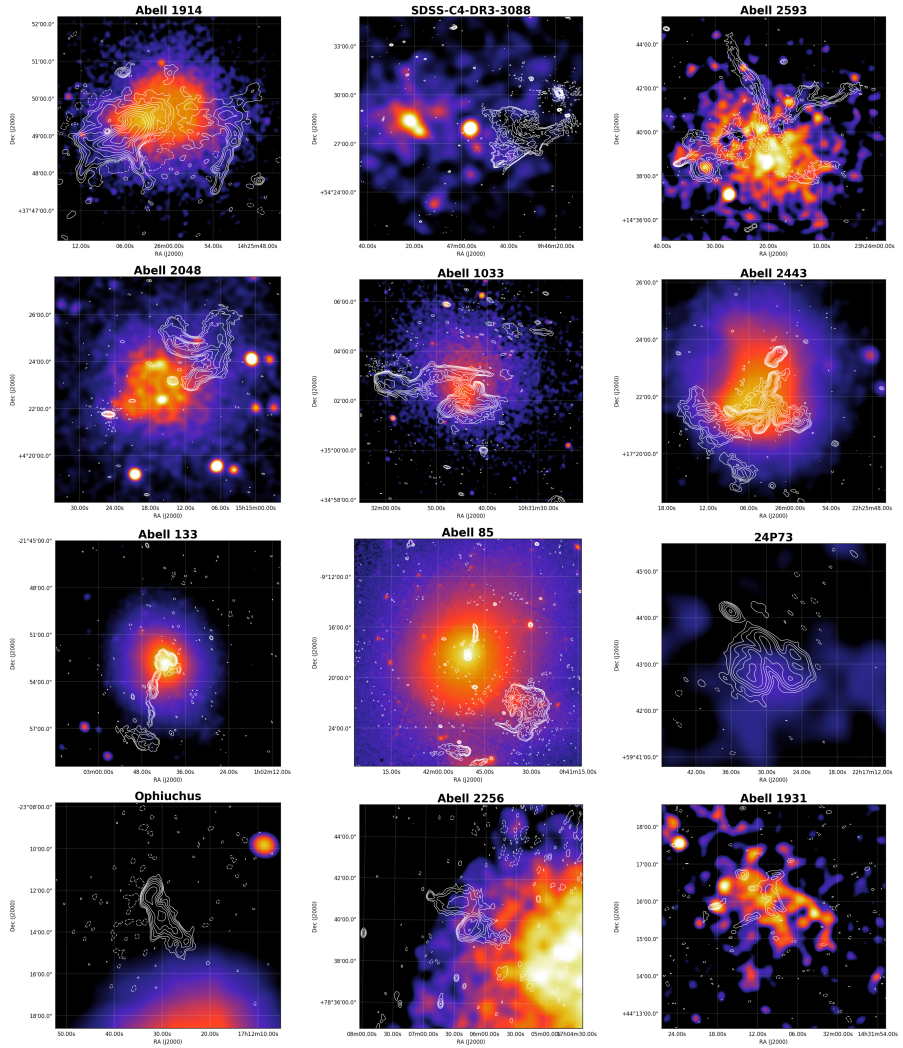


Figure 4.3: Full-resolution radio (LOFAR 150 MHz / GMRT 325 MHz/ GMRT 610 MHz) images of the radio phoenixes. The black ellipses are marked to visualise the candidate radio phoenix. In each of the radio images, the black contours and dashed lines show the $(1, 2, 4, \dots) \times 5 \times \sigma_{\text{radio}}$ and $-3 \times \sigma_{\text{radio}}$ levels, respectively. σ_{radio} is the measured rms noise in the respective radio maps. The beam size is labelled in every image at the bottom left corner.



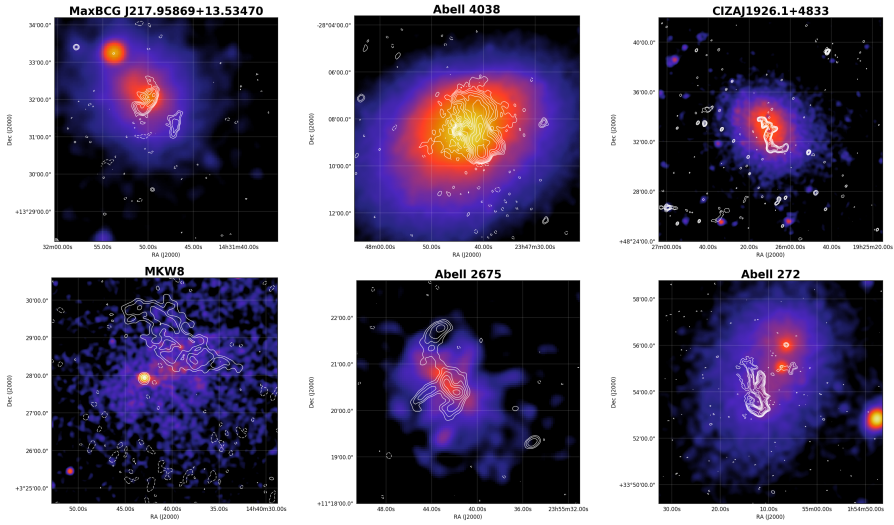
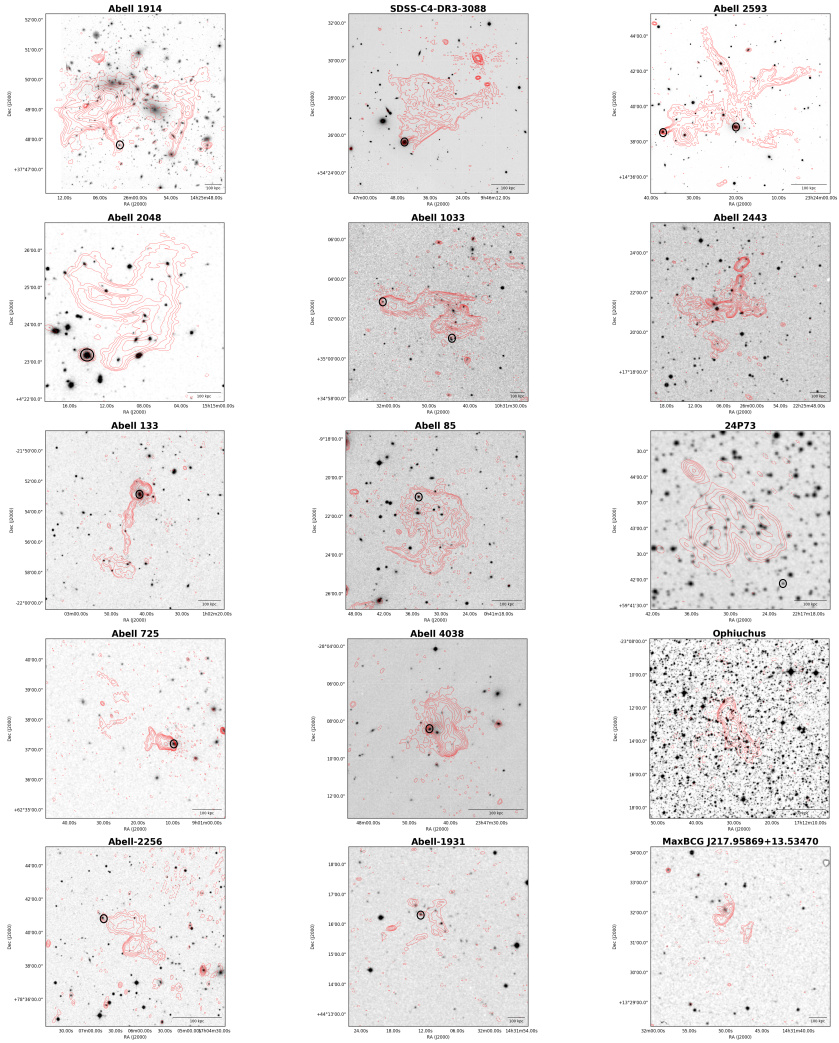


Figure 4.3: Full-resolution radio (LOFAR 150 MHz / GMRT 325 MHz / GMRT 610 MHz) image contours (white; as shown in the Figure 4.3) of all the radio phenices, overlaid on exposure-corrected *Chandra* or *XMM-Newton* images in the 0.5-2.0 keV energy band. The observation details are provided in Table 4.2. In the radio image contours, solid and dashed white lines show the $(1, 2, 4, \dots) \times 5 \times \sigma_{\text{radio}}$ and $-3 \times \sigma_{\text{radio}}$ levels, respectively where σ_{radio} is the local rms noise in the radio images.



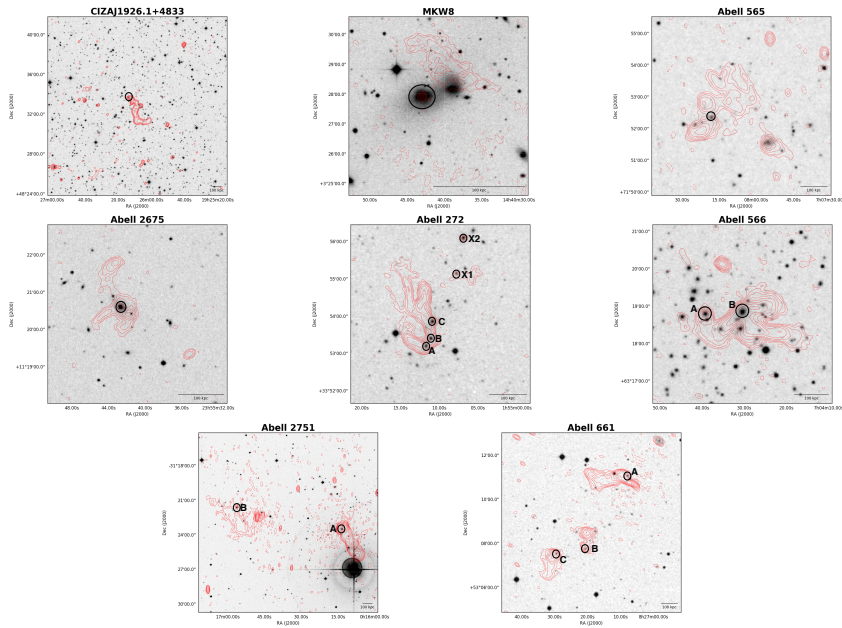


Figure 4.4: Full-resolution radio (LOFAR 150 MHz / GMRT 325 MHz / GMRT 610 MHz) image contours (red; as shown in the Figure 4.3) of all the radio phoenixes, overlaid on DSS r-band optical images. In the radio image contours, solid and dashed red lines show the $(1, 2, 4, \dots) \times 5 \times \sigma_{\text{radio}}$ and $-3 \times \sigma_{\text{radio}}$ levels, respectively, where σ_{radio} is the local rms noise in the radio images.

4.A GMRT Maps

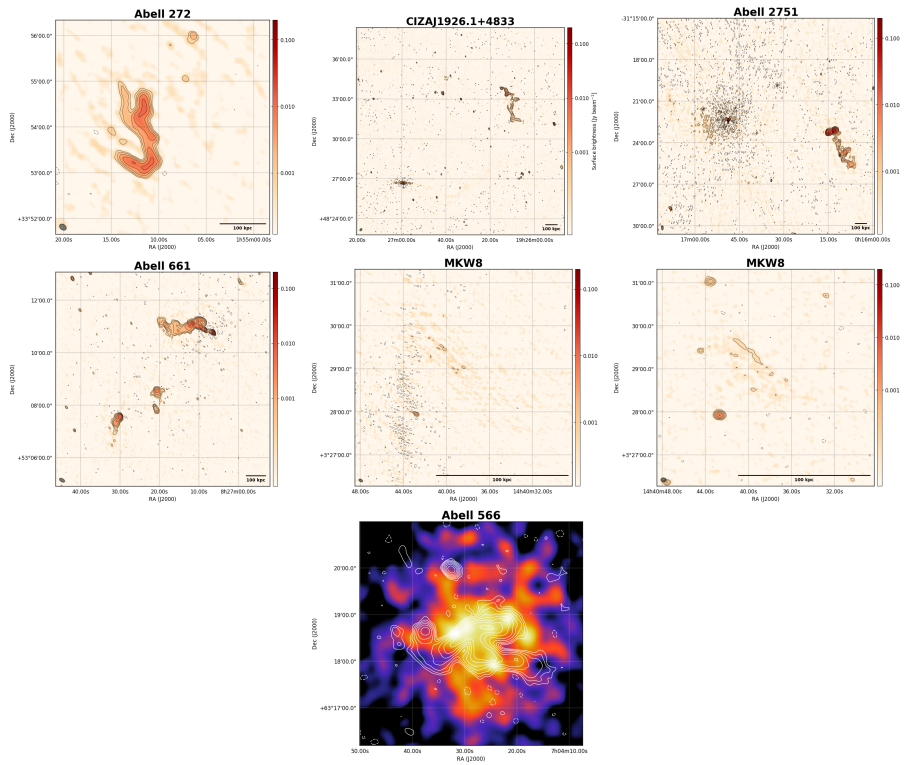


Figure 4.5: Additional radio and X-ray images. Top row (left to right): Abell 272 (GMRT 325 MHz); CIZAJ1926.1+4833 (GMRT 610 MHz); Abell 2751 (GMRT 610 MHz). Middle row (left to right): Abell 661 (GMRT 610 MHz); MKW8 (GMRT 610 MHz) and MKW8 (VLA 1.4 GHz). Bottom row: Abell 566 Suzaku image.

Table 4.5: Total flux density measurements of candidate radio phenices at 150, 325 and 1400 MHz

Sources (Jy)	150 MHz (Jy)	325 MHz (Jy)	1400 MHz (Jy)
Abell 1914	4.68±0.46	0.83±0.08	0.040±0.002
SDSS-C4-DR3-3088	1.83±0.18	0.45±0.05	0.021±0.002
Abell 2593	3.57±0.36	1.45±0.15	0.290±0.012
Abell 2048	1.57±0.25	0.55±0.06	0.019±0.004
Abell 1033	1.30±0.01	0.46±0.05	0.046±0.001
Abell 2443	3.65±0.4	0.41±0.07	0.007±0.0006
Abell 133	10.9±1.2	4.19±0.42	0.210±0.024
Abell 85	8.33±0.7	2.86±0.30	0.042±0.003
24P73	1.40±0.01	0.41±0.04	0.012±0.003
Ophiuchus	6.38±0.32	2.60±0.13	0.630±0.032
Abell 2256	0.57±0.06	0.34±0.03	0.020±0.001
Abell 1931	0.04±0.008	0.004±0.0008	0.0005±0.001
MaxBCG J217.95869+13.53470	0.14±0.01	0.06±0.01	0.001±0.0005
Abell 725	0.75±0.08	0.39±0.04	0.110±0.006
Abell 4038	4.30±0.5	1.40±0.15	0.060±0.003
Abell 13	2.80±0.6	0.63±0.10	0.030±0.002
Abell S753	10.1±0.04	8.50±0.00	0.460±0.0
CIZAJ1926.1+4833	1.15±0.01	0.33±0.03	0.011±0.001
MKW8	1.12±0.11	0.27±0.03	0.002±0.0002
Abell 565	0.27±0.03	0.10±0.01	0.005±0.0003
Abell 2675	0.26±0.03	0.10±0.01	0.008±0.0004
Abell 272	0.75±0.08	0.21±0.02	0.006±0.0003
Abell 566	6.61±0.7	1.54±0.20	0.052±0.001
Abell 2751	0.31±0.03	0.17±0.02	0.024±0.001
Abell 661	0.42±0.04	0.26±0.03	0.055±0.001

Chapter 5

Extremely deep 150 MHz source counts from the LoTSS Deep Fields

Based on
S. Mandal, I. Prandoni, M. J. Hardcastle, T. W. Shimwell, H. T. Intema,
C. Tasse, R. J. van Weeren, H. Algera, K. L. Emig, H. J. A. Röttgering,
D. J. Schwarz, T. M. Siewert, P. N. Best, M. Bonato, M. Bondi, M. J. Jarvis,
R. Kondapally, S. K. Leslie, V. H. Mahatma, J. Sabater,
E. Retana-Montenegro, W. L. Williams et al. Submitted to A&A

5.1 Introduction

Large-area radio surveys are very important for statistical studies of radio source populations, addressing astrophysical properties and cosmological evolution of radio galaxies, quasars and starburst galaxies. In the past, several wide-area radio surveys were carried out at low radio frequencies, such as the Cambridge Surveys (3C, 4C, 6C, and 7C at around 160 MHz: [Edge et al. 1959](#), [Bennett 1962](#), [Pilkington & Scott 1965](#), [Gower et al. 1967](#), [Baldwin et al. 1985](#)). However, calibration of low-frequency radio data is challenging due to the direction-dependent, time-varying effects of the ionosphere that affects both the amplitude and the phase of the radio signal. Since these effects are only prominent in the MHz regime, the focus of wide-area/all-sky radio surveys switched to around 1 GHz in the last decades, resulting in the NRAO VLA Sky Survey (NVSS: [Condon et al. 1998](#)), the Sydney University Molonglo Sky Survey (SUMSS: [Mauch et al. 2003](#)) and the Faint Images of the Radio Sky at Twenty-Centimeters (FIRST) survey ([Becker et al. 1995](#); [White et al. 1997](#)).

The higher sensitivity and higher spatial resolution of surveys at GHz frequencies also allowed us to probe deeper and deeper flux densities, and today we have several deep surveys covering degree-scale fields, and sensitive to the sub-mJy and μ Jy radio populations (see e.g. [Prandoni et al. 2000a,b, 2006](#); [Hopkins et al. 2003](#); [Schinnerer et al. 2004, 2007](#); [Hales et al. 2014b](#); [Smolčić et al. 2017](#); [Prandoni et al. 2018](#)). After many years of studies, it is now well established that the sub-mJy radio population has a composite nature. Radio-loud (RL) active galactic nuclei (AGNs) are dominant down to 1.4 GHz flux densities of 200-300 μ Jy and star-forming galaxies (SFGs) become dominant below about 100-200 μ Jy ([Smolčić et al. 2008](#); [Bonzini et al. 2013](#); [Prandoni et al. 2018](#); [Bonato et al. 2020](#)). A significant fraction of the sources below 100 μ Jy can also show signatures of AGN activity in the host galaxy at other bands (IR, optical, X-ray), but rarely display the large-scale radio jets and lobes typical of classical radio galaxies. Most of them are unresolved or barely resolved on a few arcsec scale, i.e. on scales similar to the host galaxy size. The origin of the radio emission in these (so-called radio-quiet) AGN is debated: it may come from star formation in the host galaxy ([Padovani et al. 2011, 2015](#), [Bonzini et al. 2013, 2015](#); [Ocran et al. 2017](#); [Bonato et al. 2017](#)) or from low-level nuclear activity ([White et al. 2015, 2017](#); [Maimi et al. 2016](#); [Herrera Ruiz et al. 2016, 2017](#); [Hartley et al. 2019](#)). Most likely, such AGN are composite systems where star formation and AGN-triggered radio emission co-exist over a wide range of relative contributions (e.g. [Delvecchio et al. 2017](#)). This scenario is also supported

by the modeling work of [Mancuso et al. \(2017\)](#), see also [Macfarlane et al. in prep.](#)).

Being sensitive to SFGs up to the epoch of the peak of their activity ($z \sim 2 - 3$), and reaching for the first time the dominant radio-quiet (RQ) AGN population, deep radio surveys probing the μJy regime can be used as a very important dust/gas-obscuration-free tool to study both AGN activity and star formation and how they evolve with cosmic time. However, to overcome uncertainties introduced by low statistics, cosmic variance effects ([Heywood et al. 2013](#)) and other systematics ([Condon et al. 2012](#)), deep-radio surveys that cover wide areas ($\gg 1 \text{ deg}^2$) and have multi-band ancillary data are needed. Such wide-area surveys are also useful to investigate the role of environment in driving the growth of galaxies and SMBH, and to better trace rare radio source populations.

With the advent of a new generation of low-frequency telescopes and better data processing techniques we can now revisit the radio sky at low-frequency. With the Murchison Widefield Array (MWA; [Lonsdale et al. 2009](#)), [Wayth et al. \(2015\)](#) have carried out the GaLactic and Extragalactic All-sky MWA survey (GLEAM; [Hurley-Walker et al. 2017](#)), reaching a sensitivity of a few mJy beam^{-1} at a resolution of a few arcminutes. The GMRT has significantly improved the low-frequency view of the radio sky in terms of sensitivity and angular resolution. This has already been shown in a few low-frequency surveys centred around 150 MHz (e.g.: [Ishwara-Chandra et al. 2010](#), [Sirothia et al. 2009](#), [Intema et al. 2011](#), [Intema et al. 2017](#)).

The Low Frequency Array (LOFAR; [van Haarlem et al. 2013](#)) is one of the key pathfinders to the Square Kilometre Array (SKA). Most of the LOFAR antennas are based in the Netherlands, with baseline lengths ranging from 100 meters to 120 km. Additional remote stations are located throughout various countries in Europe. The longest baseline of LOFAR can provide a resolution of $0.3''$ at 150 MHz. The combination of LOFAR's large field of view, wide range of baseline lengths, and large fractional bandwidth makes it a powerful instrument for performing large area and deep sky surveys. The LOFAR Two Meter Sky Survey (LoTSS) is an ongoing project in which the whole northern sky is observed with a sensitivity better than $100\mu\text{Jy beam}^{-1}$ at the resolution of $6''$ allowed by the Dutch LOFAR stations. The first data release (DR1) is described by [Shimwell et al. \(2017\)](#) and [Shimwell et al. \(2019\)](#). The LoTSS also includes deeper observations of a number of pre-selected regions, where the aim is to eventually reach an rms depth of $10 \mu\text{Jy beam}^{-1}$ at 150 MHz ([Röttgering et al. 2011](#)). In order to scientifically exploit these more sensitive surveys (collectively known as LoTSS Deep Fields), complementary multi-wavelength data

are necessary, most notably to identify the host galaxies of the extra-galactic radio sources and determine their redshift. For this reason observations were focused on fields with the highest quality multi-wavelength data available. The Lockman Hole, the Boötes and the European Large-Area ISO Survey-North 1 (ELAIS-N1) fields are the deepest of the LoTSS Deep Fields so far (see Tasse et al 2020; Sabater et al. 2020; respectively paper I and II of this series). All have rich multi-wavelength ancillary data, covering a broad range of the electromagnetic spectrum, from X-ray to radio bands.

The Lockman Hole (LH hereafter) is one of the best studied extragalactic regions of the sky. It is characterized by a very low column density of Galactic HI (Lockman et al. 1986) making it an ideal field to study extragalactic sources with deep observations in the mid-IR/FIR/sub-mm (Lonsdale et al. 2003; Mauduit et al. 2012, Oliver et al. 2012), optical/NIR (Muzzin et al. 2009; Fotopoulou et al. 2012; Hildebrandt et al. 2016), and X-ray (Polletta et al. 2006, Brunner et al. 2008). A variety of radio surveys cover limited areas within the LH region, at several frequencies. The widest deep radio survey so far consists of a 6.6 deg². 1.4 GHz mosaic obtained with the Westerbork (WSRT) telescope (1σ sensitivity $\sim 10 \mu\text{Jy beam}^{-1}$; Prandoni et al. 2018). We refer to Prandoni et al. (2018) for a comprehensive summary of the available multi-frequency and multi-band coverage in this region (see also Kondapally et al. 2020, paper III of this series).

The Boötes (Boo hereafter) field was originally targeted as part of the NOAO Deep Wide Field Surveys (NDWFS; Jannuzi & Dey 1999) which covers ~ 9 deg² in the optical and near infrared (K) bands. Ancillary data is available for this field including X-ray (Murray et al. 2005; Kenter et al. 2005), UV (GALEX; Martin et al. 2003), and mid-infrared (Eisenhardt et al. 2004). Radio observations have also been carried out at 153 MHz with the GMRT (Intema et al. 2011; Williams et al. 2013), at 325 MHz with the VLA (Croft et al. 2008, Coppejans et al. 2015) and at 1.4 GHz with the WSRT (de Vries et al. 2002).

The Elais-N1 (EN1 hereafter) field has deep multi-wavelength ($0.15\mu\text{m} - 250\mu\text{m}$) data taken as part of many different surveys (optical: the Panoramic Survey Telescope and Rapid Response System; Pan-STARRS (Chambers et al. 2016) and Hyper-Suprime-Cam Subaru Strategic Program (HSC-SSP) survey, u-band: Spitzer Adaptation of the Red-sequence Cluster Survey; SpARCS: Muzzin et al. 2009, UV: Deep Imaging Survey (DIS): Martin et al. 2005, NIR J and K band: the UKIDSS Deep Extragalactic Survey (DXS) DR10 (Lawrence et al. 2007), MIR: IRAC instrument on board the Spitzer Space Telescope: SWIRE; Lonsdale et al. 2003 and The Spitzer Extragalactic Representative Volume Survey (SERVS; Mauduit et al. 2012).

Mahony et al. (2016) presented the first LOFAR 150 MHz map of the LH

Table 5.1: An overview of the statistical properties of the three LoTSS Deep Fields.

Field	R.A. (hh:mm:ss)	DEC. (dd:mm:ss)	Obs. Time (hr)	σ_c ($\mu\text{Jy beam}^{-1}$)	Area _{full} (deg ²)	N_S^{raw}	$\sigma_{\text{med}}^{\text{full}}$ ($\mu\text{Jy beam}^{-1}$)	Area _{masked} (deg ²)	N_S^{final}	$\sigma_{\text{med}}^{\text{masked}}$ ($\mu\text{Jy beam}^{-1}$)
LH	10:47:00.0	+58:04:59.0	112	22	25.0	50112	40	10.3	31162	29
Boo	14:32:00.0	+34:30:00.0	80	32	26.5	36767	58	8.6	19179	42
EN1	16:11:00.0	+55:00:00.0	164	17	24.3	69954	31	6.7	31610	21

Notes: the columns are as follows: pointing centre (R.A. and DEC); total observing time; RMS noise reached at the center of the image (σ_c); area covered by the raw catalogue (Area_{full}), number of sources in the raw catalogue (N_S^{raw}) and median RMS noise in the area covered by the raw catalogue ($\sigma_{\text{med}}^{\text{full}}$); same parameters for the final catalogue (Area_{masked}, N_S^{final} , $\sigma_{\text{med}}^{\text{masked}}$).

with a sensitivity of $160 \mu\text{Jy beam}^{-1}$ at a resolution of $18.7'' \times 16.4''$. [Williams et al. \(2016\)](#) presented the first LOFAR map of the Boo field at a resolution of $5.6'' \times 7.4''$ with an rms of $120 \mu\text{Jy beam}^{-1}$. A deeper image of the Boo field, reaching an rms of $55 \mu\text{Jy}$ at its center, was presented by [Retana-Montenegro et al. \(2018\)](#). [Tasse et al. \(2020, paper I\)](#) present the deepest, high-resolution ($6''$) low-frequency images and catalogues of the LH and Boo fields at 150 MHz and also describe the general method followed for the data reduction of the LoTSS Deep Fields. The even deeper LOFAR observations of the EN1 field are presented separately by [Sabater et al. \(2020, paper II\)](#).

One of the immediate science products of deep radio surveys is the determination of the radio source counts, which can provide useful comparison with counts predictions based on evolutionary models of radio source populations. In the present paper, we collectively exploit the LH, Boo and EN1 deep LOFAR data to derive the deepest radio source counts at 150 MHz ever. The derived source counts are compared with other existing determinations, as well as with state-of-the-art radio source evolutionary models (e.g. [Wilman et al. 2008](#); [Mancuso et al. 2017](#); [Bonaldi et al. 2019](#)).

The outline of the paper is as follows. In Section 2 the data reduction and the imaging process followed to obtain the deep images of the LH, Boo and EN1 are described in brief. In Section 3, we summarize the source extraction process and we describe the derived source catalogues and corresponding properties. This is followed by an analysis of the source size distribution and of the catalogue incompleteness due to resolution bias (Section 4). Eddington bias and related incompleteness are discussed in Section 5. Section 6 presents the derived 150 MHz source counts and their comparison with state-of-the-art evolutionary models. We summarize our results in Section 7. Throughout this paper, we have used the convention $S_\nu \propto \nu^\alpha$.

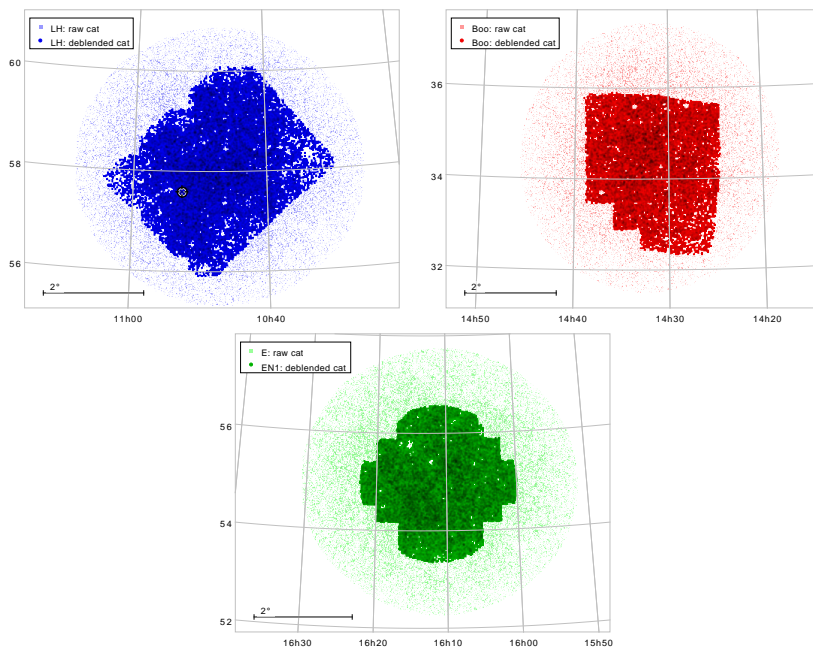


Figure 5.1: LH (top left), Boo (top right) and EN1 (bottom) fields targeted by LOFAR at 150 MHz. Light colors refer to the raw catalogues, cut at a distance from the pointing center of 0.3 of the LOFAR 150 MHz primary beam power. Darker colors refer to the final catalogues. The varying shape of their footprints highlights the regions with available optical/IR data. The areas of the optical/IR footprints are listed in Table 5.1.

5.2 Observations and Data reduction

The observations and data reduction of the LoTSS Deep Fields are described in detail in paper I, but for completeness we provide a brief summary below.

Each of the deep fields was observed using the LOFAR High Band Antenna (HBA) in its HBA_DUAL_INNER mode. Observations were taken in approximately 8hr blocks and the total integration times were 112, 80 and 164 hours for the LH, Boo and EN1 fields respectively¹. The phase centers of the three pointings are listed in Table 5.1 (R.A., DEC.). The calibration of the data was completed in two steps. Firstly a direction independent calibration was performed using the PREFACTOR pipeline² which is described in [van Weeren et al. \(2016a\)](#) and [Williams et al. \(2016\)](#) and corrects for direction independent effects (see [de Gasperin et al. 2019](#)). To efficiently deal with the large data rates, this pipeline is run on a compute cluster connected to the LOFAR archive (see [Mechev et al. 2018](#) and [Drabent et al. 2019](#)). The resulting data products are then calibrated with the latest version of DDF-PIPELINE³ which is briefly outlined in Section 5.1 of [Shimwell et al. 2019](#) and detailed by paper I. This pipeline is based on the kMS solver ([Tasse 2014](#); [Smirnov & Tasse 2015](#)) and the DDFacet imager ([Tasse et al. 2018](#)) to calibrate for direction-dependent effects, such as ionosphere-induced and beam model errors, and apply these solutions whilst imaging.

As described in [Tasse et al. \(2018\)](#), for each deep field a single good observation is selected and run through DDF-PIPELINE. The resulting sky model, together with all observations from that particular field, are then input into a second run of DDF-PIPELINE which calibrates all the data off that sky model, before imaging all the data together and completing a final round of direction independent and direction-dependent self-calibration. The frequency coverage used to produce the images is 120 MHz to 168 MHz for Boo and LH and 115 MHz to 177 MHz for EN1⁴.

As described in papers I and II, the peak and integrated flux densities of the final images were rescaled by factors of 0.920, 0.859 and 0.796 for the LH, Boo and EN1 fields respectively. These scaling factors were derived from the comparison of the LOFAR flux densities with a variety of shallower radio surveys available at various frequencies over these fields. The minimum sensitivity

¹A full overview of the observation details is given in Table 1 of paper I (for the LH and the Boo fields) and in Table 1 of Paper II (for the EN1 field).

²<https://github.com/lofar-astron/prefactor>

³<https://github.com/mhardcastle/ddf-pipeline>

⁴The exact central frequency of the imaged band is therefore 144 MHz for LH and Boo, and 146 MHz for EN1.

reached at the center of the images (after rescaling) is $\sigma_c \sim 22, 32, 20 \mu\text{Jy beam}^{-1}$, respectively, at a resolution of $6''$ (see Table 5.1). Although dynamic range effects are present around bright sources, in all cases the final image noise levels are within $\sim 10\%$ of the noise levels predicted from 8-hr depths, assuming an rms scaling with time $t^{-0.5}$. We note that the noise measured in the Boo field is higher compared to the other two, also due to its lower declination.

5.3 Source extraction, masking and deblending

Initial source catalogues were extracted in each field using the PYthon Blob Detector and Source Finder (PYBDSF: Mohan & Rafferty 2015). The strategy followed for LH and Boo is detailed in paper I. In brief, the source detection threshold was set at 5σ for the peak flux and at 3σ for the definition of the contiguous pixels used for the source Gaussian fitting, where σ is defined as the local rms noise at the source position. To measure the background noise variations across the images, a sliding box of the size of 40×40 synthesized beams was used. For high signal-to-noise (≥ 150) sources, the box size was reduced to 15×15 synthesized beams in order to capture the increased local noise level more accurately. For EN1 a slightly different set of parameters was used (see Table C.1 of paper II). The PyBDSF wavelet decomposition mode was used in all fields to better describe complex sources characterized by very extended emission. A flag is assigned to each source according to the number of Gaussian components fitted: ‘S’ and ‘M’ refer to sources fitted by a single and multiple Gaussian components respectively, whereas ‘C’ means that the source lies within the same island as another source. For a more detailed description of the method and format of the catalogues, see the webpage⁵ and Shimwell et al. (2019). The catalogues were cut at a distance from the pointing centre roughly corresponding to 0.3 of the 150 MHz LOFAR primary beam power (corresponding to fields of view of about 25 deg^2). The footprints of these initial catalogues (hereafter referred to as *raw* catalogues) are shown in light colors in Figure 5.1. The total number of sources over these footprints is respectively 50, 112 (LH), 36, 767 (Boo) and 69, 954 (EN1).

Deep and wide optical and IR data are available over part of the LoTSS Deep Fields. Over these common sub-regions, we could carry out an extensive process of multi-wavelength cross-matching and source characterisation, that allowed us to produce a cleaner and more reliable radio source catalogue. This

⁵<http://www.astron.nl/citt/pybdsf/>

process is extensively described by paper III, and only briefly reported here. Using a combination of statistical techniques and visual cross-matching, distinct PyBDSF components belonging to the same physical radio sources were grouped together to form multiple-component and/or complex radio sources. In addition, PyBDSF components were identified that needed to be deblended into separate Gaussian components associated with different host galaxies. In the same process, using the deep multi-wavelength datasets we were able to identify the host galaxies of over 97% of the detected radio sources⁶. After masking, the catalogues cover respectively 10.3 deg² (LH), 8.6 deg² (Boo) and 6.7 deg² (EN1), and collect respectively 31,163 (LH), 19,179 (Boo) and 31,645 (EN1) sources. In the following we will refer to these deblended/associated catalogues as *final* catalogues. The footprints of the final catalogues are shown in dark colors in Figure 5.1. The irregular shape of these footprints follows the optical/IR sky coverage. We note that ‘holes’ are present in such footprints, due to the fact that regions with very bright optical and/or radio sources (which typically produce artifacts in their surroundings) were masked.

In addition we have pixel-matched the images in each waveband and extracted aperture-matched photometry from ultraviolet to infrared wavelengths, deriving high-quality photometric redshifts for around 5 million objects across the three fields (see Duncan et al., 2020, paper IV of this series, for more details). The raw and final radio catalogues, as well as the optical/IR and photometric catalogues, are available on the LOFAR Surveys Data Release site web-page⁷.

5.3.1 Visibility function of raw and final catalogues

Figure 5.2 shows the so-called visibility function (i.e. the cumulative fraction of the total area of the noise map characterized by noise measurements lower than a given value) for the LH (blue), Boo (red) and EN1 (green) fields. Raw and final catalogues are indicated respectively by the dashed and solid lines. We note that the visibility functions of final catalogues are significantly steeper than those of the raw catalogues. This is due to the fact that the final catalogues are mostly confined in the inner, most sensitive parts of the LOFAR fields. As a consequence the median noise is significantly lower for final than for raw catalogues (see Table 5.1).

⁶97.6% for EN1 and LH; 96.9% for Boo.

⁷<http://www.lofar-surveys/releases.html>

Table 5.2: Parameters describing the unresolved/resolved sources' dividing lines (see Eqs. 5.2 and 5.3) for the LH, Boo and EN1 catalogues.

Field	A	B	% _{resolved}	
			raw	final
LH	1.15	3.0	34	25
Boo	1.00	2.0	47	38
EN1	1.07	3.0	35	24

5.3.2 Source Size Deconvolution

Characterisation of resolved versus unresolved sources in our catalogues is important in order to correct the catalogues for the incompleteness introduced by so-called *resolution bias* (described in Section 5.4). The total flux density (S_{total}) of a source can be written as:

$$S_{\text{total}}/S_{\text{peak}} = \theta_{\text{maj}}\theta_{\text{min}}/b_{\text{min}}b_{\text{maj}} \quad (5.1)$$

where S_{peak} is the source peak flux density, θ_{min} and θ_{maj} are the source full-width-half-maximum (FWHM) axes, and b_{min} and b_{maj} are the restoring beam FWHM axes. In an ideal image, in the absence of noise, the total flux density of a point source is equal to its peak flux density. In real images both the total and peak flux measurements of point sources are affected by errors. This means that not all sources with $S_{\text{total}} > S_{\text{peak}}$ would be genuinely resolved sources. The $S_{\text{total}}/S_{\text{peak}}$ ratio as a function of signal-to-noise ratio ($\text{SNR} = S_{\text{peak}}/\sigma$, where σ is the local rms noise), can be used to establish a statistical criterion to establish if a source is likely extended or point-like (see e.g. Prandoni et al. 2000b, 2006). In Figure 5.2, the ratio of the total to peak flux densities is shown as a function of SNR for both raw and final catalogues. A lower envelope of the source distribution can be defined by the following equation:

$$S_{\text{total}}/S_{\text{peak}} = A/(1 + B/\text{SNR}) \quad (5.2)$$

where A and B are two free parameters (see dashed lines in each panel of Fig. 5.2). As expected, going to higher SNR, measurement errors get smaller. At $\text{SNR} \gg 100$ the 2nd term of Eq. 5.2 can be neglected, and the $S_{\text{total}}/S_{\text{peak}}$ tends to A. In an ideal case, where radial smearing is taken care of, the ratio of the total over the peak flux density for point sources should converge to a value

of $A=1$ at very high SNRs. The DDFacet pipeline implements a facet dependent PSF which, for deconvolved sources, accounts for the impact of time and bandwidth smearing (Tasse 2014). However, due to imperfect calibration of the PSF across the field and/or smearing of sources due to ionospheric distortions, the value of the ratio at high signal-to-noise sources can be found to be higher than 1 and can be field-dependent (as ionospheric effects are time and spatially dependent). The values of A for the LH, Boo and EN1 field are respectively 1.15, 1.00 and 1.07 (see Table 5.2). This could potentially mean that the Boo field is less affected by ionospheric smearing when compared with LH and EN1. The B value also changes depending on the field, with Boo showing a lower value than LH and EN1 (see Table 5.2), again indicating smaller errors in the determination of source flux densities. We notice that the parameters given in Table 5.2 provides a good description of both raw and final catalogues. The lower envelopes can then be mirrored around the $S_{\text{total}}/S_{\text{peak}} = A$ axis to get the upper envelopes:

$$S_{\text{total}}/S_{\text{peak}} = A \cdot (1 + B/\text{SNR}) \quad (5.3)$$

Sources lying above the upper envelopes (dashed black lines in each panel) are then considered to be truly extended or resolved sources. Sources below the upper envelopes are considered to be point sources. The fraction of resolved sources in each field is given in Table 5.2. In final catalogues the fraction of resolved sources vary from 24-25% (EN1 and LH) to 38% (Boo). The $\sim 10\%$ higher fractions observed in raw catalogues reflect the larger number of bright extended sources detected in their larger FoV. These fractions should be considered as indicative, as they depend on the criteria used to define them. Sabater et al., for instance, as part of their detailed analysis of the EN1 field, used more stringent criteria, which also include additional sources of errors for the source fluxes, and estimated that between 4 and 11% of the sources in the EN1 raw catalogues are genuinely extended (see paper II for more details). Nevertheless, we decided to apply the same approach to all fields, and to both final and raw catalogues, to enable a consistent statistical analysis of the source size distribution in the three fields (see Sect. 5.4).

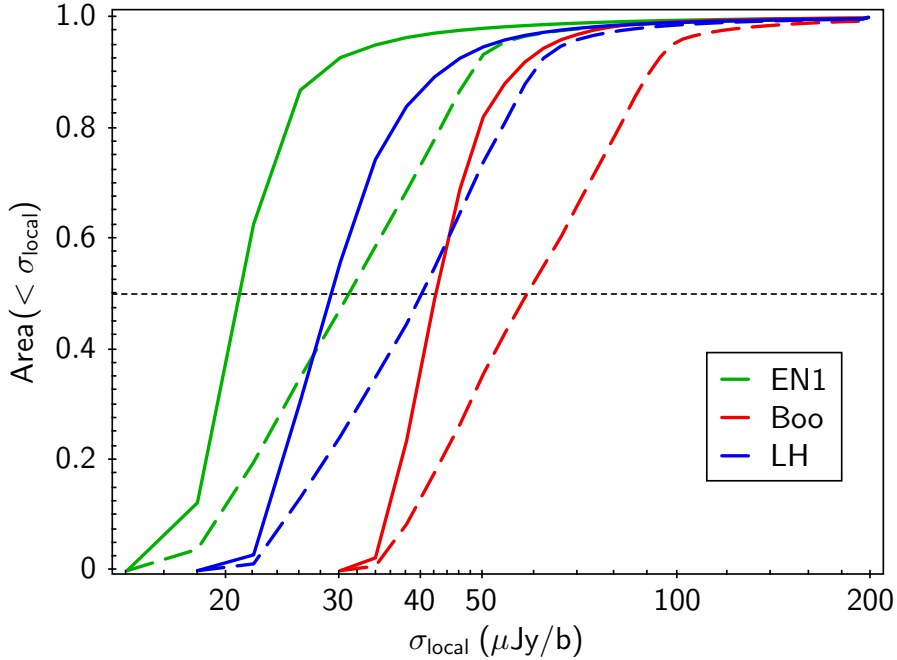
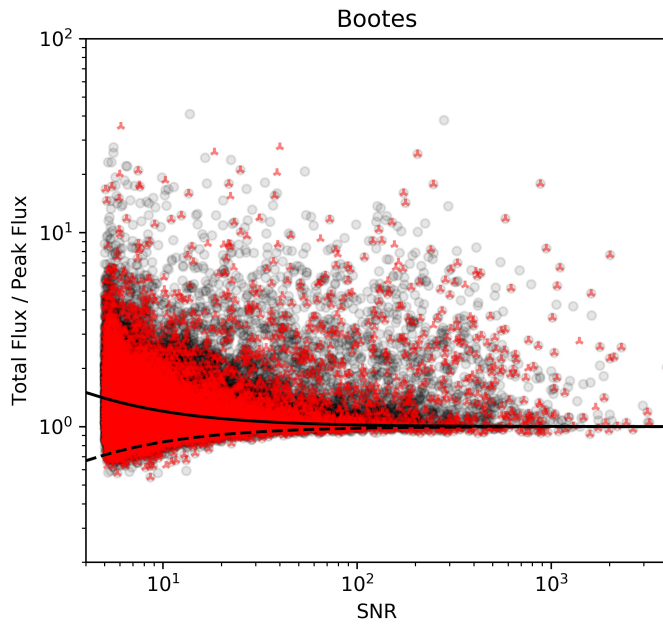
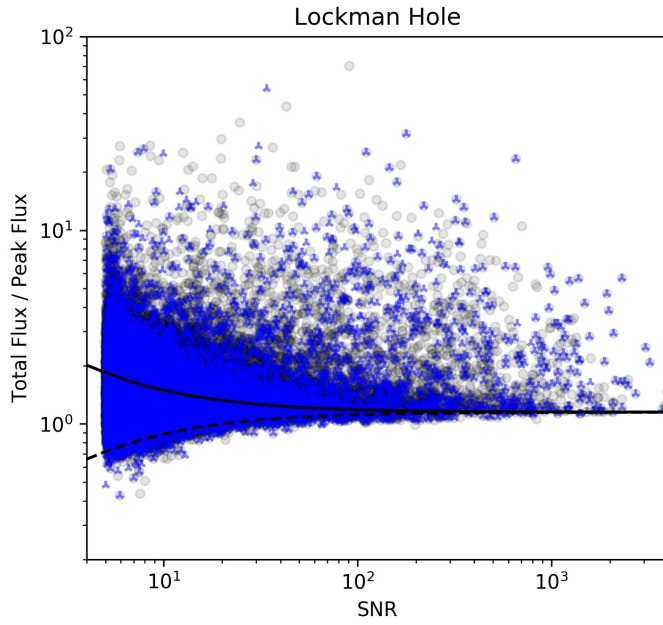


Figure 5.2: Visibility functions of the raw (dashed lines) and final (solid lines) catalogues presented in this paper. Blue, red and green colors correspond to the LH, Boo and EN1 fields, respectively. The visibility functions represent the cumulative fraction of the total area of the noise map characterized by a noise lower than a given value. We caveat that the total area covered by the final catalogues is much smaller than the one covered by the raw catalogues (see Tab. 5.1).



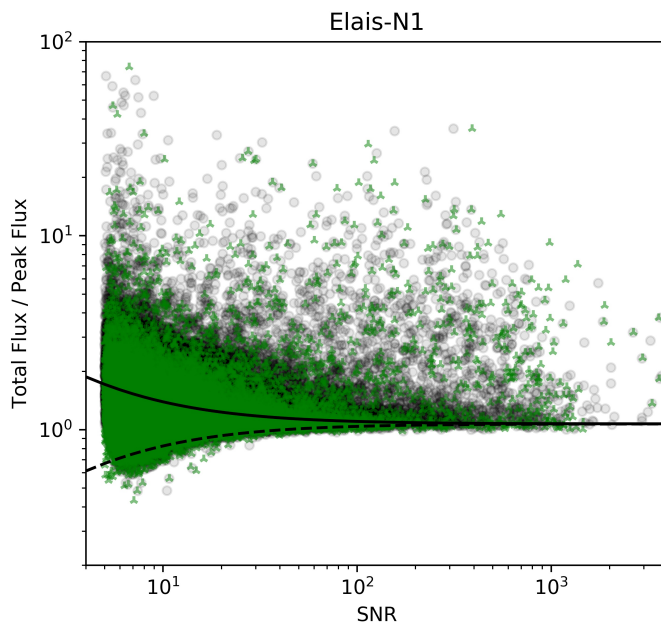


Figure 5.2: Total to peak flux density ratio as a function of signal to noise ratio ($\text{SNR} = S_{\text{peak}}/\sigma$) for both the raw (black transparent circles) and final (\blacktriangle symbols in blue, red and green colors) catalogues in the LH, Boo and EN1 fields (respectively from *top left* panel). The dashed and solid lines represent the unresolved source distribution lower and upper envelopes respectively (see text for more details).

5.4 Source Size Distribution and Resolution Bias

In deriving the source counts, the completeness of the catalogues in terms of total flux density needs to be estimated. Such completeness depends on source angular sizes, since, as shown by Eq. 5.1, a larger source of a given total flux density will drop below the 5σ limit of a survey more easily than a smaller source of the same total flux density. This effect, called *resolution bias*, results from the fact that the detection of a source depends on its peak flux. Following Prandoni et al. (2001b, 2006), we can use Eq. 5.1 to calculate the approximate maximum deconvolved size (Θ_{\max}) a source of a given total flux, S_{total} , can have before dropping below the 5σ limit of the catalogue:

$$\Theta_{\max} = \Theta_N \sqrt{(S_{\text{total}}/(5\sigma) - 1)} \quad (5.4)$$

where $\Theta_N \equiv \sqrt{b_{\text{maj}}b_{\text{min}}}$ is the geometric mean of the restoring beam axes. In our case $\Theta_N = b_{\text{maj}} = b_{\text{min}} = 6''$.

In Figure 5.3 we show the deconvolved source sizes as a function of the total flux density for both raw and final catalogues. Each panel corresponds to a different field: LH (top-left), Boo (top-right) and EN1 (bottom). Deconvolved sizes are defined as the geometric mean of the major and minor FWHM axes, except for well resolved radio galaxies, which are better described by their major axis. Deconvolved sizes of point sources are set to zero. As expected, the upper envelope of the source size distributions approximately follow the $\Theta_{\max} - S_{\text{total}}$ relation (short-long-dashed line) in all fields.

Equations 5.1 and 5.3 can also be used to derive an approximate minimum intrinsic angular size (Θ_{\min}) that can be resolved reliably as a function of the source peak flux density:

$$\Theta_{\min} = \Theta_N \sqrt{A \cdot (1 + B/\text{SNR}) - 1} . \quad (5.5)$$

The curve representing Θ_{\min} is shown in Figure 5.3 by the solid lines.

In order to quantify the fraction of sources larger than Θ_{\max} , and in turn the incompleteness affecting our catalogue, we need to know the true intrinsic radio source size distribution within the flux range probed by our survey. We start assuming the empirical integral distribution proposed by Windhorst et al. (1990) for 1.4 GHz-selected samples:

$$h(> \Theta) = \exp[-\ln 2 (\Theta/\Theta_{\text{med}})^q] \quad (5.6)$$

where $q = 0.62$ and the median source size varies with the total flux density as follows:

$$\Theta_{\text{med}} = k \times (S_{1.4\text{GHz}})^m \quad (5.7)$$

with $k=2''$, $m = 0.3$, $S_{1.4\text{GHz}}$ expressed in mJy. The Windhorst et al. (1990) relations are extensively used in the literature to estimate the resolution bias, either for 1.4 GHz selected samples (see e.g. Prandoni et al. 2001b, 2018; Huynh et al. 2005; Hales et al. 2014b), or for surveys at other frequencies, including LOFAR HBA ones (Mahony et al. 2016; Williams et al. 2016; Retana-Montenegro et al. 2018). We converted the median size - flux relation to 150 MHz assuming a spectral index $\alpha = -0.7$. This assumption is appropriate for radio catalogues dominated by faint sub-mJy radio sources. Indeed spectral index analyses performed using shallower ($S_{150\text{ MHz}} \geq 1$ mJy) LOFAR observations of the Boötes and LH fields, report overall median spectral index values of $\alpha_{150\text{ MHz}}^{1.4\text{ GHz}} = -0.73 \pm 0.33$ and -0.78 ± 0.24 , for AGN and star-forming galaxies respectively (Boötes; Calistro Rivera et al. 2017), as well as a flattening of the spectral index going to lower flux densities, with a median value of $\alpha_{150\text{ MHz}}^{1.4\text{ GHz}} = -0.7^{+0.02}_{-0.04}$ at $S_{150\text{ MHz}} \sim 1 - 2$ mJy (LH; Mahony et al. 2016).

As shown in Figure 5.3 the median sizes of both raw and final catalogues (respectively indicated by filled black-bordered magenta squares and golden circles with error bars) are compared with the Windhorst et al. (1990) size - flux relation converted to 150 MHz (long-dashed line). We see a discrepancy at intermediate fluxes (10 – 100 mJy), where the measured sizes appear in slight excess to what was predicted by Windhorst et al. (1990). We therefore decided to consider also the median size – flux relation derived from the Tiered Radio Extragalactic Continuum Simulation (T-RECS) catalogues at 150 MHz (Bonaldi et al. 2019, dot-dashed line), which implement different size – flux scaling relations for star-forming galaxies and AGN. This seems to better reproduce our measured sizes at fluxes $S_{150\text{ MHz}} \sim 10 - 100$ mJy, where extended radio galaxies (with typical sizes of hundreds of kpc) are expected to provide a significant contribution to the total radio source population. We caveat, however, that the afore-mentioned analysis is limited to flux densities $S_{150\text{ MHz}} \geq 2$ mJy, while the large majority of the sources in the LoTSS Deep Fields are fainter. Most of these sources cannot be reliably deconvolved, implying that no direct information on their size distribution can be obtained. Several attempts have been made to estimate the intrinsic source sizes at sub-mJy fluxes, based on deep samples carried out over a wide range of observing frequencies (from 330 MHz to 10 GHz). Some of these works have proposed a steepening of the Windhorst et al. (1990) median size - flux relation at sub-mJy fluxes, with $m = 0.4 - 0.5$ in the range 0.1 – 1 mJy (Richards 2000; Bondi et al. 2003, 2008; Smolčić et al. 2017). A smooth transition from a flatter to a steeper relation at sub-mJy fluxes could again be justified by a smooth transition from a flux regime dominated by extended radio galaxies ($S \gg 1$ mJy) to a flux regime dominated by radio sources triggered by

star-formation (or by composite SF/AGN emission), confined within the host galaxy.

In order to establish which size–flux relation would best quantify the incompleteness of our catalogues we have decided to include in our analysis the results from other deep surveys. Figure 5.4 shows the existing measurements of (median) source sizes in various flux bins for a number of surveys (different colors/symbols refer to different observing frequencies). Also shown are the median sizes derived by combining together the three LoTSS fields (raw and final catalogues, respectively indicated by filled black-bordered magenta squares and golden circles). To make the comparison meaningful, all fluxes referring to a different observing frequency have been converted to 1.4 GHz, assuming $\alpha = -0.7$. Also shown are various size – flux relations: the ones proposed by [Bonaldi et al. \(2019\)](#), converted to 1.4 GHz) and [Windhorst et al. \(1990\)](#) (dot-dashed and long-dashed lines respectively), and some modifications of the latter. The short dashed lines show the ones obtained by rescaling the [Windhorst et al. \(1990\)](#) relation by $1.5\times$ and $2\times$ (i.e. assuming $k=3$ and $k=4$ in Eq. 5.7), while the dotted line assumes a smooth transition between $m = 0.3$ and $m = 0.5$ going from mJy to sub-mJy flux densities, i.e.:

$$m = m(S) = 0.3 + 0.2 \times \exp(-S_{1.4\text{GHz}}^2) \quad (5.8)$$

with $S_{1.4\text{GHz}}$ expressed in mJy. Focusing on the sub-mJy regime, it is clear that both the [Windhorst et al. \(1990\)](#) and the steeper $m(S)$ relations are consistent with the observed sizes, especially when considering only the 1.4 GHz surveys (black filled triangles). Surveys undertaken at higher frequencies seem to point towards the steeper relation, but these samples may be biased towards a flatter spectrum population, resulting in an over-estimation of the flux densities once converted to 1.4 GHz assuming a too steep spectral index. We also caveat that higher frequency surveys more easily miss extended flux, and resolution bias issues can indeed mimic a steepening of source median sizes getting close to the flux limit of a radio survey. At larger flux densities ($S_{1.4\text{GHz}} \geq 1$ mJy) the median sizes are observed to lie between the [Windhorst et al. \(1990\)](#) relations described by $k = 2$ and $k = 4$, with a tendency for larger sizes going to lower frequency. Indeed some source counts’ analyses of shallower LOFAR surveys in the LH and Boo fields claimed in the past a better consistency with a $k = 4$ [Windhorst et al. \(1990\)](#) median size – flux scaling relation ([Mahony et al. 2016](#); [Retana-Montenegro et al. 2018](#)). It is interesting to note, however, that the LoTSS final catalogues are characterized by smaller median sizes than the raw catalogues at their faint end ($S_{1.4\text{GHz}} \leq 5$ mJy), indicating that confusion significantly affects the measured sizes of the faintest sources, and that a significant

number of faint sources were deblended. On the other hand, the final catalogues tend to be characterised by larger sizes at the bright end ($S_{1.4\text{GHz}} \geq 100$ mJy), likely as a consequence of the association of multiple components into single sources, after visual inspection of the radio/optical images (see Sect 5.3). After accounting for these effects, LoTSS median sizes (golden filled circles) are consistent with the Windhorst et al. (1990) $k = 2$ size – flux relation up to $S_{1.4\text{GHz}} \sim 2$ mJy. Then they smoothly increase and become consistent with the Bonaldi et al. (2019) relation at $S_{1.4\text{GHz}} \geq 10$ mJy. At $S_{1.4\text{GHz}} \geq 100$ mJy the LoTSS source median sizes show large uncertainties. At these large flux densities also the Bonaldi et al. (2019) relation is poorly determined, being based on a simulated catalogue covering a similar area to the one covered by the LOFAR deep fields (25 deg²). It is interesting to note, however, that both are consistent with the Windhorst et al. (1990) relation. Based on all the above considerations, a good description of the observed median sizes can be obtained by the following analytical form, which assumes the Windhorst et al. (1990) relation with a varying $k = k(S)$, i.e.:

$$k = \begin{cases} 3.5 - 1.5 \times \exp(-S_{1.4\text{GHz}}/2) & S_{1.4\text{GHz}} < 4.5 \\ 2 + 1.5 \times \exp(-S_{1.4\text{GHz}}/200) & S_{1.4\text{GHz}} \geq 4.5 \end{cases} \quad (5.9)$$

where $S_{1.4\text{GHz}}$ is expressed in mJy (see solid line in Fig. 5.4).

Another important consistency check regards the angular size distribution of the sources. Figure 5.5 shows the cumulative size distributions of the final catalogues combined together, in four flux density bins (yellow solid lines). Such distributions can be considered reliable only down to a flux-dependent minimum intrinsic size (see vertical grey lines), below which most of the sources cannot be reliably deconvolved and they are conventionally assigned $\Theta = 0$. The observed distributions are compared with various realizations of the cumulative distribution function described by Eq. 5.6, obtained by varying either the function exponent q (left and right columns respectively) or the assumed median size – flux relations (see various black lines). The original function proposed by Windhorst et al. (1990) (Eq. 5.6 with $q = 0.62$, see left column) does provide a good approximation of the observed distributions, when assuming the original $\Theta_{\text{med}} - S$ relation described by Eq. 5.7, only at fluxes $S_{150\text{MHz}} \geq 10$ mJy (see long-dashed lines). This is perhaps not surprising considering that this relation was calibrated at 1.4 GHz down to a few mJy fluxes. At the lowest flux densities ($S_{150\text{MHz}} \leq 1$ mJy) we need to assume a steepening of the parameter m (see Eq. 5.8), to get a good match with observations (dotted line in the top left panel). This is consistent with what proposed for higher frequency deep surveys

(as discussed earlier in this Section). At intermediate fluxes ($S_{150\text{MHz}} \sim 1 - 10$ mJy, on the other hand, none of the discussed median size – flux relations can reproduce the observed size distribution (see second-row panel on the left). It is interesting to note, however, that if we assume a steeper exponent for the distribution function described by Eq. 5.7 (i.e. $q = 0.80$), we get a very good match with observations at all fluxes, when assuming a flux-dependent scaling factor ($k = k(S)$; see Eq. 5.9) for the Windhorst et al. (1990) median size – flux relation (black solid lines on the right). The median sizes derived from the T-RECS simulated catalogues (Bonaldi et al. 2019) also provide good results for $q = 0.80$ (dot-dashed lines on the right), except again at intermediate fluxes ($S_{150\text{MHz}} \sim 1 - 10$), where they show strong discrepancies with observations also in Fig. 5.4. This seems to indicate that the number density of extended radio galaxies in this flux density range is over-estimated in the T-RECS simulated catalogues.

Correction for Resolution Bias

The correction factor c that needs to be applied to the source counts to account for the resolution bias can be defined as (Prandoni et al. 2001b):

$$c = 1/[1 - h(> \Theta_{\text{lim}})] \quad (5.10)$$

where $h(> \Theta_{\text{lim}})$ takes the form of the integral of the angular size distribution proposed by Windhorst et al. (1990, see Eq. 5.6), and Θ_{lim} is the limiting angular size above which the catalogues are expected to be incomplete. Following Prandoni et al. (2001b), this is defined as:

$$\Theta_{\text{lim}} = \max[\Theta_{\text{min}}, \Theta_{\text{max}}] \quad (5.11)$$

where Θ_{max} and Θ_{min} are as defined in Eqs. 5.4 and 5.5 respectively. We notice that Θ_{lim} is always equal to Θ_{max} , except for the lowest flux bins, where Θ_{max} becomes unphysical (i.e. tends to zero). Θ_{min} accounts for the effect of having a finite restoring beam size (that is $\Theta_{\text{lim}} > 0$ at the survey limit) and a deconvolution efficiency which varies with the source peak flux (see Prandoni et al. 2001b for more details).

Figure 5.6 (left panel) shows the correction factor derived assuming the median size – flux relations discussed above, combined with appropriate values of the q exponent in Eq. 5.6, based on our analysis of the source size distribution (see Fig. 5.5 and related discussion). A caveat to keep in mind is that the resolution bias correction does depend on both the source flux and the noise

value at the source position (and/or the source signal-to-noise ratio; see Eqs. 5.4 and 5.5). The corrections presented in Fig. 5.6 (left panel) account for local and radial variations of the noise through empirical relations between source flux and local noise or signal-to-noise ratio, specifically derived for each field. Such relations describe average trends only, and hence the corrections presented here should be considered as indicative. The corrections effectively applied to the counts are based on the actual source flux, noise and signal-to-noise ratio distributions. It is interesting to note, however, that, as a consequence of radially-increasing noise (and/or limited dynamic range around bright radio sources), the correction factor c does not necessarily converge to 1 at large flux densities. As shown in Fig. 5.6, in the masked regions of our fields this only happens when assuming the shallower integral distribution function ($q = 0.62$). For the steeper one ($q = 0.80$), the expected number density of very extended sources is small, and resolution bias effects become negligible at $S_{150\text{MHz}} \geq 500$ mJy.

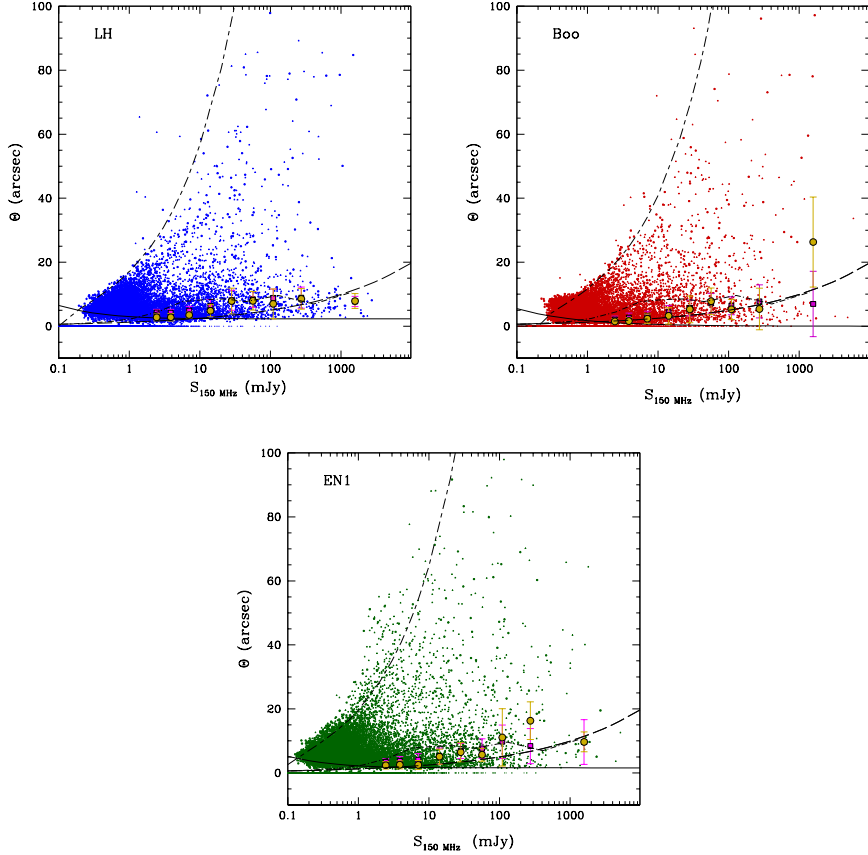


Figure 5.3: Source intrinsic (deconvolved) angular sizes as a function of the measured 150 MHz total flux densities. Deconvolved sizes are defined as the geometric mean of the major and minor FWHM axes, except for well resolved radio galaxies, which are better described by their major axis. Deconvolved sizes of point sources are set to zero. Raw (\cdot) and final (λ) catalogues of the LH, Boo and EN1 fields are shown in the top left, top right and bottom panels, respectively. The short-long-dashed lines in the three panels define the maximum size (Θ_{\max}) a source can have for a given measured total flux before dropping below the detection threshold. The solid lines give the minimum size (Θ_{\min}) below which deconvolution is not considered reliable. Both lines have been drawn assuming the median noise in the masked area (see last column of Table 5.1). The long-dashed lines indicate the Windhorst et al. (1990) median size - flux relation, converted to 150 MHz, while the dot-dashed lines indicate the median size - 150 MHz flux relation derived from the simulated T-RECS catalogues directly at 150 MHz (Bonaldi et al. 2019). The filled black-bordered magenta squares and golden circles with error bars represent the median source sizes for the raw and final catalogues respectively. Medians are computed only for those flux bins where unresolved sources represent less than 50% of the total number of sources.

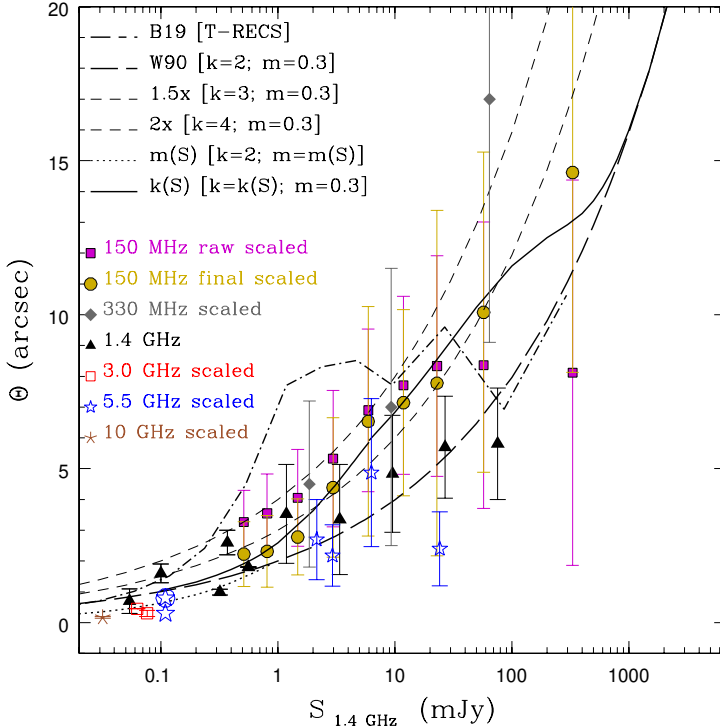


Figure 5.4: Source median angular size vs. 1.4 GHz total flux density, as estimated in some of the deepest radio samples available so far. Different colors/symbols correspond to different observing frequencies: 330 MHz (grey filled diamonds - Owen et al. 2009); 1.4 GHz (black filled triangles - Richards 2000; Bondi et al. 2003, 2008; Muxlow et al. 2005; Prandoni et al. 2018); 3 GHz (red empty squares - Bondi et al. 2018; Cotton et al. 2018); 5.5 GHz (blue stars - Prandoni et al. 2006; Guidetti et al. 2017); 10 GHz (brown asterisks - Murphy et al. 2017). Also shown are the median sizes measured in our raw and final catalogues (150 MHz), combined together (filled black-bordered magenta squares and golden circles). We note that Guidetti et al. (2017) gives different median sizes for the AGN and star-forming galaxy sub-populations. The latter population is indicated as a circled blue star in the figure. All fluxes have been converted to 1.4 GHz, assuming a spectral index $\alpha = -0.7$. Various median size – flux relations are shown for comparison: the ones proposed by Bonaldi et al. (2019) and Windhorst et al. (1990) (dot-dashed and long-dashed lines respectively), and some revised versions of the latter. The short dashed lines show the relations obtained by rescaling the Windhorst et al. (1990) relation by $1.5\times$ and $2\times$ (i.e. assuming $k = 3$ and $k = 4$ in Eq. 5.7); the dotted line assumes a smooth transition between $m = 0.3$ and $m = 0.5$ going from mJy to sub-mJy flux densities, as described by Eq. 5.8; the solid line assumes a value of k varying with flux density according to Eq. 5.9 (see text for more details).

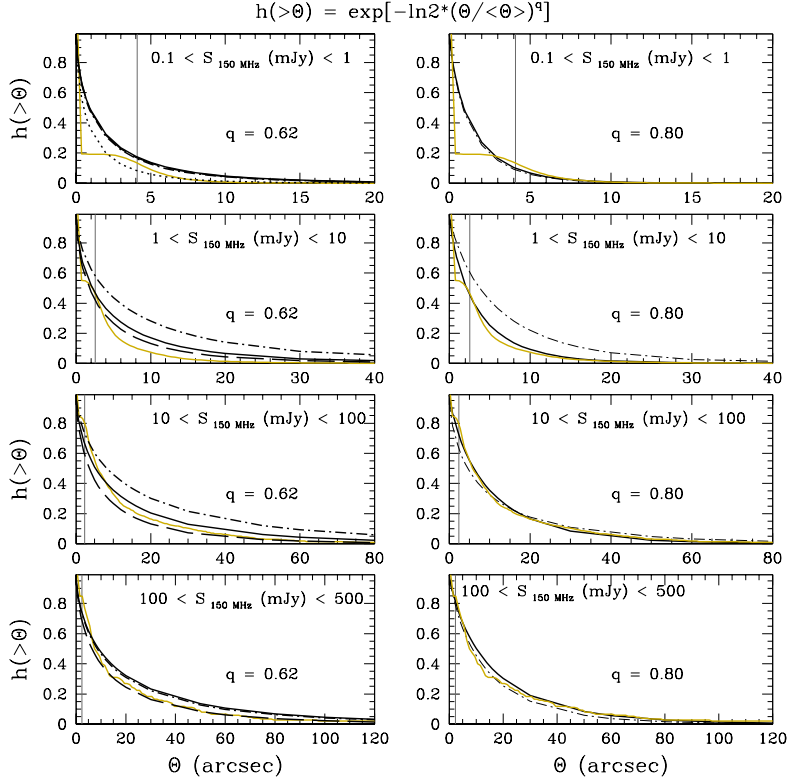


Figure 5.5: Source size cumulative distribution of final catalogues (yellow solid line) in four 150 MHz flux density bins. The vertical grey lines in all panels provides an approximate indication of the minimum intrinsic angular size to which the observed distributions can be considered reliable (most of the sources below this line cannot be reliably deconvolved and they are conventionally assigned $\Theta = 0$). Also shown for comparison are various realizations of the cumulative distribution function described by Eq. 5.6. The two columns correspond to two different values for the function exponent q : the original one proposed by Windhorst et al. (1990) ($q = 0.62$) on the left, and a steeper one ($q = 0.80$) on the right. In addition we also vary the median size – flux relation. In particular we assume the original Windhorst et al. (1990) relation (black long-dashed line), the revised versions with flux-dependent m and k parameters, as described by Eqs. 5.8 and 5.9 (black dotted and solid lines respectively) and the one describing the T-RECS catalogues (Bonaldi et al. 2019; black dot-dashed line). All such realizations are shown on the left; on the right we only show the realizations obtained using the Bonaldi et al. (2019) and the revised Windhorst et al. (1990) $k = k(S)$ relations.

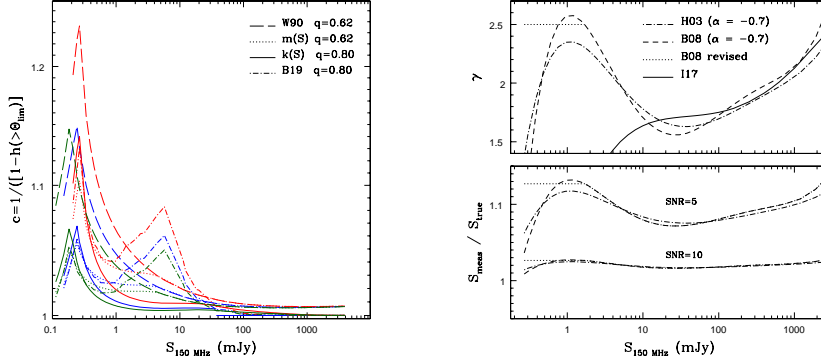


Figure 5.6: *Left*: Flux-dependent correction to be applied to source counts to account for incompleteness due to resolution bias, for four median size - flux relations: the one derived from the simulated T-RECS catalogues (Bonaldi et al. 2019; dot-dashed lines), the one proposed by Windhorst et al. (1990, long-dashed lines), the revised version with $m = m(S)$, which better describe source sizes at 1.4 GHz sub-mJy fluxes (see Eq. 5.8, dotted lines), and the revised version with $k = k(S)$ proposed by us (Eq. 5.9, solid lines). We also vary the q exponent of the integral distribution function. Based on our analysis of the source size distribution (see Fig. 5.5 and related discussion), we assume the original value proposed by Windhorst et al. (1990, $q = 0.62$) for the Windhorst et al. (1990) median size - flux relation and for the revised version with $m = m(S)$. We assume a steeper $q = 0.80$ for the revised version with $k = k(S)$ and for the Bonaldi et al. (2019) relation (see legenda). Different colors refer to different fields: LH (blue), Boo (red), EN1 (green). The corrections account for noise variations in the masked images through an empirical relation between source flux and source signal-to-noise ratio, calibrated for each field (we assume here the median noise of the masked images; see last column of Tab. 5.1). *Right*: Eddington bias for different underlying number-count distributions, as illustrated in the top panel: source counts' slope (γ ; $dN/dS \sim S^{-\gamma}$) derived from the sixth-order polynomial fit proposed at 1.4 GHz by a) Hopkins et al. (2003) (dot-dashed line) and b) Bondi et al. (2008) (dashed line), both converted to 150 MHz assuming a spectral index $\alpha = -0.7$; we also show a revised version of the Bondi et al. (2008) fit, which assumes a constant Euclidean slope ($\gamma = 2.5$) from 2 mJy all the way down to 0.1 mJy (dotted line). The polynomial fit proposed by Intema et al. (2017) at 150 MHz and valid only for the bright end of the counts is also shown for reference (solid line). The flux boosting ($S_{\text{meas}}/S_{\text{true}}$) corresponding to the three cases illustrated above is shown in the bottom panel for two different source signal-to-noise ratios: SNR=5 and SNR=10.

5.5 Eddington bias

While correcting for resolution bias is important to account for missed resolved sources, Eddington bias (Eddington 1913, 1940) should be taken into account to get an unbiased census of unresolved sources. Due to random measurement errors the measured peak flux densities will be redistributed around their true value. In presence of a source population which follows a non-uniform flux distribution, this will result in a redistribution of sources between number-count flux density bins. The way the sources are redistributed depends on the slope of source counts. If the source number density increases with decreasing flux, the fluxes tend to be boosted and the probability to detect a source below the detection threshold is higher than the probability to miss a source above the threshold, artificially boosting the detection fraction. As a consequence the catalogue incompleteness at the detection threshold is also biased.

There are two main approaches to correct for Eddington bias, both requiring an assumption about the true underlying source counts distribution (see Hales et al. 2014b for a full discussion): one can build the source counts using the boosted fluxes and then apply a correction to each flux bin, or one can correct the source fluxes, before deriving the counts. As demonstrated by Hales et al. (2014a) the two approaches give very similar and consistent results, and we decided to follow the latter approach. A maximum likelihood solution for the true source flux can be defined as follows (see Hales et al. 2014b and references therein):

$$S_{\text{true}} = \frac{S_{\text{meas}}}{2} \cdot \left(1 + \sqrt{1 - \frac{4\gamma}{\text{SNR}^2}} \right) \quad (5.12)$$

where $\gamma = \gamma(S)$ is the slope of the counts at the given flux density ($dN/dS \sim S^{-\gamma}$), and SNR is the source signal-to-noise ratio. The slope of the counts can be modeled from empirical polynomial fits of the observed counts:

$$\log \left(\frac{dN(S)}{dS} S^{2.5} \right) = \sum_{i=0}^n a_i (\log S)^i . \quad (5.13)$$

It is then easy to demonstrate that:

$$\gamma = 2.5 - \sum_{i=0}^n i \cdot a_i (\log S)^{i-1} . \quad (5.14)$$

In order to derive γ we can use one of the several counts' fits available in the literature. Intema et al. (2017) derived a fifth-order polynomial fit which describes

the 150 MHz normalized counts of the TIFR GMRT Sky Survey (TGSS), but this fit is only valid down to a flux limit of 5 mJy. The deepest fits available in the literature have been obtained at 1.4 GHz. We start by exploring the sixth-order ($n = 6$) polynomial fits obtained by Hopkins et al. (2003) and Bondi et al. (2008) for 1.4 GHz normalized source counts (converted to 150 MHz using $\alpha = -0.7^8$). The two cases are illustrated in the top right panel of Fig. 5.6 (dot-dashed and dashed lines respectively), where the derived counts' slope is shown. Both cases are consistent with the Intema et al. 150 MHz fit (indicated by the solid line) at bright flux densities ($S > 100$ mJy), while significant discrepancies are observed at fainter fluxes, where the deeper 1.4 GHz fits better describe the well-known flattening of the normalized counts. Both the 1.4 GHz fits show an increasing slope below 10 mJy, reaching a maximum around 1 mJy. This maximum is more pronounced in the case of Bondi et al. (2008), and is consistent with an Euclidean slope of $\gamma \sim 2.5$. At $S < 1$ mJy both slopes show a rapid drop. The reality and strength of this drop is unclear, as this is the flux regime where the fits are less reliably constrained. We then explore a third case, i.e. a modification of the Bondi et al. fit, which assumes a constant Euclidean slope at flux densities $S < 2$ mJy. This represents an extreme scenario, which however might be favoured by the recent 150 MHz source counts modeling proposed by Bonaldi et al. (2019), that indicates a flatter slope in the flux range 0.1 – 1 mJy. This last case is illustrated by the dotted line in Fig. 5.6 (top right panel). The flux boosting expected for the three aforementioned scenarios is illustrated in the bottom right panel of Fig. 5.6 for two signal-to-noise ratio values, SNR=5 and SNR=10.

Once the point source fluxes are corrected for Eddington bias, we can obtain an estimate of the catalogue incompleteness at the detection threshold through the use of Gaussian Error Functions (ERF).

⁸We caveat that assuming a single spectral index is a crude approximation. In principle we should account for the intrinsic scatter in the spectral index distribution of the sources, as well as for possible deviations of the mean spectral index with flux density, due to the varying relative contribution of the individual source populations. Such an approximation is however acceptable, since the largest uncertainties in this analysis come from the assumptions on the counts' slope at the faintest fluxes, which is very poorly known.

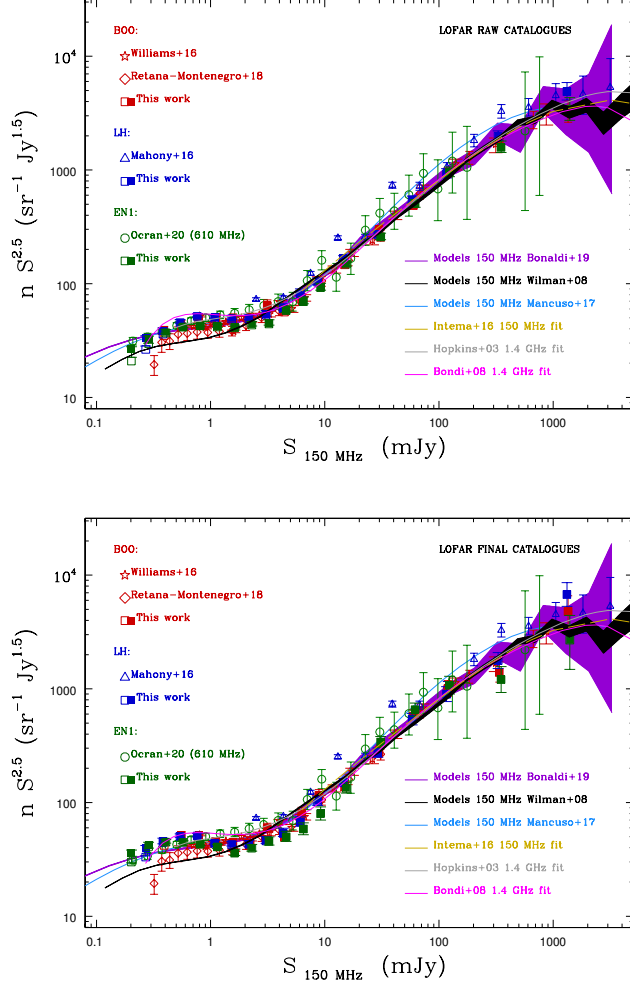


Figure 5.7: Normalized 150 MHz differential source counts in the three LoTSS Deep Fields, as derived from raw (*top*) and final (*bottom*) catalogues (filled squares). Error bars correspond to the quadratic sum of Poisson and systematic errors. Also shown are the counts obtained without applying the corrections discussed in Sects. 5.4 and 5.5 (empty squares). The counts are derived by using total flux densities for both point and extended sources. In both figures, Wilman et al. (2008), Bonaldi et al. (2019) and Mancuso et al. (2017) 150 MHz models are shown for comparison, as well as other existing 150 MHz counts’ determinations in the same fields (see legend). Since published 150 MHz counts are missing for EN1, we show a recent determination obtained at 610 MHz (Ocran et al. 2020) and rescaled to 150 MHz, assuming $\alpha = -0.7$. Also shown are the counts’ best fits discussed in Sect. 5.5.



Figure 5.8: Normalized 150 MHz differential source counts in the three LoTSS Deep Fields, as derived from final catalogues (filled squares), compared to counts derived from higher frequencies surveys (see legend), and rescaled to 150 MHz by assuming $\alpha = -0.7$. Error bars correspond to the quadratic sum of Poisson and systematic errors. Also shown are the Wilman et al. (2008), Bonaldi et al. (2019) and Mancuso et al. (2017) 150 MHz models and the counts' best fits discussed in Sect. 5.5. The counts are derived by using total flux densities for both point and extended sources.

Table 5.3: 150 MHz normalized differential radio-source counts as derived from combining the raw and final catalogues of the three LoTSS Deep Fields. $\langle S \rangle$ is the geometric mean of the respective flux density bin, expressed in mJy; $N(\text{raw})$ and $N(\text{final})$ indicates the normalized source counts obtained from the raw and final catalogues respectively (in $Jy^{1.5}sr^{-1}$); $\pm\sigma_{\text{tot}}$ are the total errors on the counts, estimated as the quadratic sum of Poissonian and systematic errors. We note that only EN1 and LH sources contribute to the first flux density bin.

$\langle S \rangle$	$N(\text{raw})^{+\sigma_{\text{tot}}}_{-\sigma_{\text{tot}}}$	$N(\text{final})^{+\sigma_{\text{tot}}}_{-\sigma_{\text{tot}}}$
0.20	$26.20^{+1.53}_{-4.26}$	$32.88^{+2.10}_{-6.56}$
0.29	$34.00^{+2.053}_{-7.124}$	$40.56^{+2.52}_{-7.98}$
0.41	$38.94^{+2.47}_{-2.64}$	$45.74^{+2.78}_{-2.29}$
0.57	$44.80^{+2.78}_{-1.42}$	$49.64^{+2.61}_{-1.11}$
0.81	$49.19^{+2.78}_{-1.44}$	$48.78^{+2.30}_{-0.96}$
1.15	$48.39^{+2.44}_{-2.05}$	$43.40^{+1.78}_{-1.25}$
1.62	$47.86^{+2.82}_{-2.92}$	$42.36^{+1.97}_{-1.84}$
2.29	$48.47^{+3.55}_{-3.58}$	$41.74^{+2.34}_{-2.36}$
3.24	$55.72^{+4.69}_{-5.32}$	$51.93^{+3.42}_{-3.72}$
4.59	$60.25^{+5.89}_{-5.88}$	$52.30^{+4.32}_{-4.16}$
6.49	$79.17^{+7.88}_{-8.14}$	$73.08^{+5.65}_{-6.59}$
9.17	$104.4^{+8.0}_{-8.4}$	$105.4^{+7.4}_{-7.2}$
15.4	$160.0^{+8.7}_{-8.2}$	$142.6^{+7.7}_{-7.3}$
30.9	$290.5^{+18.0}_{-17.0}$	$307.0^{+18.4}_{-17.4}$
61.7	$533.2^{+41.5}_{-38.6}$	$597.5^{+43.7}_{-40.8}$
123	$970.0^{+96.6}_{-87.9}$	$991.0^{+96.8}_{-88.4}$
349	1911^{+204}_{-185}	1660^{+190}_{-171}
1396	3915^{+890}_{-745}	4793^{+967}_{-822}

5.6 Differential source counts

The differential source counts, normalised to a non-evolving Euclidean model, obtained from the LoTSS Deep Fields are shown in Figure 5.7, together with other count determinations obtained in the same fields from previous low-frequency surveys (see legend). The top and bottom panels refer to counts derived from the raw and final catalogues, respectively (see filled boxes). The source counts obtained from the final catalogues are reported in tabular form in the Appendix (Tables 5.5, 5.6 and 5.7, for LH, Boo and EN1 fields respectively), and are also shown in Fig. 5.8, where they are compared to counts extrapolated from higher frequencies. In deriving the counts we applied a ‘fiducial’ model for the systematic corrections described in Sects. 5.4 and 5.5. Specifically we assumed the [Windhorst et al. \(1990\)](#) size – flux relation with $k = k(S)$ (Eq. 5.9), in combination with a ‘steep’ ($q = 0.80$ in Eq. 5.6) integral size distribution, to estimate the resolution bias, and we assumed the [Bondi et al. \(2008\)](#) source counts best fit to estimate the Eddington bias. The uncertainties associated with such assumptions are factored into systematic error terms (see Sys^- and Sys^+ columns in the counts’ tables), that are defined as the maximum discrepancy between the ‘fiducial’ counts and those obtained assuming the other discussed models (shown in Fig. 5.6). Also shown in Fig. 5.7 are the counts obtained from the three LoTSS fields before applying the corrections for resolution and Eddington bias (empty boxes). As expected such corrections are only relevant for the lowest flux density bins. We cut the source counts at a threshold of $\sim 7\sigma_{\text{med}}$, where systematic errors dominate over Poissonian (calculated following [Gehrels 1986](#)) by factors $\sim 5 - 10$.

The normalized 150 MHz source counts derived from the three LoTSS Deep Fields are in broad agreement with the counts obtained from previous low- and high- frequency radio surveys (see Figs. 5.7 and 5.8), and show the well known flattening at $S \leq \text{few mJy}$. However, when comparing the source counts derived from raw and final catalogues, we notice a very interesting feature: the latter show a much more pronounced drop at fluxes around a few mJy, which results in a more prominent ‘bump’ in the sub-mJy regime. For a more quantitative analysis of this feature we have combined the sources in the three fields and produced a combined version of the source counts. This allows us to smooth out field-to-field variations due to cosmic variance and/or residual systematics (like e.g. residual flux scaling issues, see Sect. 5.2), as well as reduce the scatter at bright fluxes, where Poissonian errors dominate. The combined counts derived from raw and final catalogues are shown in Fig. 5.9 and listed in Tab.5.3. We

Table 5.4: Coefficients for 7-th order polynomial function defined by Eq. 5.13, which best-fit the LoTSS and TGSS 150 MHz normalized source counts. The polynomial fit is shown in Figure 5.9.

Coefficient	Value	Error (\pm)
a_0	1.656	0.016
a_1	-0.0987	0.0632
a_2	0.2048	0.0877
a_3	0.52745	0.15986
a_4	-0.450223	0.166446
a_5	0.159674	0.078435
a_6	-0.028399	0.017124
a_7	0.002032	0.001416

notice that in this case we included LH and Boo sources down to a 5σ flux limit, to increase the statistics available in the first two flux density bins. From the comparison of the raw and final counts we see that the latter are systematically lower by a factor 7 – 14% in the range $S \sim 1 - 10$ mJy. This deficiency appears to be counterbalanced by a 10 – 20% excess at fluxes 0.2–0.6 mJy. This sort of compensation is consistent with being the result of source deblending, i.e. of the splitting of confused (brighter) sources into multiple fainter ones (see Sect. 5.3 and paper III for more details).

It is interesting to note that none of the previous counts’ determinations (neither at 150 MHz nor at higher frequency) show the pronounced ‘bump’ that we observe at 150 MHz sub-mJy fluxes. We have therefore decided to update the existing source counts best fits (shown in Figs. 5.7 and 5.8) with a new one that better matches the faint end of the 150 MHz counts derived from our final catalogues. The slope of the counts is modeled by a 7-th order polynomial function defined in the log-log space, according to Eq. 5.13 (see Sect. 5.5 for more details). To better constrain the bright end of the counts, where the LoTSS Deep Fields provide poor statistics, we have included the counts derived from the TGSS (Intema et al. 2017). The resulting coefficient values and their uncertainties are listed in Table 5.4; the fitted curve is shown in Fig. 5.9.

Qualitative comparison with models

The source counts derived from the LoTSS Deep Fields provide unprecedented observational constraints to the shape of the source counts at 150 MHz sub-mJy

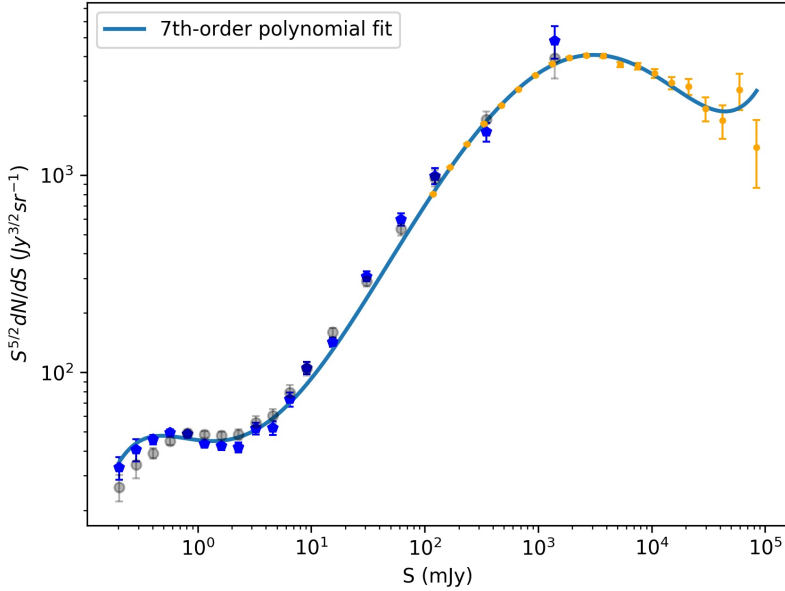


Figure 5.9: 150 MHz Euclidean normalized differential source counts as derived from the LoTSS Deep Fields: raw catalogue are indicated by transparent black circles and final catalogue by blue filled circles). Also shown are the counts obtained from the TGSS (Intema et al. 2017, orange filled circles), which better describe the counts’ bright end. Over-plotted is the best fit obtained by modeling the counts in the log-log space with a 7-th order polynomial function, according to Eq. 5.13 (see Table 5.4 for the values of the best-fit coefficients and associated errors).

fluxes. As such they can be compared with counts predictions based on existing evolutionary models of radio source populations. A comprehensive comparison with models is beyond the scope of this paper, and will be the subject of forthcoming papers, where counts and luminosity functions will be presented and discussed for various radio source populations. Here we only provide some first qualitative considerations.

In Figs. 5.7 and 5.8 we compare the LoTSS source counts to the 150 MHz determinations derived from the Wilman et al. (2008) and Bonaldi et al. (2019) simulated catalogues⁹ (black and dark violet shaded curves, respectively), as well as from Mancuso et al. (2017) models (light blue curve). We notice that the Bonaldi et al. (2019) and Wilman et al. (2008) source counts are very similar at the bright end and better reproduce the observations than Mancuso et al. (2017). On the other hand, Bonaldi et al. (2019) and Mancuso et al. (2017) counts are very similar at the faint end, and in better agreement with the observations than Wilman et al. (2008). Nevertheless, neither Bonaldi et al. (2019) nor Mancuso et al. (2017) can reproduce the pronounced bump at sub-mJy flux densities, observed in the counts derived from final catalogues (see Fig. 5.7, bottom panel, or Fig. 5.8). In addition all models appear to over-estimate the counts derived from our final catalogues at intermediate fluxes ($S \sim 2 - 20$ mJy).

In an attempt to better understand where the evolutionary models fail, we compare the observed source redshift distribution (using redshifts from paper IV) with those of the Bonaldi et al. (2019) simulated catalogue. We restrict this comparison to the EN1 field, as it is the deepest and has the most complete optical coverage among the three LoTSS Deep Fields.

In Fig. 5.10 we show the redshift distributions of the sources in the EN1 field (solid black lines) for various flux density bins. These distributions are compared with the simulated distributions based on Bonaldi et al. (2019) evolutionary models (blue histogram bars). We perform this analysis down to a flux limit of 0.25 mJy, i.e. down to a flux density where the effects of visibility function and incompleteness can be neglected. In the flux bins spanning from 0.25 to 0.75 mJy we see a clear deficiency of the simulated sources, in agreement with the observed excess in the counts. This deficiency is mainly associated with sources at $z < 1$. At larger fluxes ($S \geq 1$), on the other hand, we see an excess of simulated sources, which is also consistent with the deficiency observed in our counts in the range 2 – 20 mJy. This excess seems to be associated with either SFG or AGN at intermediate redshift ($1 < z < 2$).

⁹Bonaldi et al. (2019) present three simulated catalogues, each covering a different area of the sky. The one used here is the so-called *medium* tier, which covers a 25 deg² field of view, providing a very good match to the LoTSS Deep Fields. We use a new version of the catalogues originally presented in Bonaldi et al. (2019), which better reproduce the observations at the bottom and top of the covered frequency range (Bonaldi, private communication).

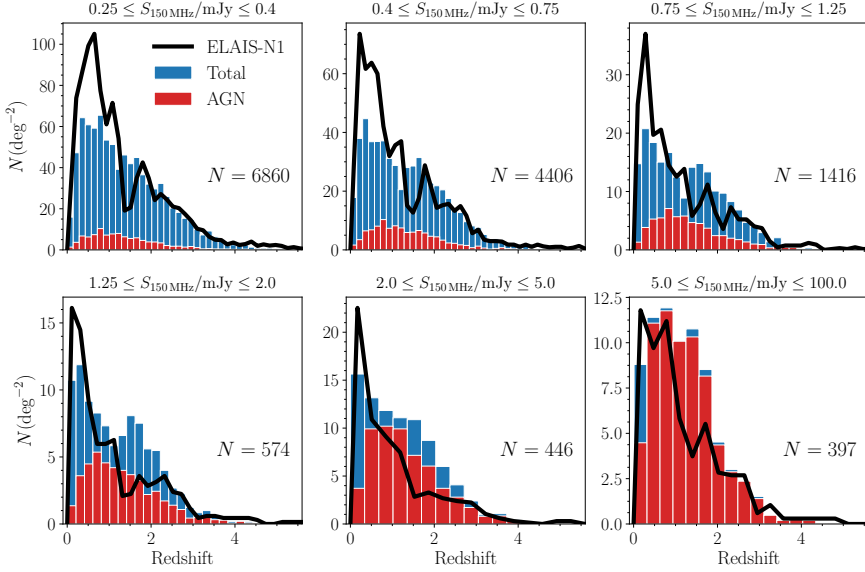


Figure 5.10: Redshift distribution of the simulated sources in [Bonaldi et al. \(2019\)](#) catalogue: the blue histogram corresponds to the total number of sources; the red histogram corresponds to the AGN component only. The solid black line shows the redshift distribution of the sources in the EN1 field. For a proper comparison the y-axis represents the source density in each catalogue. Each panel corresponds to a different flux density bin, increasing from left to right and from top to bottom.

5.7 Conclusions

In this paper, we have presented the source number counts derived from the LoTSS Deep Fields: the Lockman Hole (LH), the Boötes (Boo) and the Elais-N1 (EN1). With central rms noise levels of 22, 33, 17 $\mu\text{Jy beam}^{-1}$ the LH, Boo and EN1 fields are the deepest obtained so far at 150 MHz, allowing us to get unprecedented observational constraints to the shape of the source counts at 150 MHz sub-mJy fluxes. We compared the source counts derived from the LoTSS deep fields with other existing source-counts determinations from low-

and high- frequency radio surveys, and state-of-the-art evolutionary models. Our counts are in broad agreement with those from the literature, and show the well known upturn at \leq few mJy, which indicates the emergence of the star forming galaxy population. More interestingly, our counts show for the first time a very pronounced drop around $S \sim 2$ mJy, which results in a prominent ‘bump’ at sub-mJy fluxes. Such a pronounced ‘bump’ was not observed in previous counts’ determinations (neither at 150 MHz nor at higher frequency). We believe this is the result of a careful analysis aimed at deblending confused sources and removing spurious sources and artifacts from the radio source catalogues (see paper III). This ‘bump’ cannot be reproduced by any of the existing evolutionary models and appears to be associated with a low-redshift ($z < 1$) population of galaxies and/or AGN.

5.8 Acknowledgements

This paper is based (in part) on data obtained with the International LOFAR Telescope (ILT) under project code LC3_008. LOFAR (van Haarlem et al. 2013) is the Low Frequency Array designed and constructed by ASTRON. It has observing, data processing, and data storage facilities in several countries, that are owned by various parties (each with their own funding sources), and that are collectively operated by the ILT foundation under a joint scientific policy. The ILT resources have benefitted from the following recent major funding sources: CNRS-INSU, Observatoire de Paris and Université d’Orléans, France; BMBF, MIWF-NRW, MPG, Germany; Science Foundation Ireland (SFI), Department of Business, Enterprise and Innovation (DBEI), Ireland; NWO, The Netherlands; The Science and Technology Facilities Council, UK ; Istituto Nazionale di Astrofisica (INAF), Italy. This paper is based on the data obtained with the International LOFAR Telescope (ILT). The Leiden LOFAR team acknowledge support from the ERC Advanced Investigator programme NewClusters 321271 and the VIDI research programme with project number 639.042.729, which is financed by the Netherlands Organisation for Scientific Research (NWO). AD acknowledges support by the BMBF Verbundforschung under the grant 05A17STA. The Jülich LOFAR Long Term Archive and the German LOFAR network are both coordinated and operated by the Jülich Supercomputing Centre (JSC), and computing resources on the supercomputer JUWELS at JSC were provided by the Gauss Centre for supercomputing e.V. (grant CHTB00) through the John von Neumann Institute for Computing (NIC). TMS and DJS acknowledge the Research Training Group 1620 ‘Models of Gravity’, supported

by Deutsche Forschungsgemeinschaft (DFG) and support of the German Federal Ministry for Science and Research BMBF-Verbundforschungsprojekt D-LOFAR IV (grant number 05A17PBA). PNB is grateful for support from the UK STFC via grant ST/R000972/1. MJH acknowledges support from the UK Science and Technology Facilities Council (ST/R000905/1). IP and MB acknowledge support from INAF under PRIN SKA/CTA "FORECaST" and PRIN MAIN STREAM "SAuROS" projects, as well as from the Ministero degli Affari Esteri e della Cooperazione Internazionale - Direzione Generale per la Promozione del Sistema Paese Progetto di Grande Rilevanza ZA18GR02. JS is grateful for support from the UK STFC via grant ST/R000972/1. MJJ acknowledges support from the UK Science and Technology Facilities Council [ST/N000919/1] and the Oxford Hintze Centre for Astrophysical Surveys which is funded through generous support from the Hintze Family Charitable Foundation. RK acknowledges support from the Science and Technology Facilities Council (STFC) through an STFC studentship via grant ST/R504737/1. WLW acknowledges support from the ERC Advanced Investigator programme NewClusters 321271. WLW also acknowledges support from the CAS-NWO programme for radio astronomy with project number 629.001.024, which is financed by the Netherlands Organisation for Scientific Research (NWO). KLE acknowledges financial support from the Dutch Science Organization (NWO) through TOP grant 614.001.351. This research made use of APLpy, an open-source plotting package for Python hosted at <http://aplpy.github.com>.

5.A Appendix

Table 5.5: 150 MHz normalized differential radio-source counts as derived from the Lockman Hole field. S_{\min} and S_{\max} are the minimum and maximum flux densities (expressed in mJy), respectively. Δ denotes the flux density intervals. x is the geometric mean of S_{\min} and S_{\max} . N_S : Number of sources in respective bins. N is the normalized source counts and σ is the Poissonian errors on the normalized counts. Sys^+ and Sys^- are the systematic errors. N_c^{cor1} and N_c^{cor2} are the normalized counts with no systematic corrections applied and normalized counts with no systematic corrections and no visibility function applied, respectively. The tables for the Boötes and Elais-N1 fields are given in Table 5.6 and 5.7, respectively.

S_{\min}	S_{\max}	ΔS	x	N_S	$N_{-\sigma}^{+\sigma}$	Sys^-	Sys^+	N_c^{cor1}	N_c^{cor2}
0.23	0.32	0.09	0.27	5905	$39.51^{+0.48}_{-0.48}$	5.53	2.38	1.19	1.45
0.32	0.45	0.13	0.38	5463	$45.68^{+0.61}_{-0.61}$	2.18	2.74	1.02	1.12
0.45	0.64	0.19	0.54	4002	$50.25^{+0.80}_{-0.80}$	0.32	2.62	1.00	1.05
0.64	0.91	0.27	0.76	2447	$50.97^{+1.03}_{-1.03}$	0.04	2.26	1.01	1.03
0.91	1.29	0.38	1.08	1313	$44.16^{+1.25}_{-1.25}$	0.00	1.67	1.01	1.02
1.29	1.82	0.53	1.53	764	$43.01^{+1.61}_{-1.56}$	0.00	1.60	1.01	1.02
1.82	2.57	0.75	2.16	463	$43.31^{+2.11}_{-2.01}$	0.00	1.98	1.01	1.02
2.57	3.64	1.07	3.06	297	$46.50^{+2.86}_{-2.70}$	0.00	2.47	1.01	1.01
3.64	5.14	1.51	4.32	205	$54.06^{+4.04}_{-3.78}$	0.00	3.37	1.01	1.01
5.14	7.27	2.13	6.12	153	$67.62^{+5.91}_{-5.47}$	0.00	3.99	1.01	1.01
7.27	10.3	3.01	8.65	139	$103.2^{+9.5}_{-8.8}$	0.00	4.03	1.01	1.01
10.3	20.6	10.3	14.6	188	$150.0^{+11.7}_{-10.9}$	0.0	2.6	1.01	1.01
20.6	41.1	20.6	29.1	122	$275.3^{+27.2}_{-24.9}$	0.0	1.08	1.01	1.01
41.1	82.3	41.1	58.2	85	$541.5^{+65.1}_{-58.7}$	0.1	2.2	1.01	1.01
82.3	164	82.3	116.4	50	$900.5^{+145.4}_{-127.3}$	2.3	4.0	1.01	1.01
164	658	494	329	44	1776^{+308}_{-268}	2	11	1.00	1.00
658	2633	1975	1317	21	6791^{+1865}_{-1482}	24	91	1.01	1.01
2633	10530	7899	5266	1	2578^{+3929}_{-2139}	1	48	1.00	1.00

Table 5.6: Bootes 150 MHz source counts. See Table 5.5 for the caption

S_{\min}	S_{\max}	ΔS	x	N_S	$N_{+\sigma}$	S_{sys}^-	S_{sys}^+	$N_c^{\text{cor}1}$	$N_c^{\text{cor}2}$
0.33	0.47	0.13	0.39	3939	$44.57^{+0.70}_{-0.70}$	2.21	3.33	1.06	1.21
0.47	0.66	0.19	0.44	3251	$52.07^{+0.33}_{-0.33}$	0.40	3.42	1.01	1.08
0.55	0.93	0.27	0.78	2000	$51.25^{+0.97}_{-1.13}$	0.00	2.91	1.03	1.06
0.93	1.312	0.39	1.11	1088	$46.07^{+1.44}_{-1.40}$	0.04	2.20	1.02	1.04
1.32	1.87	0.55	1.59	651	$45.31^{+1.88}_{-1.78}$	0.00	2.47	1.02	1.02
1.87	2.64	0.77	2.22	373	$43.40^{+2.25}_{-2.25}$	0.00	2.91	1.02	1.02
2.64	3.73	1.09	3.14	263	$59.75^{+3.91}_{-3.69}$	0.00	4.43	1.01	1.18
3.73	5.27	1.54	4.43	152	$49.94^{+4.38}_{-4.05}$	0.00	4.30	1.01	1.02
5.27	7.46	2.18	6.27	147	$81.06^{+7.24}_{-6.69}$	0.00	6.78	1.01	1.02
7.46	10.55	3.09	8.87	126	$116.7^{+11.33}_{-10.4}$	0.00	6.50	1.01	1.01
10.55	21.09	10.55	14.91	140	$139.2^{+12.76}_{-11.77}$	0.00	3.29	1.01	1.01
21.09	42.18	21.09	29.83	100	$281^{+30.91}_{-28.10}$	0.0	1.30	1.02	1.01
42.18	84.36	42.18	59.65	73	$579.2^{+75.72}_{-67.79}$	0.58	2.83	1.01	1.01
84.36	168.7	84.36	119.3	45	$1010^{+173.1}_{-150.6}$	5.22	5.45	1.01	1.01
168.7	674.9	506.2	337.5	28	$1411^{+317.1}_{-298.7}$	3.57	11.34	1.01	1.01
674.9	2700	2025	1350	12	4798^{+1785}_{-1385}	9.21	47.8	1.00	1.00

Table 5.7: Elais-N1 150 MHz source counts. See Table 5.5 for the caption.

S_{\min}	S_{\max}	ΔS	x	N_S	$N_{-\sigma}^{+\sigma}$	Sys ⁻	Sys ⁺	N_c^{cor1}	N_c^{cor2}
0.17	0.24	0.07	0.20	6013	$36.13^{+0.43}_{-0.42}$	6.55	2.08	1.21	1.32
0.24	0.34	0.10	0.29	5399	$42.32^{+0.56}_{-0.55}$	2.48	2.33	1.03	1.08
0.34	0.48	0.14	0.40	3697	$45.04^{+0.74}_{-0.74}$	0.78	2.08	1.01	1.03
0.48	0.68	0.20	0.57	2257	$44.53^{+0.96}_{-0.94}$	0.10	1.76	1.00	1.01
0.68	0.96	0.28	0.81	1308	$43.04^{+1.22}_{-1.19}$	0.00	1.39	1.00	1.01
0.96	1.36	0.40	1.15	743	$40.88^{+1.55}_{-1.50}$	0.00	1.09	1.00	1.01
1.36	1.93	0.56	1.62	391	$36.04^{+1.92}_{-1.82}$	0.00	0.92	1.00	1.01
1.93	2.73	0.80	2.30	258	$39.93^{+2.64}_{-2.49}$	0.00	1.31	1.01	1.01
2.73	3.86	1.13	3.24	176	$45.78^{+3.71}_{-3.45}$	0.00	1.93	1.01	1.01
3.86	5.46	1.60	4.60	115	$50.28^{+5.12}_{-4.68}$	0.00	2.46	1.01	1.01
5.46	7.71	2.26	6.50	80	$58.72^{+7.30}_{-6.56}$	0.00	2.34	1.00	1.01
7.71	10.91	3.20	9.17	65	$80.12^{+11.17}_{-9.93}$	0.00	1.92	1.00	1.00
10.91	21.82	10.91	15.43	101	$134.5^{+14.72}_{-3.38}$	0.00	1.75	1.01	1.01
21.82	43.64	21.82	30.86	91	$340.7^{+39.46}_{-35.72}$	0.00	1.07	1.00	1.00
43.64	87.27	43.64	61.71	62	$657.2^{+94.06}_{-83.46}$	0.32	2.23	1.00	1.00
87.27	174.5	87.27	123.4	36	$1080^{+209.9}_{-179.9}$	2.55	4.10	1.00	1.00
174.5	698.2	523.6	349.1	18	$1214^{+353.7}_{-286.2}$	2.05	7.54	1.01	1.01
698.2	2793	2095.0	1396.0	5	$2689^{+1741.0}_{-1203}$	6.47	30.68	1.00	1.00

Bibliography

- Ackermann, M., Ajello, M., Albert, A., et al. 2014, *ApJ*, 787, 18
- Ackermann, M., Ajello, M., Albert, A., et al. 2016, *ApJ*, 819, 149
- Akamatsu, H. & Kawahara, H. 2013, *PASJ*, 65, 16
- Arnaud, K. A. 1996, in *Astronomical Society of the Pacific Conference Series*, Vol. 101, *Astronomical Data Analysis Software and Systems V*, ed. G. H. Jacoby & J. Barnes, 17
- Arnaud, M., Pointecouteau, E., & Pratt, G. W. 2005, *A&A*, 441, 893
- Asplund, M., Grevesse, N., Sauval, A. J., & Scott, P. 2009, *ARA&A*, 47, 481
- Bacchi, M., Feretti, L., Giovannini, G., & Govoni, F. 2003, *A&A*, 400, 465
- Baldi, A., Etori, S., Mazzotta, P., Tozzi, P., & Borgani, S. 2007, *ApJ*, 666, 835
- Baldwin, J. E., Boysen, R. C., Hales, S. E. G., et al. 1985, *MNRAS*, 217, 717
- Barrena, R., Girardi, M., & Boschin, W. 2013, *MNRAS*, 430, 3453
- Becker, R. H., White, R. L., & Helfand, D. J. 1995, *ApJ*, 450, 559
- Bell, A. R. 1978a, *MNRAS*, 182, 147
- Bell, A. R. 1978b, *MNRAS*, 182, 443

- Bennett, A. S. 1962, *MmRAS*, 68, 163
- Bennett, C. L., Banday, A. J., Gorski, K. M., et al. 1996, *ApJ*, 464, L1
- Bharadwaj, V., Reiprich, T. H., Schellenberger, G., et al. 2014, *A&A*, 572, A46
- Blumenthal, G. R., Faber, S. M., Primack, J. R., & Rees, M. J. 1984, *Nature*, 311, 517
- Bonafede, A., Brüggen, M., van Weeren, R., et al. 2012, *MNRAS*, 426, 40
- Bonafede, A., Govoni, F., Feretti, L., et al. 2011, *A&A*, 530, A24
- Bonafede, A., Intema, H. T., Brüggen, M., et al. 2014, *ApJ*, 785, 1
- Bonaldi, A., Bonato, M., Galluzzi, V., et al. 2019, *MNRAS*, 482, 2
- Bonato, M., Negrello, M., Mancuso, C., et al. 2017, *MNRAS*, 469, 1912
- Bonato, M., Prandoni, I., De Zotti, G., et al. 2020, *MNRAS*[[arXiv:2010.08748](https://arxiv.org/abs/2010.08748)]
- Bondi, M., Ciliegi, P., Schinnerer, E., et al. 2008, *ApJ*, 681, 1129
- Bondi, M., Ciliegi, P., Zamorani, G., et al. 2003, *A&A*, 403, 857
- Bondi, M., Zamorani, G., Ciliegi, P., et al. 2018, *A&A*, 618, L8
- Bonzini, M., Mainieri, V., Padovani, P., et al. 2015, *MNRAS*, 453, 1079
- Bonzini, M., Padovani, P., Mainieri, V., et al. 2013, *MNRAS*, 436, 3759
- Botteon, A., Brunetti, G., Ryu, D., & Roh, S. 2019, *arXiv e-prints*, [arXiv:1907.00966](https://arxiv.org/abs/1907.00966)
- Botteon, A., Gastaldello, F., & Brunetti, G. 2018a, *MNRAS*, 476, 5591
- Botteon, A., Gastaldello, F., Brunetti, G., & Dallacasa, D. 2016, *MNRAS*, 460, L84
- Botteon, A., Shimwell, T. W., Bonafede, A., et al. 2018b, *MNRAS*, 478, 885
- Bourdin, H., Mazzotta, P., Markevitch, M., Giacintucci, S., & Brunetti, G. 2013, *ApJ*, 764, 82
- Bridle, A. H., Fomalont, E. B., Miley, G. K., & Valentijn, E. A. 1979, *A&A*, 80, 201

- Brienza, M., Godfrey, L., Morganti, R., et al. 2017, *A&A*, 606, A98
- Brienza, M., Godfrey, L., Morganti, R., et al. 2016, *A&A*, 585, A29
- Brüggen, M., Rafferty, D., Bonafede, A., et al. 2018, *MNRAS*, 477, 3461
- Brüggen, M. & Vazza, F. 2020, *MNRAS*, 493, 2306
- Brunetti, G., Blasi, P., Reimer, O., et al. 2012, *MNRAS*, 426, 956
- Brunetti, G. & Jones, T. W. 2014, *International Journal of Modern Physics D*, 23, 1430007
- Brunetti, G. & Lazarian, A. 2007, *MNRAS*, 378, 245
- Brunetti, G. & Lazarian, A. 2011, *MNRAS*, 410, 127
- Brunetti, G. & Lazarian, A. 2016, *MNRAS*, 458, 2584
- Brunetti, G., Setti, G., Feretti, L., & Giovannini, G. 2001, *MNRAS*, 320, 365
- Brunetti, G., Zimmer, S., & Zandanel, F. 2017, *MNRAS*, 472, 1506
- Brunner, H., Cappelluti, N., Hasinger, G., et al. 2008, *A&A*, 479, 283
- Buote, D. A. & Tsai, J. C. 1996, *ApJ*, 458, 27
- Calistro Rivera, G., Williams, W. L., Hardcastle, M. J., et al. 2017, *MNRAS*, 469, 3468
- Cassano, R., Botteon, A., Di Gennaro, G., et al. 2019, *ApJ*, 881, L18
- Cassano, R., Brunetti, G., Norris, R. P., et al. 2012, *A&A*, 548, A100
- Cassano, R., Brunetti, G., Röttgering, H. J. A., & Brüggen, M. 2010, *A&A*, 509, A68
- Cassano, R., Brunetti, G., Venturi, T., et al. 2008, *A&A*, 480, 687
- Cassano, R., Etori, S., Brunetti, G., et al. 2013, *ApJ*, 777, 141
- Cavagnolo, K. W., Donahue, M., Voit, G. M., & Sun, M. 2009, *ApJS*, 182, 12
- Chambers, K. C., Magnier, E. A., Metcalfe, N., et al. 2016, arXiv e-prints, arXiv:1612.05560

- Chandra, P., Ray, A., & Bhatnagar, S. 2004, *ApJ*, 612, 974
- Clarke, T. E., Randall, S. W., Sarazin, C. L., Blanton, E. L., & Giacintucci, S. 2013, *ApJ*, 772, 84
- Cohen, A. S. & Clarke, T. E. 2011, *AJ*, 141, 149
- Cohen, A. S., Lane, W. M., Cotton, W. D., et al. 2007, *AJ*, 134, 1245
- Condon, J. J., Cotton, W. D., Fomalont, E. B., et al. 2012, *ApJ*, 758, 23
- Condon, J. J., Cotton, W. D., Greisen, E. W., et al. 1998, *AJ*, 115, 1693
- Coppejans, R., Cseh, D., Williams, W. L., van Velzen, S., & Falcke, H. 2015, *Monthly Notices of the Royal Astronomical Society*, 450, 1477
- Cotton, W. D., Condon, J. J., Kellermann, K. I., et al. 2018, *ApJ*, 856, 67
- Croft, S., van Breugel, W., Brown, M. J. I., et al. 2008, *The Astronomical Journal*, 135, 1793
- Cuciti, V., Brunetti, G., van Weeren, R., et al. 2018, *A&A*, 609, A61
- Cuciti, V., Cassano, R., Brunetti, G., et al. 2015, *A&A*, 580, A97
- de Gasperin, F., Dijkema, T. J., Drabent, A., et al. 2019, *A&A*, 622, A5
- de Gasperin, F., Dijkema, T.-J., Drabent, A., et al. 2018, *A&A*, this issue
- de Gasperin, F., Intema, H. T., & Frail, D. A. 2018, *MNRAS*, 474, 5008
- de Gasperin, F., Intema, H. T., Shimwell, T. W., et al. 2017, *Science Advances*, 3, e1701634
- de Gasperin, F., Ogrean, G. A., van Weeren, R. J., et al. 2015, *MNRAS*, 448, 2197
- de Gasperin, F., van Weeren, R. J., Brüggen, M., et al. 2014, *MNRAS*, 444, 3130
- de Vries, W. H., Morganti, R., Röttgering, H. J. A., et al. 2002, *The Astronomical Journal*, 123, 1784
- Delvecchio, I., Smolčić, V., Zamorani, G., et al. 2017, *A&A*, 602, A3

- Dennison, B. 1980, *ApJ*, 239, L93
- Di Gennaro, G., van Weeren, R. J., Hoeft, M., et al. 2018, *ApJ*, 865, 24
- Drabent, A., Hoeft, M., Mechev, A. P., et al. 2019, arXiv e-prints, arXiv:1910.13835
- Duchesne, S. W. & Johnston-Hollitt, M. 2019, *PASA*, 36, e016
- Durret, F., Lima Neto, G. B., & Forman, W. 2005, *A&A*, 432, 809
- Ebeling, H., Voges, W., Bohringer, H., et al. 1996, *MNRAS*, 283, 1103
- Eckert, D., Jauzac, M., Vazza, F., et al. 2016, *MNRAS*, 461, 1302
- Eddington, A. S. 1913, *MNRAS*, 73, 359
- Eddington, A. S., S. 1940, *MNRAS*, 100, 354
- Edge, D. O., Shakeshaft, J. R., McAdam, W. B., Baldwin, J. E., & Archer, S. 1959, *MmRAS*, 68, 37
- Eisenhardt, P. R., Stern, D., Brodwin, M., et al. 2004, *The Astrophysical Journal Supplement Series*, 154, 48
- English, W., Hardcastle, M. J., & Krause, M. G. H. 2019, *MNRAS*, 490, 5807
- Enßlin, T., Pfrommer, C., Miniati, F., & Subramanian, K. 2011, *A&A*, 527, A99
- Ensslin, T. A., Biermann, P. L., Klein, U., & Kohle, S. 1998, *A&A*, 332, 395
- Enßlin, T. A. & Brüggen, M. 2002, *MNRAS*, 331, 1011
- Enßlin, T. A. & Gopal-Krishna. 2001, *A&A*, 366, 26
- Enßlin, T. A. & Röttgering, H. 2002, *A&A*, 396, 83
- Feretti, L., Giovannini, G., Govoni, F., & Murgia, M. 2012, *A&A Rev.*, 20, 54
- Fermi, E. 1949, *Physical Review*, 75, 1169
- Finogonov, A. V., Vikhlinin, A. A., Gilfanov, M. R., et al. 1993, *Astronomy Letters*, 19, 435

- Finoguenov, A., Sarazin, C. L., Nakazawa, K., Wik, D. R., & Clarke, T. E. 2010, *ApJ*, 715, 1143
- Fixsen, D. J. 2009, *ApJ*, 707, 916
- Fotopoulou, S., Salvato, M., Hasinger, G., et al. 2012, *ApJS*, 198, 1
- Gehrels, N. 1986, *ApJ*, 303, 336
- Ghirardini, V., Eckert, D., Etti, S., et al. 2019, *A&A*, 621, A41
- Govoni, F., Markevitch, M., Vikhlinin, A., et al. 2004, *ApJ*, 605, 695
- Govoni, F., Orrù, E., Bonafede, A., et al. 2019, *Science*, 364, 981
- Gower, J. F. R., Scott, P. F., & Wills, D. 1967, *MmRAS*, 71, 49
- Green, D. A. & Joncas, G. 1994, *A&AS*, 104, 481
- Gregorini, L. & Prandoni, I. 2000, *Mem. Soc. Astron. Italiana*, 71, 895
- Gruppioni, C., Mignoli, M., & Zamorani, G. 1999, *MNRAS*, 304, 199
- Guidetti, D., Bondi, M., Prandoni, I., et al. 2017, *MNRAS*, 471, 210
- Guth, A. H. 1981, *Phys. Rev. D*, 23, 347
- Guth, A. H. & Steinhardt, P. J. 1984, *Scientific American*, 250, 116
- Hales, C. A., Norris, R. P., Gaensler, B. M., & Middelberg, E. 2014a, *MNRAS*, 440, 3113
- Hales, C. A., Norris, R. P., Gaensler, B. M., et al. 2014b, *MNRAS*, 441, 2555
- Hardcastle, M. J. 2018, *MNRAS*, 475, 2768
- Hardcastle, M. J., Croston, J. H., Shimwell, T. W., et al. 2019, *MNRAS*, 488, 3416
- Hardcastle, M. J., Gürkan, G., van Weeren, R. J., et al. 2016, *MNRAS*, 462, 1910
- Harris, D. E., Robertson, J. G., Dewdney, P. E., & Costain, C. H. 1982, *A&A*, 111, 299

- Hartley, P., Jackson, N., Sluse, D., Stacey, H. R., & Vives-Arias, H. 2019, *MNRAS*, 485, 3009
- Heald, G. H., Pizzo, R. F., Orrú, E., et al. 2015, *A&A*, 582, A123
- Herrera Ruiz, N., Middelberg, E., Deller, A., et al. 2017, *A&A*, 607, A132
- Herrera Ruiz, N., Middelberg, E., Norris, R. P., & Maini, A. 2016, *A&A*, 589, L2
- Heywood, I., Jarvis, M. J., & Condon, J. J. 2013, *Monthly Notices of the Royal Astronomical Society*, 432, 2625
- Hildebrandt, H., Choi, A., Heymans, C., et al. 2016, *MNRAS*, 463, 635
- Hoang, D. N., Shimwell, T. W., Stroe, A., et al. 2017, *MNRAS*, 471, 1107
- Hoekstra, H., Herbonnet, R., Muzzin, A., et al. 2015, *MNRAS*, 449, 685
- Hoekstra, H., Mahdavi, A., Babul, A., & Bildfell, C. 2012, *MNRAS*, 427, 1298
- Hopkins, A. M., Afonso, J., Chan, B., et al. 2003, *AJ*, 125, 465
- Hurley-Walker, N., Callingham, J. R., Hancock, P. J., et al. 2017, *MNRAS*, 464, 1146
- Huynh, M. T., Jackson, C. A., Norris, R. P., & Prandoni, I. 2005, *AJ*, 130, 1373
- Intema, H. T. 2014, *SPAM: Source Peeling and Atmospheric Modeling*
- Intema, H. T., Jagannathan, P., Mooley, K. P., & Frail, D. A. 2017, *A&A*, 598, A78
- Intema, H. T., van der Tol, S., Cotton, W. D., et al. 2009, *A&A*, 501, 1185
- Intema, H. T., van Weeren, R. J., Röttgering, H. J. A., & Lal, D. V. 2011, *Astronomy and Astrophysics*, 535, A38
- Ishwara-Chandra, C. H., Sirothia, S. K., Wadadekar, Y., Pal, S., & Windhorst, R. 2010, *MNRAS*, 405, 436
- Jannuzi, B. T. & Dey, A. 1999, in *Astronomical Society of the Pacific Conference Series*, Vol. 191, *Photometric Redshifts and the Detection of High Redshift Galaxies*, ed. R. Weymann, L. Storrie-Lombardi, M. Sawicki, & R. Brunner, 111

- Jeltema, T. E. & Profumo, S. 2011, *ApJ*, 728, 53
- Jones, T., O'Neill, B. J., Nolting, C., & Mendygral, P. J. 2017a, in *International Cosmic Ray Conference*, Vol. 301, 35th International Cosmic Ray Conference (ICRC2017), 276
- Jones, T. W., Nolting, C., O'Neill, B. J., & Mendygral, P. J. 2017b, *Physics of Plasmas*, 24, 041402
- Joshi, M. N., Kapahi, V. K., & Bagchi, J. 1986, *National Radio Astronomy Observatory Workshop*, 16, 73
- Juett, A. M., Sarazin, C. L., Clarke, T. E., et al. 2008, *ApJ*, 672, 138
- Kaiser, N. & Squires, G. 1993, *ApJ*, 404, 441
- Kalberla, P. M. W., Burton, W. B., Hartmann, D., et al. 2005, *A&A*, 440, 775
- Kale, R., Parekh, V., & Dwarakanath, K. S. 2018, *MNRAS*, 480, 5352
- Kale, R., Venturi, T., Giacintucci, S., et al. 2015, *A&A*, 579, A92
- Kang, H. & Ryu, D. 2015, *ApJ*, 809, 186
- Kang, H. & Ryu, D. 2016, *ApJ*, 823, 13
- Kang, H., Ryu, D., & Jones, T. W. 2012, *ApJ*, 756, 97
- Kempner, J. C., Blanton, E. L., Clarke, T. E., et al. 2004, in *The Riddle of Cooling Flows in Galaxies and Clusters of galaxies*, ed. T. Reiprich, J. Kempner, & N. Soker, 335
- Kempner, J. C. & Sarazin, C. L. 2001, *ApJ*, 548, 639
- Kenter, A., Murray, S. S., Forman, W. R., et al. 2005, *The Astrophysical Journal Supplement Series*, 161, 9
- Kierdorf, M., Beck, R., Hoefl, M., et al. 2017, *A&A*, 600, A18
- Komatsu, E., Smith, K. M., Dunkley, J., et al. 2011, *ApJS*, 192, 18
- Komissarov, S. S. & Gubanov, A. G. 1994, *A&A*, 285, 27
- Kovac, J. M., Leitch, E. M., Pryke, C., et al. 2002, *Nature*, 420, 772

- Kravtsov, A. V. & Borgani, S. 2012, *ARA&A*, 50, 353
- Krymskii, G. F. 1977, *Akademiia Nauk SSSR Doklady*, 234, 1306
- Lane, W. M., Cotton, W. D., Helmboldt, J. F., & Kassim, N. E. 2012, *Radio Science*, 47, RS0K04
- Lane, W. M., Cotton, W. D., van Velzen, S., et al. 2014, *MNRAS*, 440, 327
- Lawrence, A., Warren, S. J., Almaini, O., et al. 2007, *MNRAS*, 379, 1599
- Liu, A., Tozzi, P., Yu, H., De Grandi, S., & Ettori, S. 2018, *MNRAS*, 481, 361
- Lockman, F. J., Jahoda, K., & McCammon, D. 1986, *ApJ*, 302, 432
- Loi, F., Murgia, M., Govoni, F., et al. 2017, *MNRAS*, 472, 3605
- Lonsdale, C. J., Cappallo, R. J., Morales, M. F., et al. 2009, *IEEE Proceedings*, 97, 1497
- Lonsdale, C. J., Smith, H. E., Rowan-Robinson, M., et al. 2003, *PASP*, 115, 897
- Lovisari, L., Forman, W. R., Jones, C., et al. 2017, *ApJ*, 846, 51
- Mahdavi, A., Hoekstra, H., Babul, A., Balam, D. D., & Capak, P. L. 2007, *ApJ*, 668, 806
- Mahdavi, A., Hoekstra, H., Babul, A., et al. 2013, *ApJ*, 767, 116
- Mahony, E. K., Morganti, R., Prandoni, I., et al. 2016, *MNRAS*, 463, 2997
- Maini, A., Prandoni, I., Norris, R. P., Giovannini, G., & Spitler, L. R. 2016, *A&A*, 589, L3
- Mancuso, C., Lapi, A., Prandoni, I., et al. 2017, *ApJ*, 842, 95
- Mandal, S., Intema, H. T., Shimwell, T. W., et al. 2019, *A&A*, 622, A22
- Mandal, S., Intema, H. T., van Weeren, R. J., et al. 2020, *A&A*, 634, A4
- Markevitch, M., Gonzalez, A. H., David, L., et al. 2002, *ApJ*, 567, L27
- Markevitch, M. & Vikhlinin, A. 2007, *Phys. Rep.*, 443, 1
- Martin, D. C., Fanson, J., Schiminovich, D., et al. 2005, *ApJ*, 619, L1

- Mather, J. C., Cheng, E. S., Cottingham, D. A., et al. 1994, *ApJ*, 420, 439
- Mauch, T., Murphy, T., Buttery, H. J., et al. 2003, *MNRAS*, 342, 1117
- Mauduit, J.-C., Lacy, M., Farrah, D., et al. 2012, *PASP*, 124, 1135
- Maughan, B. J., Jones, C., Forman, W., & Van Speybroeck, L. 2008, *ApJS*, 174, 117
- Mechev, A. P., Plaat, A., Oonk, J. B. R., Intema, H. T., & Röttgering, H. J. A. 2018, *Astronomy and Computing*, 24, 117
- Mernier, F., Werner, N., Bagchi, J., et al. 2019, *MNRAS*, 486, 5430
- Miniati, F. & Beresnyak, A. 2015, *Nature*, 523, 59
- Mohan, N. & Rafferty, D. 2015, *PyBDSF: Python Blob Detection and Source Finder*, *Astrophysics Source Code Library*
- Murgia, M., Eckert, D., Govoni, F., et al. 2010, *A&A*, 514, A76
- Murgia, M., Govoni, F., Feretti, L., et al. 2004, *A&A*, 424, 429
- Murgia, M., Parma, P., Mack, K. H., et al. 2011, *A&A*, 526, A148
- Murphy, E. J., Momjian, E., Condon, J. J., et al. 2017, *ApJ*, 839, 35
- Murray, S. S., Kenter, A., Forman, W. R., et al. 2005, *The Astrophysical Journal Supplement Series*, 161, 1
- Muxlow, T. W. B., Richards, A. M. S., Garrington, S. T., et al. 2005, *MNRAS*, 358, 1159
- Muzzin, A., Wilson, G., Yee, H. K. C., et al. 2009, *ApJ*, 698, 1934
- Nolting, C., Jones, T. W., O'Neill, B. J., & Mendygral, P. J. 2019, *ApJ*, 876, 154
- Nuza, S. E., Gelszinnis, J., Hoeft, M., & Yepes, G. 2017, *MNRAS*, 470, 240
- Nuza, S. E., Hoeft, M., van Weeren, R. J., Gottlöber, S., & Yepes, G. 2012, *MNRAS*, 420, 2006
- Ocran, E. F., Taylor, A. R., Vaccari, M., & Green, D. A. 2017, *MNRAS*, 468, 1156

- Ocran, E. F., Taylor, A. R., Vaccari, M., Ishwara-Chandra, C. H., & Prandoni, I. 2020, *MNRAS*, 491, 1127
- Offringa, A. R., McKinley, B., Hurley-Walker, N., et al. 2014, *MNRAS*, 444, 606
- Offringa, A. R. & Smirnov, O. 2017, *MNRAS*, 471, 301
- Offringa, A. R., van de Gronde, J. J., & Roerdink, J. B. T. M. 2012, *A&A*, 539, A95
- Ogrean, G. A., Brüggem, M., van Weeren, R., et al. 2011, *MNRAS*, 414, 1175
- Oliver, S. J., Bock, J., Altieri, B., et al. 2012, *MNRAS*, 424, 1614
- O'Neill, B. J., Jones, T. W., Nolting, C., & Mendygral, P. J. 2019, *ApJ*, 887, 26
- Owen, F. N., Morrison, G. E., Klimek, M. D., & Greisen, E. W. 2009, *AJ*, 137, 4846
- Padovani, P., Bonzini, M., Kellermann, K. I., et al. 2015, *MNRAS*, 452, 1263
- Padovani, P., Miller, N., Kellermann, K. I., et al. 2011, *ApJ*, 740, 20
- Parma, P., Murgia, M., de Ruiter, H. R., et al. 2007, *A&A*, 470, 875
- Pearson, T. J. & Readhead, A. C. S. 1984, *ARA&A*, 22, 97
- Perley, R. A. & Butler, B. J. 2013, *ApJS*, 204, 19
- Petrosian, V. 2001, *ApJ*, 557, 560
- Piffaretti, R., Arnaud, M., Pratt, G. W., Pointecouteau, E., & Melin, J. B. 2011, *A&A*, 534, A109
- Pilkington, J. D. H. & Scott, J. F. 1965, *MNRAS*, 69, 183
- Pinzke, A., Oh, S. P., & Pfrommer, C. 2013, *MNRAS*, 435, 1061
- Pinzke, A., Oh, S. P., & Pfrommer, C. 2017, *MNRAS*, 465, 4800
- Planck Collaboration, Ade, P. A. R., Aghanim, N., et al. 2016, *A&A*, 594, A27
- Polletta, M. d. C., Wilkes, B. J., Siana, B., et al. 2006, *ApJ*, 642, 673
- Prandoni, I., Gregorini, L., Parma, P., et al. 2001a, arXiv e-prints, astro

- Prandoni, I., Gregorini, L., Parma, P., et al. 2000a, *A&AS*, 146, 31
- Prandoni, I., Gregorini, L., Parma, P., et al. 2000b, *A&AS*, 146, 41
- Prandoni, I., Gregorini, L., Parma, P., et al. 2001b, *A&A*, 365, 392
- Prandoni, I., Guglielmino, G., Morganti, R., et al. 2018, *MNRAS*, 481, 4548
- Prandoni, I., Parma, P., Wieringa, M. H., et al. 2006, *A&A*, 457, 517
- Rajpurohit, K., Hoeft, M., van Weeren, R. J., et al. 2018, *ApJ*, 852, 65
- Rajpurohit, K., Hoeft, M., Vazza, F., et al. 2020, *A&A*, 636, A30
- Randall, S. W., Clarke, T. E., Nulsen, P. E. J., et al. 2010, *ApJ*, 722, 825
- Randriamanakoto, Z., Ishwara-Chandra, C. H., & Taylor, A. R. 2020, *MNRAS*, 496, 3381
- Rau, U. & Cornwell, T. J. 2011, *A&A*, 532, A71
- Rengelink, R. B., Tang, Y., de Bruyn, A. G., et al. 1997, *A&AS*, 124, 259
- Retana-Montenegro, E., Röttgering, H. J. A., Shimwell, T. W., et al. 2018, *A&A*, 620, A74
- Richards, E. A. 2000, *ApJ*, 533, 611
- Riess, A. G., Filippenko, A. V., Challis, P., et al. 1998, *AJ*, 116, 1009
- Roettiger, K., Burns, J. O., & Loken, C. 1996, *ApJ*, 473, 651
- Roettiger, K., Burns, J. O., & Stone, J. M. 1999, *ApJ*, 518, 603
- Roettiger, K., Loken, C., & Burns, J. O. 1997, *ApJS*, 109, 307
- Roland, J., Hanisch, R. J., Veron, P., & Fomalont, E. 1985, *A&A*, 148, 323
- Röttgering, H., Afonso, J., Barthel, P., et al. 2011, *Journal of Astrophysics and Astronomy*, 32, 557
- Röttgering, H. J. A., Braun, R., Barthel, P. D., et al. 2006, *ArXiv Astrophysics e-prints* [[astro-ph/0610596](https://arxiv.org/abs/astro-ph/0610596)]
- Sarazin, C. 2013, PKS B1400-33 and Abell S753: A Very Bright Radio Relic in a Poor Cluster, XMM-Newton Proposal

- Sarazin, C. L. 1999, *ApJ*, 520, 529
- Scaife, A. M. M. & Heald, G. H. 2012, *MNRAS*, 423, L30
- Schilizzi, R. T. 2005, in *EAS Publications Series*, Vol. 15, *EAS Publications Series*, ed. L. I. Gurvits, S. Frey, & S. Rawlings, 445–463
- Schinnerer, E., Carilli, C. L., Scoville, N. Z., et al. 2004, *AJ*, 128, 1974
- Schinnerer, E., Smolčić, V., Carilli, C. L., et al. 2007, *ApJS*, 172, 46
- Shimwell, T. W., Luckin, J., Brügger, M., et al. 2016, *MNRAS*, 459, 277
- Shimwell, T. W., Markevitch, M., Brown, S., et al. 2015, *MNRAS*, 449, 1486
- Shimwell, T. W., Röttgering, H. J. A., Best, P. N., et al. 2017, *A&A*, 598, A104
- Shimwell, T. W., Tasse, C., Hardcastle, M. J., et al. 2019, *Astronomy and Astrophysics*, 622, A1
- Shulevski, A., Morganti, R., Barthel, P. D., et al. 2015, *A&A*, 583, A89
- Shulevski, A., Morganti, R., Harwood, J. J., et al. 2017, *A&A*, 600, A65
- Sifón, C., Hoekstra, H., Cacciato, M., et al. 2015, *A&A*, 575, A48
- Simard, L., Clowe, D., Desai, V., et al. 2009, *A&A*, 508, 1141
- Sirothia, S. K., Saikia, D. J., Ishwara-Chandra, C. H., & Kantharia, N. G. 2009, *MNRAS*, 392, 1403
- Slee, O. B., Roy, A. L., Murgia, M., Andernach, H., & Ehle, M. 2001, *AJ*, 122, 1172
- Smirnov, O. M. & Tasse, C. 2015, *MNRAS*, 449, 2668
- Smolčić, V., Novak, M., Bondi, M., et al. 2017, *A&A*, 602, A1
- Smolčić, V., Schinnerer, E., Scodreggio, M., et al. 2008, *ApJS*, 177, 14
- Smoot, G. F., Bennett, C. L., Kogut, A., et al. 1992, *ApJ*, 396, L1
- Springel, V., Frenk, C. S., & White, S. D. M. 2006, *Nature*, 440, 1137
- Stroe, A., Shimwell, T., Rumsey, C., et al. 2016, *MNRAS*, 455, 2402

- Stroe, A., van Weeren, R. J., Intema, H. T., et al. 2013, *A&A*, 555, A110
- Struble, M. F. & Rood, H. J. 1999, *ApJS*, 125, 35
- Subrahmanyan, R., Beasley, A. J., Goss, W. M., Golap, K., & Hunstead, R. W. 2003, *AJ*, 125, 1095
- Swarup, G., Ananthakrishnan, S., Kapahi, V. K., et al. 1991, *Current Science*, 60, 95
- Tasse, C. 2014, arXiv e-prints [arXiv:1410.8706]
- Tasse, C., Hugo, B., Mirmont, M., et al. 2018, *A&A*, 611, A87
- Trott, C. M. & Wayth, R. B. 2016, *PASA*, 33, e019
- Tümer, A., Tombesi, F., Bourdin, H., et al. 2019, *A&A*, 629, A82
- Ulmer, M. P., Kowalski, M. P., Cruddace, R. G., et al. 1981, *ApJ*, 243, 681
- Urdampilleta, I., Akamatsu, H., Mernier, F., et al. 2018, *A&A*, 618, A74
- Vacca, V., Murgia, M., Govoni, F., et al. 2012, *A&A*, 540, A38
- van Haarlem, M. P., Wise, M. W., Gunst, A. W., et al. 2013, *A&A*, 556, A2
- van Weeren, R. J., Andrade-Santos, F., Dawson, W. A., et al. 2017, *Nature Astronomy*, 1, 0005
- van Weeren, R. J., Brunetti, G., Brüggén, M., et al. 2016a, *ApJ*, 818, 204
- van Weeren, R. J., de Gasperin, F., Akamatsu, H., et al. 2019, *Space Sci. Rev.*, 215, 16
- van Weeren, R. J., Röttgering, H. J. A., & Brüggén, M. 2011, *A&A*, 527, A114
- van Weeren, R. J., Röttgering, H. J. A., Brüggén, M., & Cohen, A. 2009, *A&A*, 508, 75
- van Weeren, R. J., Röttgering, H. J. A., Brüggén, M., & Hoeft, M. 2010, *Science*, 330, 347
- van Weeren, R. J., Röttgering, H. J. A., Intema, H. T., et al. 2012a, *A&A*, 546, A124

- van Weeren, R. J., Röttgering, H. J. A., Rafferty, D. A., et al. 2012b, *A&A*, 543, A43
- van Weeren, R. J., Williams, W. L., Hardcastle, M. J., et al. 2016b, *ApJS*, 223, 2
- Vantyghem, A. N., McNamara, B. R., Russell, H. R., et al. 2014, *MNRAS*, 442, 3192
- Vazza, F., Brüggem, M., Gheller, C., & Wang, P. 2014, *MNRAS*, 445, 3706
- Vazza, F., Brüggem, M., van Weeren, R., et al. 2012, *MNRAS*, 421, 1868
- Vazza, F., Eckert, D., Brüggem, M., & Huber, B. 2015, *MNRAS*, 451, 2198
- Voges, W., Aschenbach, B., Boller, T., et al. 1999, *A&A*, 349, 389
- Wayth, R. B., Lenc, E., Bell, M. E., et al. 2015, *PASA*, 32, e025
- Wen, Z. L., Han, J. L., & Liu, F. S. 2012, *ApJS*, 199, 34
- Werner, N., Zhuravleva, I., Canning, R. E. A., et al. 2016, *MNRAS*, 460, 2752
- White, R. L., Becker, R. H., Helfand, D. J., & Gregg, M. D. 1997, *ApJ*, 475, 479
- White, S. V., Jarvis, M. J., Häußler, B., & Maddox, N. 2015, *MNRAS*, 448, 2665
- White, S. V., Jarvis, M. J., Kalfountzou, E., et al. 2017, *MNRAS*, 468, 217
- Wilber, A., Brüggem, M., Bonafede, A., et al. 2018, *MNRAS*, 473, 3536
- Williams, W. L., Intema, H. T., & Röttgering, H. J. A. 2013, *Astronomy and Astrophysics*, 549, A55
- Williams, W. L., van Weeren, R. J., Röttgering, H. J. A., et al. 2016, *MNRAS*, 460, 2385
- Wilman, R. J., Miller, L., Jarvis, M. J., et al. 2008, *MNRAS*, 388, 1335
- Windhorst, R., Mathis, D., & Neuschaef, L. 1990, in *Astronomical Society of the Pacific Conference Series*, Vol. 10, *Evolution of the Universe of Galaxies*, ed. R. G. Kron, 389–403

Wittor, D., Vazza, F., & Brüggen, M. 2017, *MNRAS*, 464, 4448

Wright, E. L. 2006, *PASP*, 118, 1711

Yang, X., Mo, H. J., van den Bosch, F. C., et al. 2007, *ApJ*, 671, 153

Yatawatta, S., de Bruyn, A. G., Brentjens, M. A., et al. 2013, *A&A*, 550, A136

Zandanel, F. & Ando, S. 2014, *MNRAS*, 440, 663

Nederlandse samenvattig

De oerknaltheorie suggereert dat ons universum ongeveer 13,7 miljard jaar geleden begon in een begintoestand van zeer hoge temperatuur en dichtheid. De geschiedenis van de vorming van het heelal is al sinds de oudheid een onderwerp van discussie en heeft in de afgelopen decennia veel belangstelling gekregen vanwege de verbeteringen van de astronomische gegevens en technologische vooruitgangen. Op grote schaal is ons huidige universum opmerkelijk homogeen en isotroop. Studies tonen echter aan dat kleine variaties in de temperatuur van de kosmische achtergrondstraling (CMB) uiteindelijk leiden tot kleinschalige variaties in dichtheid. Onder invloed van de zwaartekracht groeiden deze kleinschalige schommelingen in dichtheid hiërarchisch en vormden ze wolken van gas, sterren, sterrenstelsels en uiteindelijk de grootste (massa's tot 10^{15} zonsmassa's) gravitationeel gebonden structuren: clusters van sterrenstelsels. Ongeveer 80% van de massa van clusters bestaat uit donkere materie en de rest uit baryonische materie. De enige interactie tussen donkere materie en baryonische materie is door middel van zwaartekracht.

Clusters van sterrenstelsels groeien door het aantrekken van kleinere groepen sterrenstelsels en door grote botsingen met andere clusters. Deze botsingen kunnen een enorme hoeveelheid gravitationele energie vrijgeven die kan worden verspreid door schokgolven en turbulentie die het intra-cluster medium (ICM) kunnen opwarmen. Direct bewijs van dergelijke gebeurtenissen kan worden gevonden door middel van röntgen waarnemingen van clusters van sterrenstelsels. Bovendien kunnen schokken en turbulentie ook de magnetische velden versterken en het ruimtelijk transport van de relativistische deeltjes (die ook bek-

end staan als kosmische straling, CR: cosmic rays in het engels.) beïnvloeden. Onder invloed van magnetische velden kunnen deze relativistische geladen deeltjes synchrotronstraling uitzenden die we kunnen waarnemen op radiogolflengten. Deze radiostraling heeft typisch een steile 'spectrale index', wat betekent dat het helderder is op lagere frequenties en zwakker op hoge frequenties. De aanwezigheid van CR-elektronen en magnetische velden in het ICM die via synchrotronstraling grote diffuse radiobronnen genereren, heeft fundamentele implicaties voor zowel de fysica van het ICM als de evolutie van de grootschalige structuur van het heelal.

In de afgelopen decennia is er aanzienlijke vooruitgang geboekt met het classificeren van diffuse radiobronnen in de ICM. Op basis van de morfologie en fysische eigenschappen kunnen deze bronnen grofweg worden onderverdeeld in twee categorieën: radio halo's en radio-relikwieën. Beide soorten bronnen hebben geen duidelijke optische tegenhangers (sterrenstelsels). Radio halo's zijn diffuse radiobronnen op Mpc-schaal, die zich doorgaans in het centrum van botsende clusters bevinden en de vorm van de röntgenstraling van het systeem volgen. Waarnemingen van radio halo's suggereren dat deze bronnen hoogstwaarschijnlijk worden gecreëerd door het continu opnieuw versnellen van CR-elektronen in het turbulente gas. Daarentegen worden radio-relikwieën meestal gevonden aan de rand van botsende clusters en hebben ze een convexe vorm ten opzichte van het centrum van de cluster. Aangenomen wordt dat radio-relikwieën de door de botsingen veroorzaakte schokgolven traceren. In de eerste plaats wordt gedacht dat schokken deeltjes versnellen via een mechanisme dat diffuse schok versnelling (DSA) wordt genoemd. De efficiëntie van dit mechanisme blijkt echter erg laag en onvoldoende te zijn om heldere radio-relikwieën te creëren, zoals gevonden in recente waarnemingen. Om deze reden is de aanwezigheid van reeds bestaande relativistische deeltjes (ook bekend als 'zaad-deeltjes' of 'fossiel plasma') voorgesteld, aangezien simulaties aangeven dat versnelling van zaad-deeltjes efficiënter is dan de DSA. Een soortgelijk scenario is ook voorgesteld voor het genereren van radio halo's die het bestaan van licht relativistische zaad-elektronen vereisen. In dit opzicht is een van de belangrijkste vragen die beantwoord moet worden de bron van deze fossiele elektronen in het ICM.

Het is inmiddels bekend dat clusters van sterrenstelsels actieve galactische kernen (AGN's) herbergen die CR-elektronen in het ICM injecteren en in de aanwezigheid van magnetische velden radiostraling kunnen genereren. Dergelijke AGN's staan bekend als radiostelsels en gaan vaak gepaard met enkele of dubbele radiolobben die zich tot zeer grote schaal kunnen uitstrekken. Deze energetische CR-elektronen uit de lobben van radiostelsels zijn belangrijke kandidaten die een zaad-populatie van relativistisch fossiel plasma kunnen leveren.

Wanneer de centrale AGN van een radiostelsel uitschakelt, is er geen toevoer van energetische elektronen naar de lobben en kunnen deze ‘AGN-restlobben’ zich uitspreiden in het omringende medium. Door verschillende processen (zoals synchrotron en stralingsverliezen) wordt hun spectrum pas na enkele tientallen miljoenen jaren steiler en worden ze zeer moeilijk te detecteren, zelfs op de laagst waarneembare frequenties. Daarom is het bestuderen van deze fossiele plasmapronen in clusters niet triviaal. Door botsingen aangedreven turbulentie, schokgolven en bulkstromen van het omringende medium kunnen deze fossiele elektronen echter opnieuw activeren en waarneembare radiogolven uitzenden. Deze bronnen van ‘nieuw leven ingeblazen fossiel plasma’ (die ook bekend staan als **radio feniksen**) bieden ons dus een unieke kans om deze anders onzichtbare populatie elektronen te bestuderen. Tot op heden zijn er maar heel weinig radio feniksen ontdekt. Om de onderliggende versnellingsmechanismen van deeltjes te begrijpen en of er een verband bestaat tussen radiostelsels en versnellingsmechanismen in radio halo’s en relikwieën, is het essentieel om systematisch hun gemeenschappelijke fysische eigenschappen te identificeren en ze te vergelijken met die van radio halo’s en relikwieën.

Laagfrequente radiosurveys van de hele hemel zijn uitstekend om deze studies systematisch uit te voeren. Kalibratie van laagfrequente radio data is echter altijd een uitdaging geweest vanwege de richtingsafhankelijke, tijd-variërende effecten van de ionosfeer. De ionosferische effecten zijn veel ernstiger voor het laagste frequentie deel van het radiospectrum, waardoor het een van de belangrijkste beperkende factoren is voor hoge resolutie laagfrequente radiowaarnemingen. Bovendien is het blikveld bij deze lage frequenties veel groter dan bij hoge frequenties. Daarom is het gebruik van traditionele technieken en het toepassen van een enkele correctiefactor om ionosferische effecten in het gehele blikveld te corrigeren te simplistisch en niet voldoende.

Zeer recent, met de komst van een nieuwe generatie laagfrequente telescopen (zoals LOFAR, MWA, uGMRT, MeerKAT enz.) en betere kalibratietechnieken, is het mogelijk geworden om de laagfrequente radiohemel te onthullen met ongekende diepte en gevoeligheid. Deze instrumenten zijn ook enkele van de belangrijkste padvindende voor de toekomstige generatie telescoop: de Square Kilometre Array (SKA; zal worden gebouwd in Zuid-Afrika en Australië). Ook al is het aantal van zulke waarnemingen momenteel zeer beperkt, de complexiteit van objecten die met deze nieuwe instrumenten worden waargenomen heeft de traditionele taxonomie van diffuse radiobronnen al in twijfel getrokken. Het is duidelijk dat het laagst waarneembare venster van de elektromagnetische straling een volledig onbekend terrein is en daarom vol potentie zit voor nieuwe ontdekkingen. Voordat we de wetenschappelijke vragen behandelen, is het echter

erg belangrijk om ervoor te zorgen dat deze radiobeelden van diepe laagfrequente surveys nauwkeurig zijn gekalibreerd en betrouwbaar zijn. 'Radiobron tellingen' - een van de verschillende kosmologische tests om nieuwe kosmologische modellen te controleren - is een onmiddellijk dataproduct van deze beelden dat kan worden gebruikt als een controle van de datareductie en om de statistische eigenschappen van de (zwakke) populatie van radiobronnen te onderzoeken. In dit proefschrift hebben we twee verschillende aspecten behandeld:

- De aard van de nieuw leven ingeblazen fossiele (radio) plasmabronnen in clusters van sterrenstelsels beter begrijpen en ze neerzetten als een aparte klasse van radiobronnen (Hoofdstuk 2,3 en 4).
- De diepste radiobron tellingen bij 150 MHz (tot nu toe) afleiden uit diepe laagfrequente radiobeelden en vergelijken met de andere bestaande studies, evenals met state-of-the-art evolutionaire modellen (Hoofdstuk 5).

Hieronder beschrijven we in het kort de inhoud van elk hoofdstuk: In **Hoofdstuk 2** hebben we de botsende cluster van sterrenstelsels Abell 1914 in detail bestudeerd met diepe radio- (LOFAR, GMRT en VLA), röntgen (Chandra) en optische (CFHT) data. Deze nieuwe waarnemingen laten zien dat de bron met het ultra-steile spectrum in dit cluster, waarvan eerder werd gedacht dat het deel uitmaakte van een radio halo, een aparte bron is met de eigenschappen die consistent zijn met een radio feniks. **Hoofdstuk 3** demonstreert de potentie van laagfrequente radio surveys van de hele hemel voor het vinden en bestuderen van van nieuw leven ingeblazen fossiele plasmabronnen in clusters van sterrenstelsels. In dit hoofdstuk hebben we een subset van 3 kandidaten bestudeerd (waarvan 2 nieuwe ontdekkingen) met behulp van nieuwe multi-band radio, röntgen en oude optische data. Het artikel bespreekt de mogelijke gemeenschappelijke eigenschappen van deze bronnen en we identificeren ze in de categorie van radio feniksen. In **Hoofdstuk 4** geven we een overzicht van alle bekende (of kandidaat-) radio feniksen. Van de 25 getoonde bronnen zijn er 12 nieuwe ontdekkingen. Voor deze bronnen presenteren we nieuwe radio (GMRT en/of LOFAR) en, voor een deelverzameling, röntgen waarnemingen. Voor het eerst worden de algemene fysische eigenschappen (de vorm, dynamische toestand van de cluster, locatie van de feniksen in de cluster en spectraal gedrag) van de hele steekproef van radio feniksen bestudeerd, om de aard van deze relatief onbekende klasse van objecten te achterhalen. We vinden dat deze bronnen voorlopig een AGN-oorsprong lijken te hebben en ruim binnen de binnenste regio's van de clusters liggen. De clusters blijken dynamisch niet ontspannen te zijn en daarom ondersteunen we het formalisme dat feniksen worden geassocieerd met

ICM-beweging en/of schokken. De steekproef die in dit hoofdstuk wordt gepresenteerd is waarschijnlijk nog steeds het topje van de ijsberg van deze klasse van bronnen en toekomstige diepere laagfrequente radio observaties zullen cruciaal zijn om een zuivere statistische steekproef van deze klasse te maken. Ten slotte, presenteren we in **Hoofdstuk 5** de tellingen van radiobronnen die zijn afgeleid van zeer diepe radiobeelden die zijn waargenomen met de LOFAR-telescoop. Tot op heden zijn dit de diepste tellingen die ooit zijn gemaakt bij 150 MHz. Deze worden vergeleken met andere bestaande bepalingen, evenals met state-of-the-art simulaties. Onder de 1 mJy zien we de (verwachte) afvlakking van de genormaliseerde tellingen, voornamelijk geassocieerd met de opkomst van de populatie van stervormende sterrenstelsels. In de toekomst zullen deze diepe radiogegevens ons kritisch in staat stellen om de zwakke radiobronnen goed te bemonsteren over verschillende waarden van helderheid en roodverschuiving.

List of publications

First Author

Ultra-steep spectrum emission in the merging galaxy cluster Abell 1914

S. Mandal, H. T. Intema, T. W. Shimwell, R. J. van Weeren, A. Botteon, H. J. A. Röttgering, D. N. Hoang, G. Brunetti, F. de Gasperin, S. Giacintucci, H. Hoekstra, A. Stroe, M. Brüggen, R. Cassano, A. Shulevski, A. Drabent, D. Rafferty, *A&A* 622, A22 (2019).

Revived fossil plasma sources in galaxy clusters

S. Mandal, H. T. Intema, R. J. van Weeren, T. W. Shimwell, A. Botteon, G. Brunetti, F. de Gasperin, M. Brüggen, G. Di Gennaro, R. Kraft, H. J. A. Röttgering, M. Hardcastle, C. Tasse. *A&A* 634, A11 (2020).

Towards a sample of revived fossil plasma sources in Galaxy Clusters

S. Mandal, R. J. van Weeren, T. W. Shimwell, H. T. Intema, A. Botteon, F. de Gasperin, G. Di Gennaro, M. Grespan, G. Brunetti, M. Brüggen, M. Brienza, F. Gastaldello, M. J. Hardcastle, H. Röttgering, R. Kraft, R. Cassano, A. Drabent, M. Hoeft, D. Jung, L. K. Morabito, A. Shulevski, W. L. Williams, submitted to *A&A*.

Extremely deep 150 MHz Source Counts from the LoTSS Deep Fields

S. Mandal, I. Prandoni, M. J. Hardcastle, T. W. Shimwell, H. T. Intema, C. Tasse, R. J. van Weeren, H. Algera, K. L. Emig, H. J. A. Röttgering, D. J. Schwarz, T. M. Siewert, P. N. Best, M. Bonato, M. Bondi, M. J. Jarvis,

R. Kondapally, S. K. Leslie, V. H. Mahatma, J. Sabater, E. Retana-Montenegro, W. L. Williams, submitted to A&A.

Contributing Author

Fast magnetic field amplification in distant galaxy clusters

G. Di Gennaro, R. J. van Weeren, G. Brunetti, R. Cassano, M. Brüggen, M. Hoeft, T. W. Shimwell, H. J. A. Röttgering, A. Bonafede, A. Botteon, V. Cuciti, D. Dallacasa, F. de Gasperin, P. Domínguez-Fernández, T. A. Ensslin, F. Gastaldello, **S. Mandal**, M. Rossetti & A. Simionescu, *Nature Astronomy* (2020)

A giant radio bridge connecting two galaxy clusters in Abell 1758

A. Botteon, R. J. van Weeren, G. Brunetti, F. de Gasperin, H. T. Intema, E. Osinga, G. Di Gennaro, T. W. Shimwell, A. Bonafede, M. Brüggen, R. Cassano, V. Cuciti, D. Dallacasa, F. Gastaldello, **S. Mandal**, M. Rossetti and H. J. A. Röttgering, *MNRAS: Letters*, Volume 499, Issue 1, pp.L11-L15 (2020)

The great Kite in the sky: a LOFAR observation of the radio source in Abell 2626

A. Ignesti, T. Shimwell, G. Brunetti, M. Gitti, H. Intema, R. J. van Weeren, M. J. Hardcastle, A. O. Clarke, A. Botteon, G. Di Gennaro, M. Brüggen, I. Browne, **S. Mandal**, H. J. A. Röttgering, V. Cuciti, F. de Gasperin, R. Cassano, A. M. M. Scaife, Accepted for publication on *Astronomy & Astrophysics*

The Beautiful Mess in Abell 2255

A. Botteon, G. Brunetti, R. J. van Weeren, T. W. Shimwell, R. F. Pizzo, R. Cassano, M. Iacobelli, F. Gastaldello, L. Birzan, A. Bonafede, M. Brüggen, V. Cuciti, D. Dallacasa, F. de Gasperin, G. Di Gennaro, A. Drabent, M. J. Hardcastle, M. Hoeft, **S. Mandal**, H. J. A. Röttgering, and A. Simionescu, *The Astrophysical Journal*, Volume 897, Issue 1, id.93 (2020)

The life cycle of radio galaxies in the LOFAR Lockman Hole field

N. Jurlin, R. Morganti, M. Brienza, **S. Mandal**, N. Maddox, K. J. Duncan, S. S. Shabala, M. J. Hardcastle, I. Prandoni, H. J. A. Röttgering, V. Mahatma, P. N. Best, B. Mingo, J. Sabater, T. W. Shimwell and C. Tasse, *A&A*, 638 (2020) A34

The spectacular cluster chain Abell 781 as observed with LOFAR, GMRT, and XMM-Newton

A. Botteon, T. W. Shimwell, A. Bonafede, D. Dallacasa, F. Gastaldello, D. Eckert, G. Brunetti, T. Venturi, R. J. van Weeren, **S. Mandal**, M. Brüggen, R. Cassano, F. de Gasperin, A. Drabent, C. Dumba, H. T. Intema, D. N. Hoang, D. Rafferty, H. J. A. Röttgering, F. Savini, A. Shulevski, A. Stroe and A. Wilber, *A&A* 622, A19 (2019)

The LOFAR Two-metre Sky Survey. II. First data release

LOFAR Surveys: a new window on the Universe, *Astronomy & Astrophysics*, Volume 622, id.A1, 21 pp (2019)

LOFAR discovery of a double radio halo system in Abell 1758 and radio/X-ray study of the cluster pair

A. Botteon, T. W. Shimwell, A. Bonafede, D. Dallacasa, G. Brunetti, **S. Mandal**, R. J. van Weeren, M. Brüggen, R. Cassano, F. de Gasperin, D. N. Hoang, M. Hoeft, H. J. A. Röttgering, F. Savini, G. J. White, A. Wilber, T. Venturi, *MNRAS*, Volume 478, Issue 1, July 2018, Pages 885–898

LOFAR discovery of an ultra-steep radio halo and giant head-tail radio galaxy in Abell 1132

A. Wilber, M. Brüggen, A. Bonafede, F. Savini, T. Shimwell, R. J. van Weeren, D. Rafferty, A. P. Mechev, H. Intema, F. Andrade-Santos, A. O. Clarke, E. K. Mahony, R. Morganti, I. Prandoni, G. Brunetti, H. Röttgering, **S. Mandal**, F. de Gasperin, M. Hoeft, *MNRAS*, Volume 473, Issue 3, January 2018, Pages 3536–3546

The LOFAR Two-metre Sky Survey. I. Survey description and preliminary data release

LOFAR Surveys Key Science Project, *A&A*, Volume 598, id.A104, 22 pp, 2017

The Lockman Hole project: LOFAR observations and spectral index properties of low-frequency radio sources

E. K. Mahony, R. Morganti, I. Prandoni, I. M. van Bemmelen, T. W. Shimwell, M. Brienza, P. N. Best, M. Brüggen, G. Calistro Rivera, F. de Gasperin, M. J. Hardcastle, J. J. Harwood, G. Heald, M. J. Jarvis, **S. Mandal**, G. K. Miley, E. Retana-Montenegro, H. J. A. Röttgering, J. Sabater, C. Tasse, S. van Velzen, R. J. van Weeren, W. L. Williams, G. J. White

Curriculum Vitae

I was born on the 17th of September 1992 in Purulia, a small town in the state of West Bengal, in India. Even though my family is full of medical doctors, I never had the interest to pursue that career path. I remember myself being very outdoorsy and passionate about adventures. I can trace back the first stimulation of my first interest in ‘Astro’ related things to the historic event of the Columbia Space Shuttle in 2003. I was really excited about the fact that the first woman from Indian origin, Kalpana Chawla was on board. The Columbia journey had ended with sad memories, however, it had given birth to a dream inside me to know more about space and celestial bodies.

During the early years of my school life, I started developing interest in scientific subjects, especially in Maths and Physics. I also started taking participation in national level competitive examinations. During the last year of my high school in 2010, I qualified in the Indian Institute of Technology Joint Entrance Examination (IIT-JEE) and chose to pursue an integrated masters degree in Physics from one of the premier institutes in India: the Indian Institute of Technology, Kharagpur. During my 1st year of my undergraduate studies, I was selected to represent my institute in an academic camp called ‘Vijyoshi’, that was organised by the Indian Institute of Science, Bangalore. In that camp, renowned scientists presented lectures on Astronomy and Astrophysics and that triggered my childhood interests to know about the universe. From that time onwards, I was determined to pursue my study in Astronomy and Astrophysics. Our department did not offer many astronomy related courses. But, I started to work with Prof. Somnath Bharadwaj, a faculty at IIT Kharag-

pur, on short term projects and gradually started developing interest in radio astronomy. Following this, I gathered several research experiences in the field of radio astronomy. I worked as a summer student at NCRA-TIFR under the supervision of Prof. Jayaram Chengalur where I was involved with the process of upgrading the Ooty Radio Telescope (ORT). Later, in 2014, I was selected for a summer internship at the Leiden Observatory, under the supervision of Dr. Timothy Shimwell to work on Westerbork Synthesis Radio Telescope (WSRT) observations of proto-clusters. During my masters' thesis, I worked on theoretical modelling of magneto-convection under the supervision of Prof. Krishna Kumar. I graduated with a masters degree in Physics in the August of 2015.

In September 2015, I started a position as a PhD candidate at the Leiden Observatory under the supervision of Dr. Huib Intema and Prof. dr. Huub Röttgering. During the first year of my PhD, I was involved in the development of LOFAR calibration pipelines and collaborated with a lot of scientists at the Netherlands Institute for Radio Astronomy (ASTRON). This experience allowed me to appreciate the huge amount of technological advancements that have been made in this field and to familiarize with big data problems. In the later years, I started to work on diffuse radio emission in galaxy clusters. During my PhD, I mostly focused to study revived fossil plasma sources in galaxy clusters and used LOFAR data to derive the deepest radio source counts at 150 MHz, ever obtained. These two aspects of the thesis, blend the technical side of radio astronomy with the scientific prospects of the field. I was fortunate enough to travel around the world and present my scientific results in international conferences (India, USA, China, Italy, Germany, France) and visit collaborators (USA, Italy) to work with. It has been a great learning experience to communicate with such a large and diverse audience in so many countries. In Leiden, I have been a teaching assistant for the bachelor course "Astronomical Observing Techniques" and the masters course "Radio Astronomy". I also have been a co-supervisor for one of the summer students during LEAPS 2018. I also worked as one of the editors for the Annual Report of the Leiden Observatory in 2017. In addition, for 3 years (until 2019) I was a member of the social committee and helped in the organisation of annual events at the Observatory such as Sinterklaas, Christmas lunch and the summer barbecue.

Working at the Leiden Observatory has truly been an enriching experience, both professionally and personally. In future, I wish to use my experience and continue to do research in the field of space science and technology.

Acknowledgements

My PhD journey in Leiden has been a wonderful experience. I was very fortunate to have such a friendly, welcoming and international environment at the Leiden Observatory. Coming all the way from India to a foreign country was not an easy choice, but I am very glad that I took this leap. Being a part of the LOFAR group has been a great learning experience. Huib, I learnt a lot from you; not just in academic matters but also in tackling many other challenges. Thank you for the guidance in this journey. Tim, you are one of the nicest colleagues that anyone could wish to work with. Starting from your supervision during my summer internship to all these years, I had a great time working with you on so many different projects; thank you for everything. Fra(ncesco), I always valued your opinions and suggestions. You always demonstrated how to think pragmatically and tackle things in a rational way. I am very lucky to have worked with so many excellent scientists in the LOFAR collaboration. Amongst them, I am particularly grateful to Isabella and Gianfranco. You always allowed me to visit in Bologna to work with you. Thank you very much for the support. Xander, thank you so much for your encouraging words and support, especially in the last few months, I really appreciate it.

For my PhD research, I used a lot of computing resources and it would not have been possible without the help from the Sterrewacht computer group. Erik, Aart, David, Eric and Leonardo, thank you so much for your prompt responses for all the helpdesk tickets I submitted. I would also like to thank Evelijn, Alexandra, Marjan, Caroline, Monica and all the other secretaries for making the official work so smooth; I never had to worry about those aspects.

I would like to thank my (extended) LOFAR / galaxy-cluster family who are now spread all over the world: Aayush, Alessandro, Alex, Alexander Shulevski, Andra, Andrea, Andreas Horneffer, Anniek, Aurora, Cyril, David Rafferty, Duy, Edwin, Erik (thank you so much for translating the summary in Dutch!), Fabio Gastaldello, Frits, Francois, George, Gabriella, Hiddo, Joe, Josh, Ken, Kim, Leah, Lýdia, Maolin (you will always be missed), Marisa, Martijn, Martin Hardcastle, Marcus Brügggen, Matthias Hoeft, Nika, Pedro, Rafaël, Roland, Rossella, Sarah, Virginia, Wendy, Xuechen and Yuhan. Special thanks go to Kim and Andrea (JAK, spicy finger!): not only you have been my colleagues but very close friends since the moment we started our PhD. Thank you for being an integral part of this journey. Hopefully some day, we will be able to guess the numbers for “the lotteries” ;).

During all these years, I have met so many wonderful people at the Sterrewacht. Christos and Tommaso, you are not only two of my closest friends, but are like my brothers. You guys thought about everything, haha. Thank you for countless awesome memories. The PhD journey would have been significantly different without you guys and I have been very lucky to share this path with friends like you. Grazie alla mia famiglia (quasi tutta) italiana: Valeriya (favourite office-mate ever), MariCri, Gabriella and Eleonora: thank you for all the nice memories, the honorary citizenship and always making me feel like home. To the Maastricht 2019 group: Anna, Mantas, Fraser, Kirsty, Pooneh, Anniek & Arthur: spending holiday season far from home is not easy, but you all made it super fun and enjoyable. Thank you for all the fun times. To all the other people from the Sterrewacht (or in connection with): Andrea (Manrique), Andrej, Alberto, Bas, Clément (I hope you still have the ladle), Dario, Dilovan, Emanuele, Francois (Grande man!), Gaby, Marco, Davide, Igone, Lamim, Lýdka, Lorenzo, Luke, Omar, Mieke, Marta, Matteo, Martinella, Pedrito, Salvatore, Santiago and anyone else that I might have missed; thank you for the time spent together and all kinds of social activities.

In my experience, having a good work life balance also depends on the interaction one makes outside the workplace. I am very glad that I had been surrounded by so many wonderful people during this time who made a direct or indirect contribution for the completion of this thesis. Elenita, I cannot thank you enough, it’s IMPOSSIBLE. The emotional support and the friendship that I had from you, are unparalleled and I am so happy to have you in my life. And of course, thank you for the amazing cover and abstaining (==saving) people from getting the glimpse of my art skills! Ireth, my Costa Rican sister; thank you so so much for listening to me all the time and helping me out in the hard times. I am so happy that all these years we managed to “keep in touch” and I

hope to do the same in future ;). Vince, my friend, my housemate, thank you for everything. Without your constant support, this journey would have been much harder. Thanks a lot also for all the food and teaching me so many Italian cuisine. Nicandro and Flavio, thank you for being such amazing friends, I could always count on you! No one taught (some people would use the word 'impose') me the concept of Italian cuisine more scientifically than you two! Marta and Federica, grazie belle, from the bottom of my heart! Your words and support meant a lot. Andrea (rocca): Maaaaan! we shared A LOT of memories together (of course, also the birthday) and thank you for everything. Hopefully 8a+ at some point in near future ;). Noemi, thank you for your support during the last year and being positive about things in general; it helped a lot! Aurelio, Piermarco, Tilbe, Lieslore and Liuba: thank you for all the nice discussions and fun memories. Frédérique, thank you for being such an amazing, cool and positive person! You always listened to me and made me feel better. Thank you to my fellow PhDs (mostly): Helena, Anna Prydatko, Uditendu, Alexandru, Chris, Lavinia, Leonardo, Miriam, Erik, Claudiu, Swantje, Yan, (little) Tim, Natacha, Aleksandrina; for all the happy moments, discussions that we shared over these years.

The sport of climbing is known to attract people with an analytic mind because it involves solving a 'problem'. However, for me climbing has not just been a sport, it has been my safe place where I could learn my capabilities, re-energise my brain and motivate myself to improve the quality of life. During this activity, I met many people and big cheers to all those friends: Arthur, Lise, Pablito, Filippo (allez ha!), Aurelio, Piermarco, Andrea, Christos, Liuba, Christiane, Lieslore, Federico, Chloé, Harish, Hugo, Raúl, Ander, Jelle, Daragh, Evan and anyone else who I might have missed.

I would also like to acknowledge my friends from India. Sayan, Apurba, Phul and Arghya, growing up with you had a big impact on my life and I am very thankful for that. Subhadeep da, Sumit and Madhu, thank you for your support, I could always count on you. Sandeep dada, Abhisek, Kaushik, Siddhartha and Nilanjan: thank you for all the amazing years filled with unforgettable memories and learning experiences.

Finally, even though any amount of thankfulness will never be enough, I would like to convey my heartiest gratitude to my parents, my brother and my grandparents for their unconditional love, support and encouragement since the time I was born. Maa & Baba: without you I would have never become the person that I am now, thank you for everything.